DYNAMIC RESPONSE OF COMPLEX MATERIALS UNDER SHOCK LOADING

A Dissertation

by

BEDRI ARMAN

Submitted to the Office of Graduate Studies of
Texas A&M University
in partial fulfillment of the requirements for the degree of

DOCTOR OF PHILOSOPHY

August 2011

Major Subject: Chemical Engineering

DYNAMIC RESPONSE OF COMPLEX MATERIALS UNDER SHOCK LOADING

A Dissertation

by

BEDRI ARMAN

Submitted to the Office of Graduate Studies of
Texas A&M University
in partial fulfillment of the requirements for the degree of

DOCTOR OF PHILOSOPHY

Approved by:

Chair of Committee,	Tahir Cagin
Committee Members,	Jorge Seminario
	Zhengdong Cheng
	Lin Shao
Head of Department,	Michael Pishko

August 2011

Major Subject: Chemical Engineering

ABSTRACT

Dynamic Response of Complex Materials Under Shock Loading. (August 2011)

Bedri Arman, B.S., Bogazici University;

M.S., New Mexico Institute of Mining and Technology

Chair of Advisory Committee: Dr. Tahir Cagin

We investigated dynamic response of $Cu_{46}Zr_{54}$ metallic glass under adiabatic planar shock wave loading (one-dimensional strain) with molecular dynamics simulations, including Hugoniot (shock) states, shock-induced plasticity, and spallation. The Hugoniot states are obtained up to 60 GPa along with the von Mises shear flow strengths, and the dynamic spall strengths, at different strain rates and temperatures. For the steady shock states, a clear elastic-plastic transition is identified. The local von Mises shear strain analysis is used to characterize local deformation, and the Voronoi tessellation analysis, the corresponding local structures at various stages of shock, release, tension and spallation. The plasticity in this glass, manifested as localized shear transformation zones, is of local structure rather than thermal origin, and void nucleation occurs preferentially at the highly shear-deformed regions. The Voronoi and shear strain analyses show that the atoms with different local structures are of different shear resistances that lead to shear localization.

Additionally, we performed large-scale molecular dynamics simulations to investigate plasticity in Cu/Cu46Zr54 glass nanolaminates under uniaxial compression. Partial and full dislocations are observed in the Cu layers, and screw dislocations, near the amorphous−crystalline interfaces (ACIs). Shear bands are directly induced by the dislocations in the crystalline Cu layer through ACIs, and grow from the ACIs into the glass layers and absorb ambient shear transformation zones. Plasticity in the glass layers is realized via pronounced, stable shear banding.

As the last part of the dissertation, we investigated with nonreactive molecular dynamics simulations, the dynamic response of phenolic resin and its carbon-nanotube (CNT) composites to shock wave compression. For phenolic resin, our simulations yielded shock states in agreement with experiments on similar polymers, except the "phase change" observed in experiments, indicating that such phase change is chemical in nature. The elastic–plastic transition is characterized by shear stress relaxation and atomic-level slip, and phenolic resin shows strong strain hardening. Shock loading of the CNT-resin composites was applied parallel or perpendicular to the CNT axis, and the composites demonstrated anisotropy in wave propagation, yield and CNT deformation. Our simulations suggested that the bulk shock response of the composites depends on the volume fraction, length ratio, impact cross-section, and geometry of the CNT components; the short CNTs in current simulations had insignificant effect on the bulk response of resin polymer.

To my family and Nevin

ACKNOWLEDGEMENTS

First, I would like to thank Professor Tahir Cagin, who has been my research advisor over the past five years. This dissertation would not exist if he had not offered me the opportunity to come to Texas A&M. I deeply appreciate his support, both intellectually and financially. I also thank my committee members: Dr. Jorge Seminario, Dr. Zhengdong Cheng and Dr. Lin Shao for their critical review and valuable comments.

I wish to thank Dr. Sheng Nian Luo, who mentored me through my internship at Los Alamos National Laboratory. His expertise in shock physics was very helpful in my research. I would like to thank Dr. Desai Tapan, for his many suggestions and cooperation.

I am very thankful to my past and current group members who have all been very supportive and friendly: Dr. Cem Sevik, Oscar Ojeda, Dr. Jennifer Carvajal, Alper Celik, Justin Haskins, Arnab Chakrabarthy, Sandeep Kamani, Selma Atilhan, Mousumi Mani, Jean Njoroge, Kristen Williams, Dr. Carlos Silva, Dr. Dundar Yilmaz and Dr. Hieu Pham. I would like to give my best wishes to all of them.

I would like to thank my parents and my brother for their support and understanding, and I am very grateful to them. Finally, I would like to specially thank my sweetheart, Nevin, who has been a steady companion, partner and friend. Her unconditional love and patience always comforted me throughout this work.

NOMENCLATURE

ACI Amorphous−crystalline interfaces

b Burgers vector

CN Coordination number

CNT Carbon-nanotube

CP Centrosymmetry parameter

EAM Embedded atom method

EQM Equation of motion

f_{ij} Force between particle i and j

FCC Face-centered cubic

GFA Glass forming ability

h Hydrostaticity

HEL Hugoniot elastic limit

K Kelvin

K_b Boltzmann constant

lj Lennard Jones

MD Molecular dynamics

MRD Maximum relative displacement

MRO Medium-range order

N Total number of atoms

NPT Isothermal – Isobaric ensemble

n_s Number of slipped neighbors

NVE Ensemble with constant atoms, volume and energy

PBC Periodic boundary conditions

PCFF Polymer consistent force field

PMMA Polymethyl methacrylate

r_{cut} Cut-off distance

RDF Radial distribution functions

SRO Short-range order

STZ Shear transformation zone

T Temperature

T_{sp} Spall temperature

u_{fs} Free surface velocity

u_p Particle velocity

u_s Shock velocity

V Volume of the cell

ε Strain

σ Stress

σ_Y Yield stress

Z Effective charge

λ Berendsen scaling factor

κ Compressibility factor

μ Shear modulus

υ Poisson's ratio

J_2 Second deviatoric stress invariant

η^{vM} Von Mises type shear strain

c_{L} Longitudinal sound speed

σ_{sp} Dynamic spall strength

δt Time step

TABLE OF CONTENTS

CHAPTER Page

LIST OF FIGURES

FIGURE Page

FIGURE Page

FIGURE Page

LIST OF TABLES

CHAPTER I

INTRODUCTION

Metallic glasses are amorphous alloys, which are prepared from metallic liquids by rapid cooling. Since metallic glasses have randomly ordered structures and are lack of dislocations they offer unusual properties, such as high strength and corrosion resistance, great hardness and soft magnetism.[1-9] These unique and desirable material properties attracted a great deal of scientific and technological attention and their mechanical properties, deformation and fracture mechanisms have been substantially investigated by both experimental and theoretical studies. Superior mechanical properties of metallic glasses also create potential fields for impact applications such as armor operations. However, there has not been much research on the high-strain rate response of the metallic glasses even though it is critical to understand their yielding behavior and fracture mechanism under high strain rates (10^3 s^{-1} to 10^6 s^{-1}). Therefore, in this dissertation work, we have studied the dynamic response and damage mechanism of $Cu_{46}Zr_{54}$ metallic glass under shock loadings using Molecular Dynamics.

Molecular Dynamics (MD) is a powerful method to study the static and dynamic properties of materials and has become especially useful for shock compression studies due to similar time and length scales for real life laser-shock compression experiments. Thus, MD simulations for planar compressive shock wave loadings have been well implemented and established. However, no MD simulation has been addressed for shock response of metallic glasses before. Therefore, in this work, we performed MD simulations to shed light on the shock response of the metallic glasses.

In addition to dynamic loading of metallic glasses, we also focus on static deformation of nanocrystalline - amorphous nanolaminates due to presence of interesting recent experimental results illustrating the role of amorphous-crystalline interface (ACI)

This dissertation follows the style of *Nature Materials.*

as a source or sink of dislocations. Since the understanding of shear banding mechanism in metallic glasses is very imperative for designing and preparing better materials, we focus on the shear band-dislocation relation at the ACI of Cu(111)/$Cu_{46}Zr_{54}$ metallic glass nanolaminates using MD simulations.

In the last part of the dissertation work, we concentrate on the dynamic loadings of phenolic resin and its carbon nanotube (CNT) composite using MD simulations. Polymers and polymer-based composites have been widely studied for high strain rates in order to be used for aerospace applications, however, the underlying deformation mechanisms are still lacking mostly due to the complex structures of polymeric materials. We, for the first time in literature, applied MD simulation for direct shock loading to a polymer and polymer composites. The sections of this dissertation are separated as follows:

In Chapter III, the dynamic loading of $Cu_{46}Zr_{54}$ metallic glass under shock loading is presented. The presentation discusses the background about metallic glasses and MD shock simulations. This is followed by the methodology related to MD simulations and the deformation and structure analysis methods (the local von Mises shear strain, von Mises shear flow strength and Voronoi tessellation). Finally, results and discussions including the Hugoniot states, plasticity, spall, the mechanisms for plasticity and spallation as well as the related structural features are provided.

In Chapter IV, a literature review about shear band formation in metallic glasses and its importance in composite materials is given. The methodologies about Cu(111)/$Cu_{46}Zr_{54}$ metallic glass nanolaminate sample preparation and visualization methods for plasticity investigation are mentioned and followed by the results and discussions about the dislocation induced shear banding phenomena.

In Chapter V, the dynamic loading of the phenolic resin and its CNT composite under shock loadings is presented. First, the literature review and the importance of the work are described and then we address the methodology of MD simulations and post processing followed by results and discussion. In results and discussion section, the pure

phenolic resin polymer and its two different oriented CNT composite versions are mentioned and the new insights about the CNT orientations are discussed.

Finally, in Chapter VI, the summary and conclusions about the dissertation work is reported.

CHAPTER II

BACKGROUND

2.1 Molecular Dynamics Simulation Methods

2.1.1 Introduction

Molecular Dynamics (MD) is one of the most widely used simulation methods for estimating the equilibrium and transport properties by solving the classical many-body interactions.[10] This requires solving the equations of motion (EQM) of all atoms whose interactions are treated based on the laws of classical mechanics. First MD simulation was introduced by Alder and Wainwright in 1957 based on a hard-sphere model in which the spheres move in straight lines with constant velocity between the collisions.[11] This quite simple model revealed useful microscopic fluid nature and the differences between the solid and fluid phases. Afterwards, in 1964, Rahman[12] introduced continuous potentials for the intermolecular interactions in which the force on each atom changes upon the change of position of the atoms. Since the force depends on the particle position, the movements of all the particles are coupled by each other making impossible to solve the EQM analytically. Therefore, various finite difference methods have been used for integrating the equations of motion. These methods will be explained in the next sections.

In MD simulations, the main procedure starts with specifying the parameters of the run such as the desired initial temperature, system size (number of particles), time step, density etc.[13-15] The initialization of the system is followed by selecting the initial positions and velocities. After that, the computation of the forces between all particles and integration of Newton's equations of motion (EOM) are carried out. These last two steps consume most of the computing time during the whole simulation and are repeated until the desired time evolution of the system is achieved. After the completion of force

and EOM calculation loop, the desired averages of the system are printed for further analyses and finally the simulation stops.

2.1.2 Potentials

In MD, trajectories namely, successive configurations, are obtained by solving the differential equations embodied in Newton's second law: $F = ma$. In atomistic simulations, F, is the binding force between atoms which determines the material properties. There are commonly four types of interatomic forces (bonds) exist in materials. These are defined as ionic, metallic, covalent and van der Waals forces. Since van der Waals force is relatively weak, first three types of forces are the ones mostly contributing to the cohesion energy. However, categorizing the bond types into 3 or 4 sections is not healthy and one needs to solve Schrodinger's equation for a many-body problem to determine the bond type. Since this is not feasible for many atoms, approximations for the interatomic potentials have been developed. Since MD usually follows classical approximation; the atoms and molecules are treated as point masses and coupled by springs which can be represented as overlapped electron clouds in quantum mechanical description. The adaption from quantum perspective includes quantum mechanical energy calculations, experimental data (from spectroscopic studies), crystalline state structure information, collision studies from molecular beams, and measurements from transport properties.[16] It is also probable that in course of time one potential can be revised and updated or a totally new model can be developed based on the requirements. In the next section, pair potentials, first potential function used in MD simulations, will be mentioned.

2.1.3 Pair Potentials

Between the 1950s and 1980s, radially symmetric pair potential functions were the ones used most widely (Erginsoy et al.[17] and Rahman[12]). The interaction energy and force are computed by summing each pairwise of an atom and its neighbors. The most known pair interaction is the Lennard-Jones force field which has strongly repulsive core and weakly attractive tail imitating the van der Waals interaction. The functional form of the Lennard-Jones potential is

$$V_{LJ}(r_{ij}) = 4\varepsilon_{ij}\left[\left(\frac{\sigma_{ij}}{r_{ij}}\right)^{12} - \left(\frac{\sigma_{ij}}{r_{ij}}\right)^{6}\right], \qquad (2\text{-}1)$$

where i and j atoms located at r_i and r_j therefore $r_{ij} = r_i - r_j$. The parameter ε determines the strength of the interaction, whereas σ relates to the collision diameter (see Figure 2.1). In these interactions, each pair of atom is treated independently, which means, other atoms in the neighborhood do not have any effect on the force between atoms i and j. r-6 and r-12 form the attractive and the repulsive part of the potential. Since the interaction of any pair of atoms depends on the distance between them and not on the angular position of other atoms nearby, classical pair potentials are considered as radially symmetric.

2.1.4 Many Body Potentials

Pair potentials have some key limitations: *i)* Either vacany formation or cohesive energy per atom cannot be explained correctly.[18] *ii)* The direction of the bonding is unclear due to radial symmetric nature of the pair potentials causing inadequate estimation of lattice defect dynamics for transition metals. *iii)* Inaccurate prediction of the Cauchy discrepancy when used for metals.[16] In the Lennard-Jones potential the interatomic interactions, based on the electron clouds, are localized close to the atoms. However, this is not the case for metals since the valence electrons are shared among at-

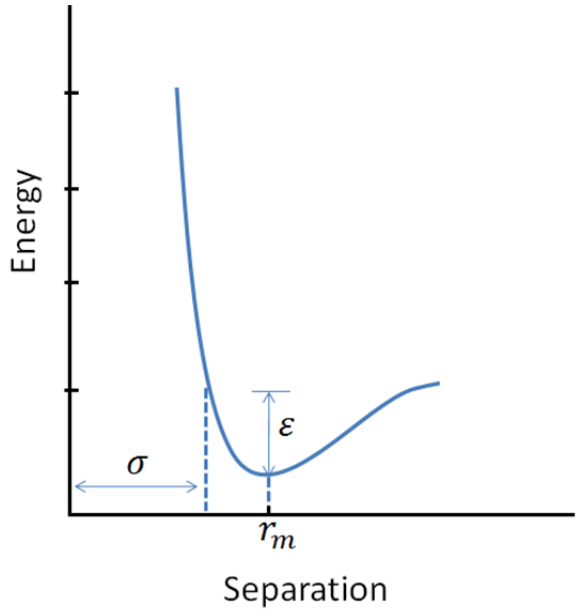

Figure 2.1 The Lennard-Jones potential (Adapted from Ref.[10])

oms, thus potentials taking the local electron density into consideration should be used. These potentials have many-body nature in which the neighboring atom positions affect the force between any pair.

There are various types of many-body potentials based on their usage; Finnis and Sinclair[19-21], and the Embedded Atom Method (EAM)[22-24] potentials for instance have been widely used for metals, whereas Brenner potential[25] is used for hydrocarbons. Rosato et al[26] and Sutton and Chen[21] introduced alternative parameters for transition metals with face-centered cubic lattices (fcc) with hcp.

2.1.5 EAM Potential

The EAM potential has been one of the most used potentials for metallic systems. The idea in this potential is to separate metallic interactions into two parts. First part covers the pair interaction between the metal ions and second part carries the many-body part in which an ion is embedded in the electron gas.[22,24] The latter part is based on

the Density Functional Theory, which enables to determine the energy of a system of atoms via a functional of the electronic density.[27] Thus, one can calculate the energy V_i^{emb} of the i^{th} atom by embedding it into the electron density of the surrounding material via an appropriate embedding function F_i.[28]

$$V_i^{\mathrm{emb}} = F_i\left(\rho_i^{\mathrm{host}}\right); \tag{2-2}$$

where ρ_i^{host}, here denotes the electron density of the bulk or host material without the atom i at the point x_{i} and is calculated by summing the electron densities ρ_j^{atom} of all atoms depending on the distance to the atom I (see equation (2-3)). In other words F_i is the embedding energy at the position of i induced by all other atoms in the system.

$$\rho_i^{\mathrm{host}} = \sum_{j=1, j\neq i}^{N} \rho_j^{\mathrm{atom}}\left(\|r_{ij}\|\right) \tag{2-3}$$

Since the use of V_i^{emb} in equation (2-2) gives unrealistic results alone, as mentioned above, a pair potential in the form of equation (2-4) is added to the embedding potential;

$$V_i^{pair} = \frac{1}{2} \sum_{j=1, j\neq i}^{N} \phi_{ij}\left(\|r_{ij}\|\right), \tag{2-4}$$

where, V_i^{pair} potential is repulsive and depends only on the distance between the atoms. Energy values similar to the electrostatic charge can be acquired using Z_{i} functions (can also be named as effective charges). So overall, with pairwise repulsive and embedding many-body parts the EAM potential becomes

$$V = \sum_{i=1}^{N} F_i\left(\sum_{j=1, j\neq i}^{N} \rho_j^{\mathrm{atom}}\left(\|r_{ij}\|\right)\right) + \frac{1}{2} \sum_{i=1}^{N} \sum_{j=1, j\neq i}^{N} \frac{Z_i\left(\|r_{ij}\|\right) Z_j\left(\|r_{ij}\|\right)}{\|r_{ij}\|}. \tag{2-5}$$

The function F_i and the effective charges Z_i are prepared in a semi-empirical way depending on the material that is being modeled. On the other hand, the density function ρ_j is determined by Hartree-Fock approximations.

2.1.6 Equation of Motion and Integrators

After completion of force calculations between the particles, the Newton's equations of motion (EOM) can be integrated to obtain the trajectories. Based on the potential used, the N number of EOM can be solved by using a finite difference algorithm. The common way of achieving this is to break down the integration into small segments which are separated with a specific and fixed time intervals. At a time *t*, the total force on every particle is computed by adding its interactions with other particles. Once the force is known, using the Newton's second law, the particle accelerations can be obtained and combined with velocities and positions at that *t* to compute the new positions and velocities at a later time, $t + \delta t$. There are a number of methods designed for integrating the equations of motion, such as Verlet algorithm, predictor-corrector scheme, Leap Frog algorithm and Beeman algorithm.[14] One of the most widely used algorithms is the Verlet algorithm in which every consecutive position is calculated as follows;

$$\boldsymbol{r}(t + \delta t) = 2\boldsymbol{r}(t) - \boldsymbol{r}(t - \delta t) + \boldsymbol{a}(t)\delta t^2. \quad (2\text{-}6)$$

As seen from equation (2-6), velocity terms do not appear in the Verlet algorithm. In order to build it in this form, the Taylor expansion of the particle coordinates are added and the velocity terms are eliminated via the following equation

$$\boldsymbol{r}(t + \delta t) = \boldsymbol{r}(t) + \mathbf{v}(t)\delta t + \frac{\boldsymbol{f}(t)}{2m}\delta t^2 + \ldots \quad (2\text{-}7)$$

It should be also noted that $\boldsymbol{f}(t)/m$ term gives the acceleration, $\boldsymbol{a}(t)$. Similary, another Taylor expansion can be given as:

$$\boldsymbol{r}(t-\delta t) = \boldsymbol{r}(t) - \mathbf{v}(t)\delta t + \frac{\boldsymbol{f}(t)}{2m}\delta t^2 - \ldots \tag{2-8}$$

Summation of equations (2-7) and (2-8) yields the equation for Verlet algorithm (equation (2-6)). Since the velocity terms are not computed during the trajectory generations, if needed (e.g., for kinetic energy calculation) they can be obtained by the following formula:

$$\mathbf{v}(t) = \frac{\boldsymbol{r}(t+\delta t) - \boldsymbol{r}(t-\delta t)}{2\delta t}. \tag{2-9}$$

Another commonly used algorithm so called 'leap-frog' method calculates the new positions from velocities at half-integer time steps and uses the following equation

$$\boldsymbol{r}(t+\delta t) = \boldsymbol{r}(t) + \mathbf{v}(t+\delta t/2)\delta t\,. \tag{2-10}$$

The choice of these algorithms is very essential. Even though the speed of the algorithms can be thought to play an important role, this is not true, especially with today's computers. In MD calculations as mentioned in the introduction section, most of the computation time is being used for the force calculation of each particle during the simulation. More attention should be given when choosing an appropriate algorithm, whether it conserves energy and momentum, allows long time steps (δt) or is time-reversible. Besides those algorithms may differ in the error variation with different time steps, e.g., the predictor-corrector algorithms show more accurate results for short time steps whereas in longer time steps the Verlet methods become more accurate.[14] Other factors for choosing an appropriate integrator can include the memory requirements and self-starting properties, which are relatively less critical.

2.1.7 Boundaries

Boundary effects in MD simulations play a significant role since the aim is to calculate macroscopic or bulk properties of a sample from a relatively much smaller number of particles. Especially, interaction between the surfaces of the simulation box and the atoms in it can be a problem. For instance, a system of 1000 atoms has ~ 49% of all atoms at the surface, whereas one liter water (~ 3.3×10^{25} atoms) has only 2×10^{19} atoms on the surface making ~ 0.000075% of all the atoms. Therefore, the smaller the size of the system, the less accurate the results for the intended "bulk" calculations unless the "drop" of a water is studied.[10] To alleviate this problem, periodic boundary conditions (PBCs) are being implemented by replicating the particles periodically in all or desired directions (Figure 2.2) such that the particles interact each other as they were in a bulk environment.

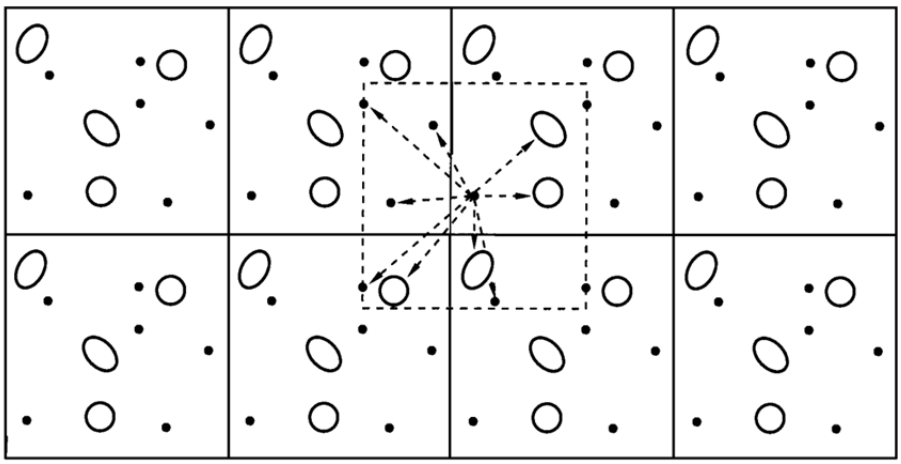

Figure 2.2 Boundary conditions in two dimensions[14].

Under PBCs, as soon as an atom leaves the simulation box, its periodic image enters to the same box (shaded particle in Figure 2.2) so that the total number of particles in the simulation box does not change. The particle coordinates in the image boxes are

calculated by adding or subtracting the integral multiples of the box sides. This implementation of periodicity is made after the integration of EOM and the force calculations. When a particle moves outside the box, the new coordinates of the atom leaving the box is calculated by adding or subtracting (depending on the leaving direction) the simulation box size from the position of the atom.

The periodic system does not have to be cubic; depending on the system, it can be hexagonal prism (cylindrical shapes like DNA) or the truncated octahedron or the rhombic dodecahedron (spherical molecules), etc. The main disadvantage of using periodicity in MD simulations is that they can cause some artificial correlation that does not exist in the real bulk system. It should be noted that the fluctuations having wavelengths more than the box length are not allowed, which may cause problems in the phase transition regions.[15]

2.1.8 Ensembles

The concept of ensemble averaging in MD simulations arises from the difficulty of determining macroscopic properties directly from the time evolution. Since it is not feasible to calculate the equation of motion and consequently the trajectory of an order of 10^{23} atomic or molecular size, the thermodynamic properties have to be calculated for an ensemble average. This ensemble average is microcanonical (constant NVE) nature in MD runs since the total energy, E, is taken constant throughout the time evolution. It is also possible to use other ensembles, which is mentioned in the following sections. The basic idea behind ensemble averaging is that the time average of an evolving single system can be replaced by a simultaneous large number of replication of the same system. This equivalence of time dependent interpretation to ensemble averaging is called the ergodic hypothesis and holds one of the key axioms in statistical mechanics.[29]

Besides NVE, two other common ensembles are constant NVT and constant NPT ensembles. MD simulation of different ensembles can be achieved by altering the

Lagrangian equations of motion of the system. In the following sections the constant temperature and/or pressure type ensembles will be mentioned.

2.1.9 Constant Temperature Dynamics

In MD simulations, it is quite common to run dynamics under constant temperatures in order to investigate various temperature effects on dynamics or to make a conformation search by gradually decreasing or increasing the temperature of the system. Even in the case of NVE ensemble, one can want to study under a desired starting temperature. Thus, the adjustment of temperature is important and can be carried out by various ways. One method is to scale the velocities since the temperature of the system is directly related to the kinetic energy by the following equations

$$E_{kin} = \frac{3N}{2} k_B T. \tag{2-11}$$

$$T = \frac{2}{3Nk_B} E_{kin} = \frac{2}{3Nk_B} \sum_{i=1}^{N} \frac{m_i}{2} \mathbf{v}_i^2 , \tag{2-12}$$

where N represents the total number of particles in the system. 3N comes from the number of degrees of freedom of the system. K_b is called the Boltzmann constant. Therefore, by rescaling the velocities at each time step or every *n* steps, the desired temperature can be obtained. The scaling is determined based on the following relation

$$V_{new} = c_T V_{old} \qquad c_T = \sqrt{\frac{T_0}{T}} . \tag{2-13}$$

Another method to change the temperature follows experiments similar to real life, which uses external heat bath to keep the system under constant temperature. This

heat bath either supplies or removes heat from the system based on the target temperature value. The rate of temperature change is related to the temperature difference between the heat bath and the system:

$$\frac{dT(t)}{dt} = \frac{1}{\tau}\left(T_{bath} - T(t)\right). \tag{2-14}$$

τ is the coupling parameter and governs the strength of coupling; if τ is large then the coupling will be weak and vice versa. This scaling of temperature at each step was introduced by Berendsen.[30] These two methods, however, do not generate the true canonical distribution and can give faulty results particularly in solvent – solution systems due to the artificial scaling of components of a system. Another two methods on the other hand, can produce canonical ensembles. These are Andersen[31] and Nose-Hoover[32] thermostats based on the stochastic collisions and the extended system, respectively.

In the Andersen method[31] each atom is subject to chosen randomly to experience collision with the heat bath at each integration step. Its velocity is then reassigned from Maxwell-Boltzmann distribution such that the velocities of other atoms do not change. Between these stochastic collisions, system evolves as series of microcanonical simulations (constant energy). However, one should notice that Andersen thermostat does not produce a smooth trajectory and does not conserve energy and momentum. Nose-Hoover[32] method, on the other hand, follows a deterministic approach and utilizes an extended Lagrangian, which contains additional coordinates and velocities. This extended Lagrangian is in the form of the difference between the heat bath and the system:

$$L = \sum_i \frac{m_i}{2}\tilde{s}^2\dot{\tilde{r}}_i^2 - U(\tilde{r}) + \frac{1}{2}Q\,\dot{\tilde{s}}_i^2 - gk_bT_0 ln\tilde{s}, \tag{2-15}$$

where, $\tilde{s}$ is the additional coordinate in the Lagrangian. The first and second terms in equation (2-15) are the kinetic and the potential energies of the real system, respectively. g is equal to the total number of degrees of freedom and finally Q is the mass associated with the additional variable, $\tilde{s}$.

2.1.10 Constant Pressure Dynamics

In many cases, pressure of the system as well as the temperature is also desired to be kept at constant values. These isothermal and isobaric type ensembles are also pertinent with experimental data since real life experiments are usually carried out under constant pressure and temperature. The pressure in MD simulations is calculated by the virial theorem via the following equation

$$P = \frac{1}{V}\left[Nk_bT - \frac{1}{3}\sum_{i=1}^{N}\sum_{j=i+1}^{N} r_{ij}f_{ij}\right], \tag{2-16}$$

where f_{ij} is the force between particle i and j, N is the number of particles, T is the temperature and k_b is the Boltzmann constant. Since the f_{ij} is calculated as a part of the MD simulation, the computation of pressure requires less effort. During simulation, the constant pressure is kept by changing the volume of the simulation cell. This change can be done in all three directions of the cell or in desired directions only. The methods implemented to keep the pressure constant in an MD simulation are not different from constant temperature calculations such as scaling the volume for the desired pressure or coupling the system to a pressure bath (Berendsen implementation) based on the following equation

$$\frac{dP(t)}{dt} = \frac{1}{\tau_P}\left(P_{\text{bath}} - P(t)\right). \tag{2-17}$$

Here, τ_P is the coupling constant and P_{bath} is the pressure of the bath. Based on the following equation the scaling factor, λ, is calculated (equation (2-18)) where κ is the isothermal compressibility.

$$\lambda = 1 - \kappa \frac{\delta t}{\tau_P}(P - P_{bath}) \tag{2-18}$$

The new atomic positions are then estimated using the below equation, where r_i is the old and r_i' is the new atomic coordinates.

$$r_i' = \lambda^{1/3} r_i \tag{2-19}$$

2.2 Shock Compression of Solids

2.2.1 Definition

When an external force is applied to a body with a low rate of change, the deformation is considered as sequence of steps and the body will be in static equilibrium, even though the initial external force creates a dynamic process in the first place.[33] However in the case of high amplitude stress waves, which exceed the dynamic flow strength of the body, the body cannot show any resistance to shear and the deformation can follow the fluid dynamics.[33] Shock wave concept can be understood more clearly by the famous snowplow example.[34] As seen in Figure 2.3, a snowplow begins moving at $t = t_o$. A Δt time later, the boundary between the fresh snow and the packed snow moves a distance of $U \times \Delta t$, longer than the snow plow, which proceeds a distance of $u \times \Delta t$.

It is very important to differentiate between particle velocity and shock velocity. Shock velocity is the speed of disturbance that goes through the material under the shock loading and is the interface of fresh snow and packed snow in our example. On the other

hand, the particle velocity is the velocity of an element of the material, which the shock wave passes over. In our snowplow example, particle velocity is the velocity of the snowplow, U_p, which is lower than the shock wave velocity, U_s.

2.2.2 Jump Conditions and Equation of State

Since conservation laws for mass, momentum, and energy are still valid across the shock discontinuity, the "jump conditions" can be obtained by utilizing these laws. Jump conditions are defined as the new energy, E, pressure, P and density, ρ values of the material after the shockwave passes by. To show implementation of the conservation of mass, momentum and energy we can look at a more specific example, demonstrated by the piston shown in Figure 2.4. We assume that this piston is at rest at the beginning and fluid has an initial pressure, P_0 and density, ρ_0.

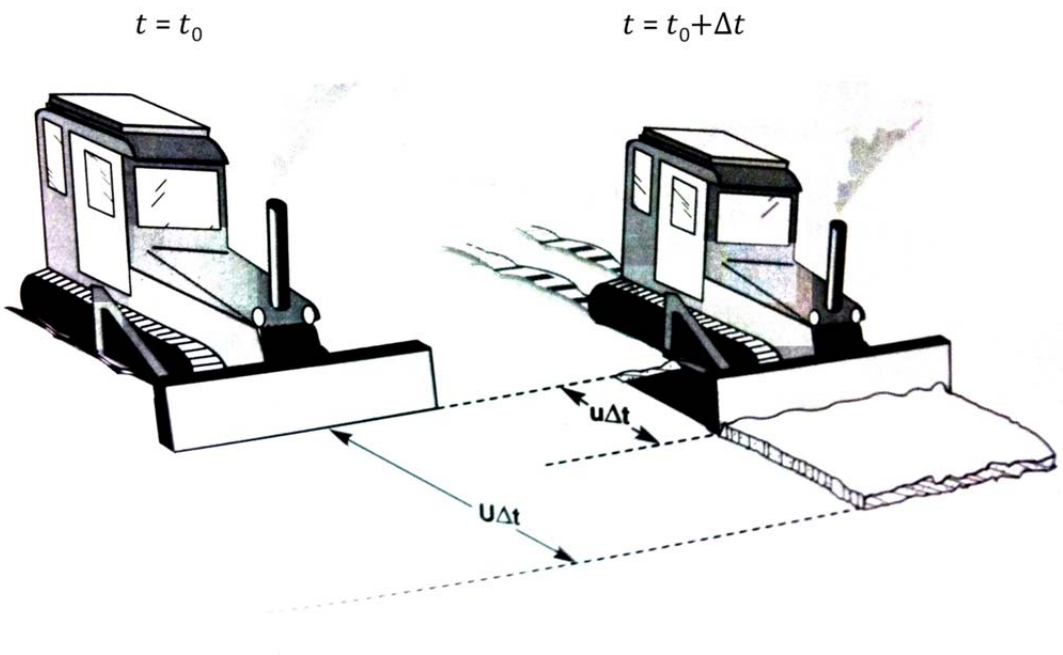

Figure 2.3 Conceptual drawing of a shock wave as an analogy to snowplow. At time $t=t_0$, plow begins to move at a velocity of u. At $t=t_0+\Delta t$, the plow has moved a distance $u\Delta t$, but discontinuity (shock wave) between the loose and packed snow has moved a length of $U\Delta t$. U is the velocity of the packed snow front[34].

When the piston is moved at a rate of U_p into the compressible fluid, similar to the snowplow example, after some Δt time the discontinuity between the highly compressed and uncompressed region moves by a distance of $U_s t_1$. The propagation of this disturbance is the shockwave velocity and the particle velocity is the piston velocity, U_p. The new density and pressure values in the compressed region are now ρ and P, respectively. Now, when we consider the conservation of mass, the relation between initial and final density values as well as the shockwave and particle velocity becomes

$$U_s \rho_0 = (U_s - U_p)\rho. \tag{2-20}$$

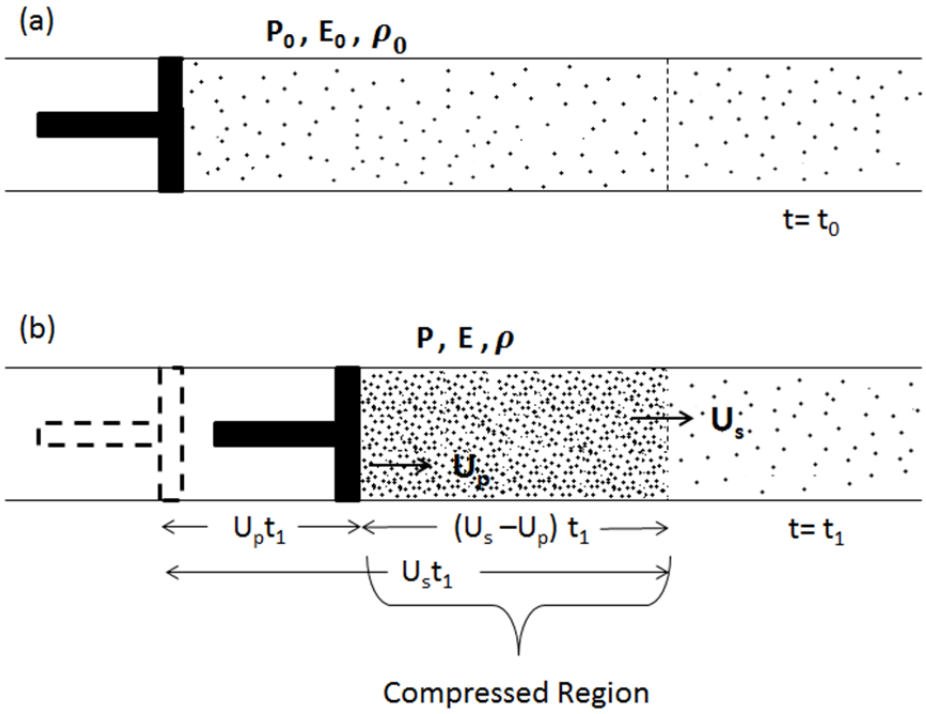

Figure 2.4 Idealized rigid piston moving and driving shock into a compressible fluid (Adapted from Ref[33]).

The above equation indicates that the initial mass of the uncompressed fluid is equal to the compressed (shocked) fluid. Since the cross section of the cylinder does not change during the compression, this term and time are dropped together from both side of the equation. The term $\rho_0 U_s$ is called "shock impedance" and explains the capability of material to produce pressure upon shock loading. Similarly the momentum conservation shows that the pressure difference between left and right of the piston is equal to the momentum transfer and can be expressed as:

$$P - P_0 = \rho_0 U_s U_p \tag{2-21}$$

where, $\rho_0 U_s$ implies the mass of the fluid, which the shock wave accelerates. Finally, the energy conservation law brings up the relation;

$$P U_p = \frac{1}{2}\left(\rho_0 U_s {U_p}^2\right) + \rho_0 U_s (E - E_0) \tag{2-22}$$

These equations (2-20, 2-21, 2-22) are also called Rankine-Hugoniot equations and have totally five variables; density (ρ), particle velocity, (U_p), shock velocity, (U_s), pressure,(P) and energy, (E). In order to express all parameters as a function of one of them, we need one more equation. This additional equation is dependent on the material property and is usually known as equation of state (EOS) of the material. EOS (equation 2-23) defines the relationship between U_s and U_p and can be obtained experimentally or theoretically,

$$U_s = C_0 + S_1 U_p. \tag{2-23}$$

where, C_0 is the material bulk sound velocity in ambient pressure and S_1 is the empirical parameter giving the relationship of two velocity types. EOS data for many materials are given in the literature, thus using this equation makes it possible to obtain the relationship between all five variables such as *P*-ρ, *P*-*V*, *P*-U_s etc. For instance *P*-U_p

(pressure – particle velocity) relation for some materials is given in Figure 2.5.

When the equations 2-20 and 2-21 are combined and solved for the U_s and U_p, the following equations for the jump conditions are obtained:

$$U_s = V_0\sqrt{(P - P_0)/(V_0 - V)}, \tag{2-24}$$

$$U_p = \sqrt{(P - P_0)(V_0 - V)}. \tag{2-25}$$

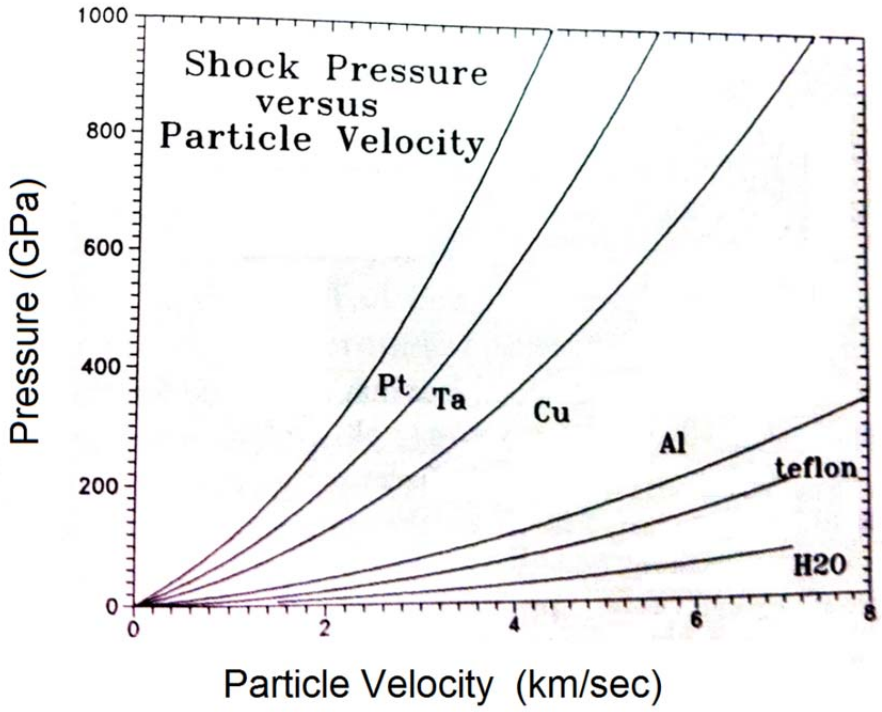

Figure 2.5 Shock pressure vs particle velocity for some standard materials[34].

Equation 2.24 can be plotted as in Figure 2.6. The initial and final states are denoted as P_0, V_0 and P_1, V_1 respectively. One should note that the Hugoniot curve is not the path of states during the shock loading. It only represents the locus states of final shock states, which are P_1 and V_1. On the other hand, the Rayleigh line, which connects

the initial and final shock states linearly (see Figure 2.6), represents the path for thermodynamic state of Hugoniot P_1 , V_1 since this line can directly express the combination of the jump conditions (equation 2-24 and 2-25).

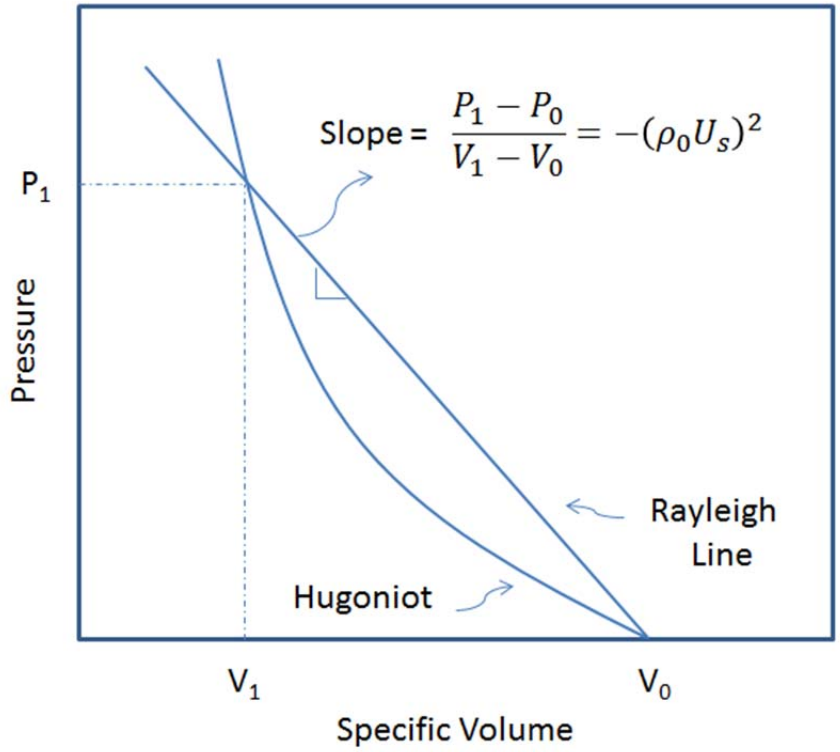

Figure 2.6 Characteristic P-V Hugoniot curve and the Rayleigh line relationship (Adapted from Ref[33]).

2.2.3 Shockwave Reflection and Spallation

When a shockwave reaches a free surface, it behaves according to the impedance rules of a wave travelling through different environments.[35] Thus, free surface acts as propagation of shock wave from high impedance to low (zero) impedance causing change in both direction and sense of the stress. Particle velocity, on the other hand, keeps its direction the same which means that if it is moving rightward it will still

continue to move right after the shockwave reaches to the free surface. Figure 2.7 explains clearly the reflection of compressive shockwave from free boundary resulting in tensile in nature. Thus, the compressive shockwave turns to be tensile after reaching the free boundary. These tensile waves are also called as rarefaction, unloading, release or decompression waves.

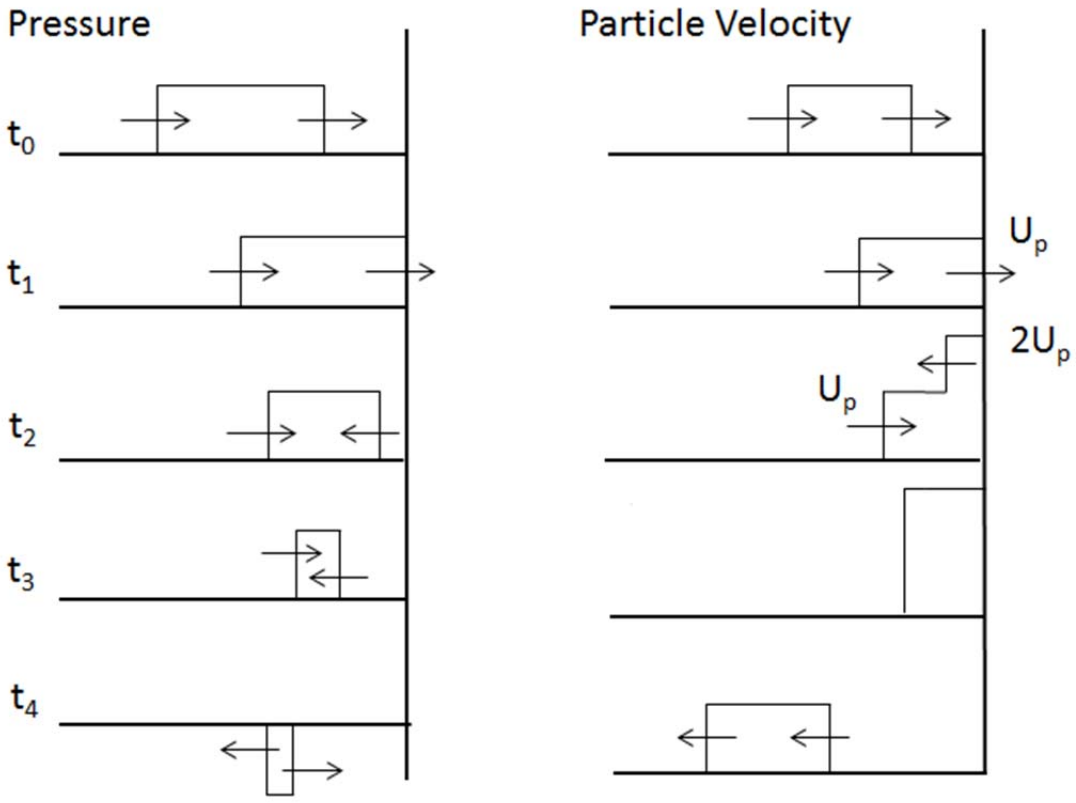

Figure 2.7 Reflection of stress and particle velocity at a free surface.

Spall fracture is a type of fracture, which occurs by the nucleation and growth of many cracks or voids over a particular region, unlike a fracture developing due to the formation and growth of a single macrocrack.[36] This special fracture type takes place only upon the interaction of stress waves.[36,37] In flyer - target type collisions, two shock waves in opposite directions are generated at the interface and travel into the flyer and

target (See Figure 2.8). When these two compressive shock waves reach the free surfaces, they turn back to the impact surface in the rarefaction form which is tensile in nature. Since the flyer size is half of the target, two tensile waves meet approximately at the mid-plane of the target, which is called the spall plane. This maximum tensile stress created by the combination of two waves that initiates the spallation process is called the spall strength.[36] Spall strengths are not material properties and depend on the loading conditions.

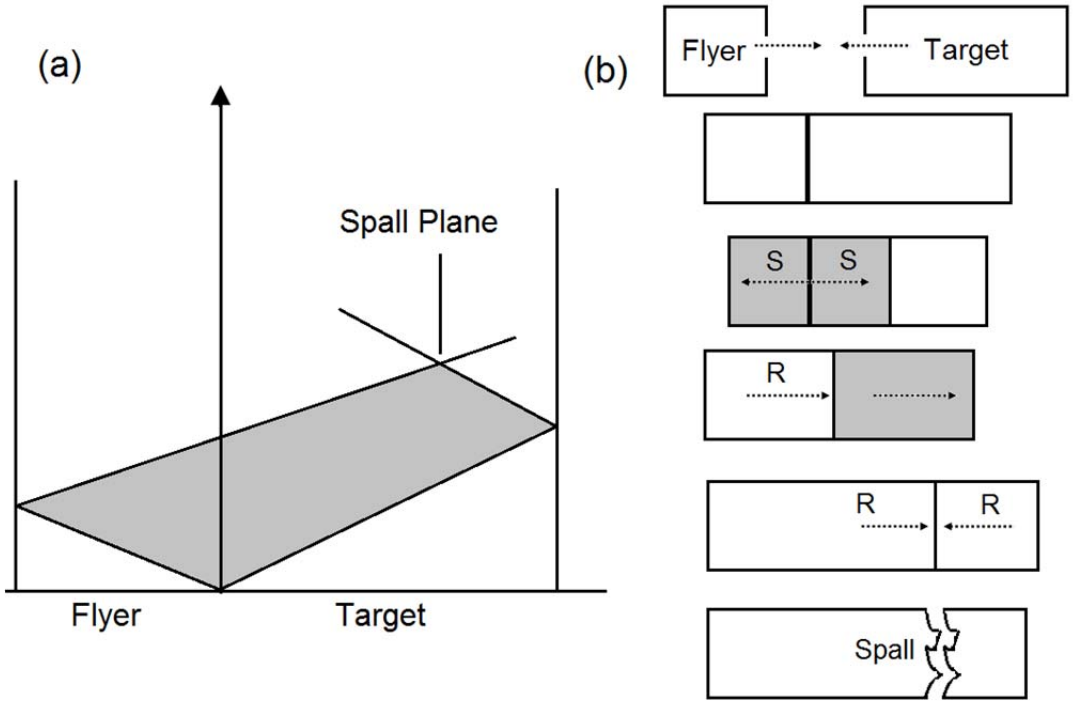

Figure 2.8 Schematics for spallation process upon shock loading. (a) the x-t diagram for shock loading. (b) Grey area is the shocked region (S), release; R.

2.2.4 Surface Velocity

In shock wave studies, measuring the free surface velocity, u_{fs}, may gain importance to deduct the particle velocity, u_p, behind the shock front. u_{fs} and u_p are related through the equation:[38,39]

$$u_{fs} = u_r + u_p \tag{2-26}$$

In this equation, u_r is the release wave which is originated at the free surface and along an isentrope it becomes

$$u_r = \int_0^{P_H} \left(-\frac{dP}{dV}\right)^{-1/2} dP|_{isentrope}. \tag{2-27}$$

Here, P and V stand for pressure and specific volume. Figure 2.9 shows schematics of Hugoniot (the curve OH) for the pressure versus volume plot. U_p is the velocity at the shock state H and surface velocity, u_{fs}, is the velocity at the zero pressure which is released from the shock state along the *HR* isentrope. However, since the release isentrope is generally not known, the equation (2-27) becomes useless.[38] Walsh and his co-workers, on the other hand, made an approximation based on the lower and upper bounds of the u_r/u_p ratio and found that it is close to 1 up to 45 GPa for Cu resulting in $u_p = \frac{1}{2}u_{fs}$. This approximation was well accepted by other authors.[34,40] MD simulations can be used as a totally independent approach to calculate the surface velocities in order to validate the experiments as well as the strength of the predictions of our simulations.

2.2.5 Experimental Techniques

Shock compression experiments are first implemented for military applications such as armor and damage tests. After the World War II, the nuclear weapon research re-

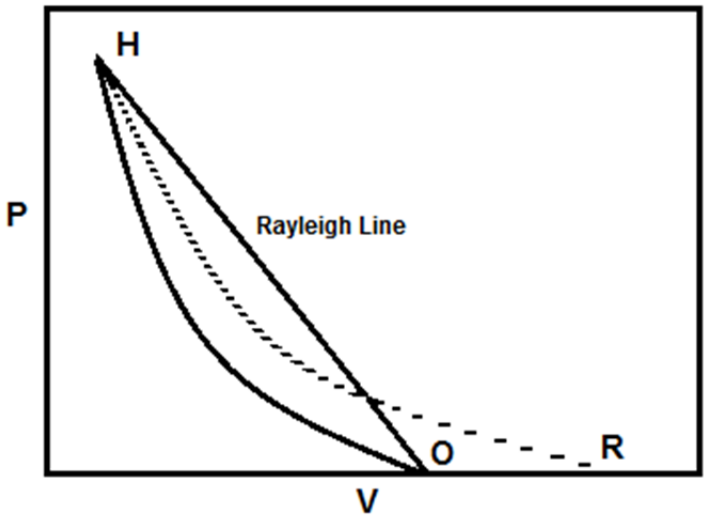

Figure 2.9 Schematics of Hugoniot (OH curve), HR is the isentropic release paths and OH straight line is the Rayleigh line (Adapted from Ref[38]).

quired to perform experiments to obtain the Hugoniot data for various materials.[34] For this need the pressure, volume or energy values at locus points after the shock compression should be recognized. In order to get reliable and healthy results, the shock front generated at the test specimen should be planar and the pressure should be uniform. Additionally, besides post-mortem damage analyses, to obtain the shock wave and the particle velocity values, new instruments needed to be developed. After achieving progress in plane wave experiments and diagnostic tools to analyze the Hugoniot data, shock compression science in materials became a well-studied discipline.[41,42] Besides Hugoniot data, other material properties such as phase transitions, chemical activity and melt boundaries were also studied.[43]

During planar shock compression, while the material faces a significant strain in the shock direction, the strain values in the two lateral directions are equal to zero. However, at finite lateral dimensions, the edge effects traveling at the speed of sound can affect the uniaxial strain nature of the compressed material.[34] Thus, early measurements during the shock compression experiments are imperative in order to cancel the lateral boundary-edge effects. In general, there are three types of experiments

used for creating a planar shock compression. These experiments use one of the followings: *i)* explosives or *ii)* guns or *iii)* energy deposition.

In explosive-driven shock experiments, a planar detonation front is generated by the explosion and this creates a planar shock front in the specimen. This method is also called explosive plane-wave generator (Figure 2.10). Early designed plane-wave generators, depending on the impedance of material ($\rho_0 U_s$), can create shock pressures at several tens of GPa.[44,45] One weakness of the early explosive plane-wave generators is the limited and poor duration of the peak shock pressure values. However, using a flyer plate and giving an acceleration via the plane-wave generator greatly increases the initial peak pressures (~ a few hundreds of GPa).[46,47]

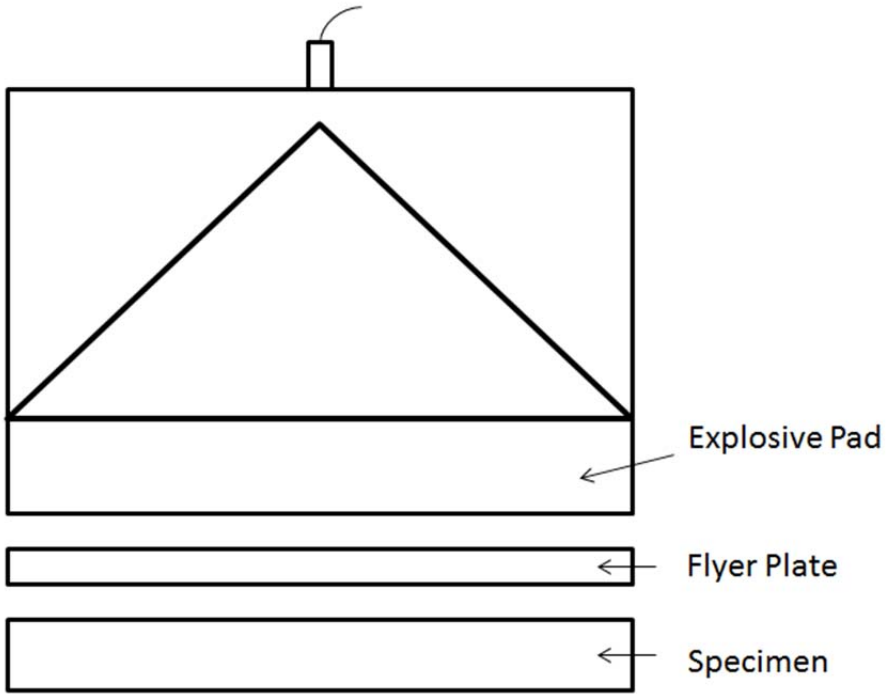

Figure 2.10 Explosive plane-wave generator using flyer plate for planar impact on a specimen (Adapted from Ref[34]).

Guns can also be used to accelerate a flat projectile to make the impact onto a flat specimen in order to generate planar shock waves. This type of shock experiments

provides more control for the shock-pressure magnitude and unloading conditions in comparison to the explosive based shock experiments.[48] Two-stage light gas guns are the most advanced guns with which high impact velocities can be achieved (Peak velocities of 7 – 8 km/s and peak shock pressures on the order of 1 TPa).[44,49] There is also another class of guns used for shock compression experiments; electromagnetic guns, which are produced by the electromagnetic forces. Rail guns are a type of electromagnetic guns and have the capability (theoretical) of very high projectile velocities even though there are still some improvements needed to reach velocities above 6 km/s.[50-52]

Last method of creating planar shock waves involves energy deposition. The principle is superheating some area of a material such that it behaves as detonated explosive, which initiates a high-pressure shock in the rest of the material (unheated part). To achieve this, extreme amount of energy is exerted over an area and this region is heated instantaneously above its vaporization temperature. Lasers or particle beams have been used for high energy deposition and especially the former method; laser-driven shock generation has been widely used.[53-57] In this process, lasers can be used either directly onto the specimen and cause target ablation into a high pressure plasma or used in a confined region (water or glass) enabling higher and longer pressure peaks.[58-61] Fast expansion of plasma creates high pressure compressive shock waves inside the specimen. Plasma pressures having a range of a few GPa to hundreds of TPa were reported.[54-56]

CHAPTER III

DYNAMIC RESPONSE OF $Cu_{46}Zr_{54}$ METALLIC GLASS UNDER SHOCK LOADING: PLASTICITY, SPALL, AND ATOMIC-LEVEL STRUCTURES*

3.1 Introduction

3.1.1 Metallic Glasses

Metallic glasses, similar to the oxide type glasses, are produced by rapid cooling from metallic liquids and form non-crystalline phases. Metallic glasses, unlike their crystalline counterparts, are lacking orientational long range order and having a randomly ordered structure, which gives them superior mechanical properties.[5]

The first metallic glass was developed in 1960 by Duwez and co-workers by quenching the $Au_{75}Si_{25}$ liquid at high rates of 10^5-10^6 K/s.[62] Following that, Chen and Turnbull defined "Turnbull's criterion, which is quite useful for predicting the glass-forming ability (GFA) of the alloy to be considered as metallic glass.[63] Later on same group achieved to make a 5 mm diameter metallic glass from $Pd_{40}Ni_{40}P_{20}$ which led Pd–Ni–P type glasses to be considered as the first bulk metallic glasses.[6] During these years, Inoue from Japan, developed $Mg_{65}Cu_{25}Y_{10}$ metallic glass[64], which has the highest GFA and also Zr-Al-Ni-Cu type glasses up to 15 mm casting thicknesses.[65] These successful attempts expedited the development of bulk metallic glasses and by developmentof"Vitreloy1"[66]($Zr_{41.2}Ti_{13.8}Cu_{12.5}Ni_{10}Be_{22.5}$) metallic glass by Johnson and his coworkers from Caltech, the effort in metallic glass research for mechanical and structural applications has increased tremendously.

---

*Part of this chapter is reprinted with permission from "Dynamic response of $Cu_{46}Zr_{54}$ metallic glass to high-strain rate shock loading: Plasticity, spall, and atomic-level structures" by Arman, B., Luo, S. N., Germann, T. C and Cagin, T., 2010. *Physical Review B* **81,** 144201. Copyright 2010 by APS publishing.

In the production of metallic glasses, melt spinning is the most used technique for quenching the liquid. However, there are other methods besides quenching such as physical vapor deposition method, which enables "amorphous alloys" in thin film forms. Before going further, we should point out that using "amorphous alloy" terminology for metallic glasses is very common and the main reason for this is that amorphous alloys can include all other methods rather than only quenching. Making amorphous alloys by damaging crystalline materials and transforming them to amorphous states is also possible. Damaging can be made by irradiation (ion, electron or neutron), ion implantation or mechanical alloying.[67-70]

In the process of producing amorphous alloys, one essential parameter is the relative size of the elements in the alloy. When the atomic size ratio gets bigger, the alloy becomes harder to crystallize, thus it possesses higher glass-forming ability.[71-73] For instance Johnson and his coworkers[66] showed excellent glass forming ability for $Zr_{41.2}Ti_{13.8}Cu_{12.5}Ni_{10.0}Be_{22.5}$ metallic glass. The cooling rate for retaining the glass was very low (10 K/s or less) and large samples up to 14 mm in diameter were able to prepared due to the large differences in atomic sizes of the elements of the metallic glass.

Revealing the atomic structure of metallic glasses is not straightforward due to the lack of long-range order, which is seen in crystalline materials. It is shown that metallic glasses have higher density values than the conventional amorphous oxides and slightly lower values from their crystallized states. These high density values suggest a randomly packed atomic configuration. TEM and diffraction methods indicate that short-range order (SRO) and also some degrees of medium-range order (MRO) structures exist in metallic glasses.[74-76] These SRO structures are mainly icosahedral type clusters and will be explained in detail in the incoming sections.

Some mechanical properties of "Vitroley" metallic glass are compared to similar crystalline metal and tabulated in Table 3.1. It is seen that metallic glass has higher elastic strain limit (~ 2%) than that of the metallic alloy, Zr 702[77] (~ 0.25%). This leads to much higher yield strength, σ_y, (~ 1.9 GPa) in metallic glass, whereas crystalline alloy

achieves yield strengths at only around ~ 0.3 GPa. The endurance stress to fatigue in amorphous alloys is higher in comparison to the crystalline alloys and combination of wear resistance with these superior mechanical properties make metallic glasses attractive in many applications such as golf-club heads, cell phone cases, medical devices and high performance springs.[78,79]

Table 3.1. Material property data for "Vitroley"[80] metallic glass and for Zr 702[77] crystalline metal.

Material Property	**Vitroley**	**Zr 702**
Young's Modulus, E	96 GPa	99.2 GPa
Shear Modulus, μ	35.3	36.2
Poisson's ratio, υ	0.36	0.35
Elastic Limit	2%	0.25%
Density, ρ	6.11 g/cm^3	6.51 g/cm^3
Fatigue Limit	170 MPa	144 MPa
Melting Temperature	992 K	1579 K

However, there are some major problems in the performance of amorphous alloys. For instance having different deformation mechanism compared to the crystalline alloys makes metallic glasses very brittle and causes rapid cracking after yielding. In crystalline materials, plastic deformation is generally is carried out by dislocations, whereas in metallic glasses, deformation is controlled through highly localized shear bands restricting plasticity resulting in low ductility. In addition to that, strain hardening is observed in crystalline materials due to the dislocation mechanism and the barrier effect of grain boundaries. Since amorphous alloys do not have these mechanisms, strain softening causes the local deformation at higher rates which raises concerns about their reliability for performances.[5] The more details about deformation mechanism of metallic

glasses based on shear transformation zones (STZs) and shear banding will be given in Chapter IV.

Some studies developed laminates having alternating layers of amorphous glasses and ductile crystalline metal layers.[3,81] The aim in these experimental works is to limit the shear band propagation or to create multiple shear bands, resulting in increased plastic strain and ductility can be increased. Other approaches to improve the ductility involve two-phase (metallic-glass-matrix)[5] composites by distributing or inhibiting shear bands include nanocrystal, particle, dendritic phase or fiber based reinforcements. Among these it is observed that the dendritic composites are more powerful at preventing plastic deformation of the glass matrix.[82-84]

3.1.2 MD Shock Simulations

Even though molecular dynamics may not be perfect for every system due to its computationally intensive nature, for shock analyses MD becomes very useful due to the short time scales of shock propagation. Laser-driven shock waves, for instance, are being studied at the size scales of tens to hundreds of nanometers for picoseconds time scale,[85-88] which is very suitable for modern MD simulations. In 1950's first MD simulation for calculating equation of state (EOS) under extreme conditions was successfully applied at Los Alamos National Laboratory.[89] Despite the fact that simulation size is only about 100 atoms, the results were surprisingly good to estimate the thermodynamic limit for the EOS. Nowadays, with the advancement in computational resources, studies of shock waves for polycrystalline systems[90] or ejecta from shocked surfaces[91] having 30 – 40 million atoms can be performed using MD codes. MD methods are also advantageous in revealing atomic-scale structure evolution and related physics,[92-95] simulation of shock wave loading for studying equation of state, plasticity or spall damage.[89,96]

In MD simulations, there are three main methods to create a shock wave:[97] 1) Pushing the material by an infinitely massive piston having a velocity of u_p analogous to the shock loading example explained in Chapter I. The same shock wave can also be

generated by assigning the velocity, u_p to the material and hurling it to the motionless piston. 2) By hitting a flyer plate to a target at specific u_p values similar to the real-life shock-wave experiments. The flyer can have an initial value of $2u_p$ or both flyer and target can have initial velocity values making the impact symmetric. By this way a shock wave at the interface upon collision is created and it travels to both plates. 3) The symmetric impact can also be generated by shrinking the longitudinal periodic length.[98] It is observed that for both shock- and release-wave type simulations, the first two methods have been used mostly to generate the shocks.[97]

3.2 Model System Preparation

To describe the Cu-Cu, Zr-Zr, and Cu-Zr interactions in the Cu-Zr alloys, we adopt the Finnis-Sinclair type interatomic potential[19] developed by Mendelev *et al.*[99] As mentioned previously in the second chapter, for the Finnis-Sinclair potential a pairwise contribution is added to the many-body term giving the following form for a system with N atoms.

$$U = \sum_{i=1}^{N-1} \sum_{j=i+1}^{N} P(r_{ij}) + \sum_{i=1}^{N} \Phi_{t_i}(\rho_i) \qquad (3\text{-}1)$$

Here, $P(r_{ij})$ denotes the pairwise potential and includes electrostatic and repulsive contributions. The second term is on the other hand, is a function of electron density, ρ_i, and based on the *second moment approximation*[10] it varies with the square root (burada leache ref ver), which assumes for each atom the local electronic binding energy is approximately equal to the square root of the number of neighbors. The electronic density is:

$$\rho_{i=} \sum_{j=1, j\neq i} \phi_{ij}(r_{ij}) \qquad (3\text{-}2)$$

where, $\Phi_{ij}(r_{ij})$ is a short-range function depending on the distance between the atoms i and j. This density function can also take other forms such as, parabolic function of $(r_{ij}-r_c)^2$, where r_c is the cutoff making $\Phi_{ij}(r_{ij})$ zero beyond this cutoff distance. Analytical expressions have been obtained for P, Φ and ϕ (eight functions in total) via fitting to some known properties of pure elements and *ab initio* Cu-Zr formation energies.[99] This potential reproduces experimental x-ray diffraction data on amorphous Cu-Zr alloys, and predicts reasonably well the elastic moduli.

Our MD simulations are performed with the LAMMPS package.[100] The initial configuration, composed of 4000 atoms with randomized positions, is subjected to incremental heating to 2000 K and then cooling to 300 K at ambient pressure, and forms a $Cu_{46}Zr_{54}$ metallic glass. This Cu-Zr model is especially chosen because it is reported that the simple $Cu_{46}Zr_{54}$ glass can be cast into 2 mm amorphous strips successfully using copper casting method.[101] The constant-pressure-temperature (NPT) ensemble and three-dimensional periodic boundary conditions are applied. The time step for integrating the equation of motion is 2 fs. The heating and cooling rates are 20–100 K per 20–100 ps, i.e., 0.2–5 K ps^{-1}. This glass is further equilibrated for 100 ps at ambient conditions, and achieves an atomic volume of 18.47 $Å^3$, corresponding to an initial (ambient) density of ρ_0=7.06 g cm^{-3}. We calculate the radial distribution functions (RDF) of this glass. Both RDFs and ρ_0 are consistent with previous results predicted from the same potential.[99,102] Mendelev *et al.*[102] also computed the elastic constants of CuZr glasses at ambient conditions, and the bulk modulus $B \approx 116$ GPa and shear modulus $\mu \approx 21$ GPa for $Cu_{46}Zr_{54}$. Thus, the Poisson's ratio $\upsilon \approx 0.415$; the bulk and longitudinal sound velocities are c_B=4.0 km s^{-1} and c_L=4.5 km s^{-1}, respectively. This 4000-atom glass is replicated along three orthogonal directions and equilibrated further with the NPT ensemble at ambient conditions for shock simulations on larger systems, in order to remove possible artifacts from the replication process. The structures of the resulting glasses are indistinguishable from that of the small system. The exact glass structure may vary modestly overall for small changes in cooling rate and relaxation process affordable by current MD simulations,[103] and Duan *et al.* showed recently that the cooling rates

(similar to ours) have a slight effect on such properties as the glass transition temperature.[101] We expect that our simulations with current glass configuration largely represent general features of the dynamic response of metallic glasses to shock loading. Planar shock-spall simulations are conducted with the flyer plate-target configuration described below and the microcanonical ensemble.[89,95] The shock loading is along the *x* axis. Periodic boundary conditions are applied only along the *y* and *z* axes, and thus free surfaces normal to the *x* axis are present on the nonimpact sides of the flyer and target. The flyer and target are constrained along the *y* and *z* axes, but can undergo compression or tension along the *x* axis. Such loading induces 1D strain as in planar shock wave experiments.[33,35,36,43,47] The time step for integrating the equation of motion is 1 fs, and the run durations are 50–200 ps. In most of our simulations, the target consists of 768 000 atoms (approximately 8.4 nm × 8.4 nm × 200 nm in edge lengths). The flyer plate has the same cross-section area as the target, and its length is reduced by half (384 000 atoms). In addition, cross-section areas of 4.2 nm × 4.2 nm and 16.8 nm × 16.8 nm are explored to examine the (cross-sectional) size effect on plasticity and the results are similar; a target length of 1.2 μm is also attempted for better separating the elastic precursor and the plastic shock. We denote the desired steady shock state particle velocity as u_p. Figure 3.1 describes schematically how the shock waves are generated using flyer-target plate impact.

The flyer plate and target are assigned initial velocities of $\frac{4}{3}u_p$ and $-\frac{2}{3}u_p$, respectively, before impacting each other, so that the flyer-target system has zero center-of-mass velocity. The impact yields shock waves propagating into the target and the flyer plate, which are then reflected at the respective free surfaces as centered simple rarefaction (release) fans, and their interaction induces an evolving tensile region and

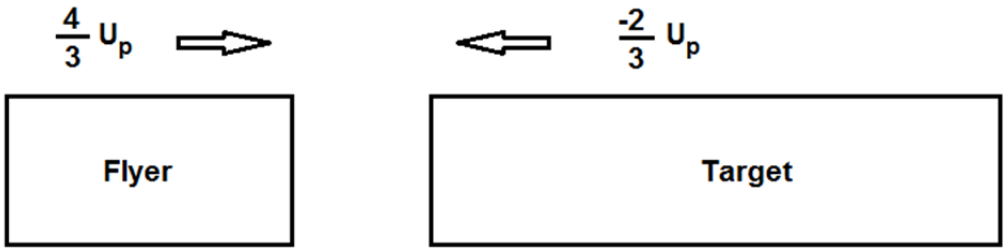

Figure 3.1 Schematic depiction showing the generating of shock wave by the impact of flyer and target (total momentum zero). The shock created will travel both into the target and the flyer.

spall in the target (for sufficiently strong shocks). The free surface velocity *vs* time (t) is obtained from the particle velocity evolution on the target free surface as $u_{\mathrm{fs}}(t)$. The atomic stress tensor σ_{ij} is calculated from the atomic virial and thermal velocity (i, j=1, 2, and 3, corresponding to x, y, and z, respectively). The binning analysis[95] is used to obtain mass density (ρ), stress (σ_{ij}), particle velocity (u), and temperature (T) profiles along the x axis. By binning, averages of the desired properties along the direction of shock wave propagation, (x axis in our case), are calculated for each rectangular bin (5 Å is chosen as the bin size) so that clear shock profiles can be extracted.

Two techniques for characterizing the short-range order in amorphous metallic glasses are the Honeycutt-Andersen analysis[101,104] and the Voronoi tessellation analysis,[105-112] and the latter is adopted here. Construction of Voronoi polyhedra is a well-studied complex exercise used in computational geometry and the details about the algorithm and the organization of the computation is available.[15] In this method, each atom is surrounded by a convex polyhedron based on predefined rules making possible to determine the neighborhood of an atom uniquely. Each atom is indexed with the Voronoi indices, i , j ,k, l , . . ., characteristic of the Voronoi polyhedron centered at this atom and consisting of its nearest neighbors (as determined from the first minimum in RDF). The center atoms can be Cu or Zr. Four indices are sufficient for our purpose, and the integers i, j, k, and l denote the numbers of Voronoi polygons, namely, triangle, tetragon, pentagon, and hexagon obtained via the Voronoi polyhedron decomposition,

respectively; their sum corresponds to the coordination number (CN) of the center atom. For the $Cu_{46}Zr_{54}$ metallic glass, a total of seven types of Voronoi indices are considered: <0,0,12,0>, <0,2,8,2>, <0,2,8,1>, <0,3,6,3>, <0,3,6,4> and <0,1,10,2>, referred to as Types 1–6, respectively; other minor individual types are denoted collectively as Type 7. Types 1 (CN=12, full icosahedrons) and 6 (CN=13) represent the densest packing and Type 1 has highest shear resistance.[112] Types 2 and 4 are considered as distorted icosahedral structures with CN=12. Type 3 is similar to Type 2 but with CN=11. Types 5 and 6 have the highest CN (13) among Types 1–6.

As demonstrated by Shimizu *et al.*,[113] a useful parameter to characterize the shear flow in metallic glasses is the von Mises type shear strain, η^{vM}, defined for each atom *i* between the present and a reference configuration. The number of the nearest neighbors of atom *i* in the reference configuration (denoted with superscript 0; it is the unshocked configuration unless stated otherwise) is n_i^0, and the vector separation between atom *i* and each of its neighbors *j* is $\mathbf{d}_{ij}$. We seek a locally affine transformation matrix $\mathbf{J}_i$ which maps

$$\{\boldsymbol{d}_{\boldsymbol{ji}}^{\mathbf{0}}\} \rightarrow \{\boldsymbol{d}_{\boldsymbol{ji}}\}, \qquad \forall\, \boldsymbol{j} \in \boldsymbol{n}_{\boldsymbol{i}}^{\mathbf{0}}, \tag{3-3}$$

and minimizes

$$\sum_{j \in n_i^0} \left| \mathbf{d}_{ji}^0 \boldsymbol{J}_i - \boldsymbol{d}_{ji} \right|^2 \tag{3-4}$$

The strain matrix follows as

$$\boldsymbol{\eta}_i = \frac{1}{2}(\mathbf{J}_i \mathbf{J}_i^T - \mathbf{I}), \tag{3-5}$$

where $\mathbf{I}$ is the unit matrix, and the local shear strain for atom *i* (a scalar) is

$$\eta_i^{\mathrm{vM}} = \left\{\frac{1}{6}[(\eta_{11}-\eta_{22})^2+(\eta_{22}-\eta_{33})^2+(\eta_{33}-\eta_{11})^2]+\eta_{12}^2+\eta_{23}^2+\eta_{31}^2\right\}^{1/2}. \quad (3\text{-}6)$$

The effective Poisson's ratio at a shock state is related to the effective Lamé's constants (λ and μ) as

$$\nu = \frac{\lambda}{2(\lambda+\mu)}. \quad (3\text{-}7)$$

For isotropic metallic glasses under 1D strain loading, we have essentially $\sigma_{11} \geq \sigma_{22} = \sigma_{33}$ (principal stresses), $\sigma_{12} = \sigma_{23} = \sigma_{31} = 0$, and

$$\sigma_{11} = (\lambda+2\mu)\varepsilon, \quad (3\text{-}8)$$

and

$$\sigma_{22} = \sigma_{33} = \lambda\varepsilon, \quad (3\text{-}9)$$

where ε denotes the bulk strain. It follows from equations (3-7)-(3-9) that

$$\nu = \frac{\sigma_{22}}{\sigma_{11}+\sigma_{22}}, \quad (3\text{-}10)$$

and σ_{22} is taken as the average of σ_{22} and σ_{33} directly measured in MD simulations. We also define hydrostaticity (h) for a given shock state as

$$h \equiv \frac{\sigma_{11}+\sigma_{22}+\sigma_{33}}{\sigma_{11}+\sigma_{22}}. \quad (3\text{-}11)$$

We use the von Mises yield criterion[114] to define the yield strength under shock compression since for metallic glasses this criterion was suggested as appropriate by a

number experimental studies.[115-117] The von Mises based yielding defines the failure when the energy of distortion becomes equal to the energy for yield (failure) in uniaxial

Table 3.2 Shock and spall parameters for the $Cu_{46}Zr_{54}$ glass. The target dimensions are 8.4×8.4×200 nm^3. The units for velocity, stress, temperature and strain rate are km s^{-1}, GPa, K and 10^9 s^{-1}, respectively.

u_p	$\boldsymbol{\sigma_{11,H}}$	$\boldsymbol{\sigma_{22,H}}$	$\boldsymbol{\sigma_Y}$	$\boldsymbol{\nu}$	$\boldsymbol{h}$	$\boldsymbol{T_H}$	$\boldsymbol{T_{sp}}$	$\boldsymbol{\sigma_{sp}}$	$\dot{\boldsymbol{\varepsilon}}$
0.125	4.22	3.06	2.00[a]	0.420	0.82	315	300	4.0[b]	…
0.250	8.39	6.32	1.98	0.432	0.84	330	305	6.8[b]	…
0.375	12.32	10.29	2.01	0.456	0.89	350	330	9.0[b]	…
0.500	16.33	14.62	1.74	0.472	0.93	380	370	10.6	1.8
0.750	25.22	24.17	1.06	0.489	0.97	480	450	11.0	8.6
1.000	35.57	35.00	0.56	0.496	0.99	600	550	11.2	17.4
1.500	59.75	59.64	0.10	0.499	1.00	1200	870	9.6	26.2

[a]Assuming the value of $\boldsymbol{\sigma_Y}$ at the HEL.

[b]The maximum tensile stress achieved; no spallation.

tension. Based on this the yield strength will become

$$\sigma_Y = \sqrt{3J_2} \tag{3-12}$$

where the second deviatoric stress invariant

$$J_2 = \frac{1}{6}[(\sigma_{11} - \sigma_{22})^2 + (\sigma_{22} - \sigma_{33})^2 + (\sigma_{33} - \sigma_{11})^2] + \sigma_{12}^2 + \sigma_{23}^2 + \sigma_{31}^2 \tag{3-13}$$

σ_y is equivalently the yield stress under uniaxial stress.

3.3 Hugoniot States, Plasticity, and Spallation Phenomena

MD shock simulations are explored for $0.125 \leq u_p \leq 1.5$ km s^{-1}, yielding results on elastic and plastic deformation, shear strengths, supported shock states (Hugoniot states) and spallation. The wave propagation and interactions related to shock, release, tension and spall are illustrated with density evolution as viewed in a traditional $x - t$ diagram (Figure 3.2). The impact-induced shocks, the subsequent release waves originating at free surfaces and the interaction of the opposing release waves, yield well-defined shock, release, tensile and spall regimes in the x–t diagram. Figure 3.3 shows the corresponding stress profiles at selected t with a spall zone indicated. Upon spall, the tensile stress is reduced, inducing (re)compression waves propagating toward the free

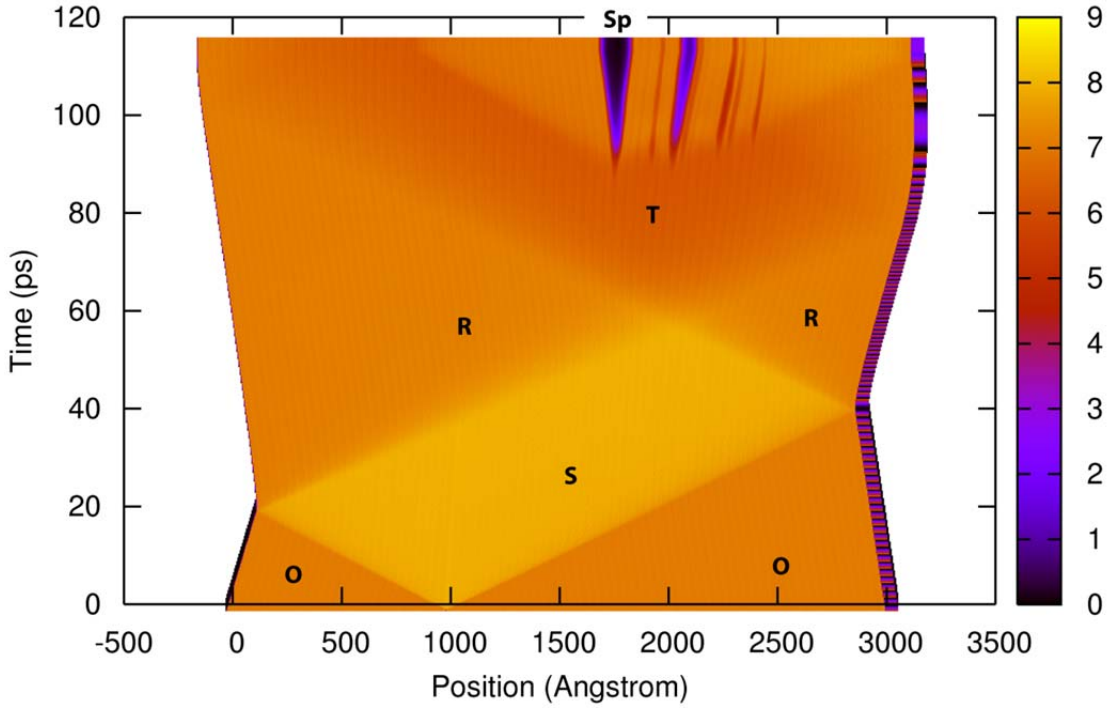

Figure 3.2 The x–t diagram for shock loading of the $Cu_{46}Zr_{54}$ glass with $u_p = 0.5$ km s^{-1}. Color coding is based on local mass density $\rho(x)$ in g cm^{-3}. Region *O*: unshocked; *S*: shocked; *R*: release; *T*: tension; *Sp*: spall.

surfaces. This shock-release-spall sequence is also manifested in the free surface velocity history (Figure 3.4) similar to experimental measurements with the velocity interferometry.[118] In particular, the recompression following spall is registered in $u_{fs}(t)$ as a pullback characteristic of spallation.

A shocked solid undergoes plastic deformation at or above the Hugoniot elastic limit (HEL), and a two-wave structure (the elastic precursor and the plastic shock wave) is expected until the elastic precursor is overtaken by the plastic shock at high shock strengths. Below HEL, there exists only a single elastic shock. A two-wave structure can

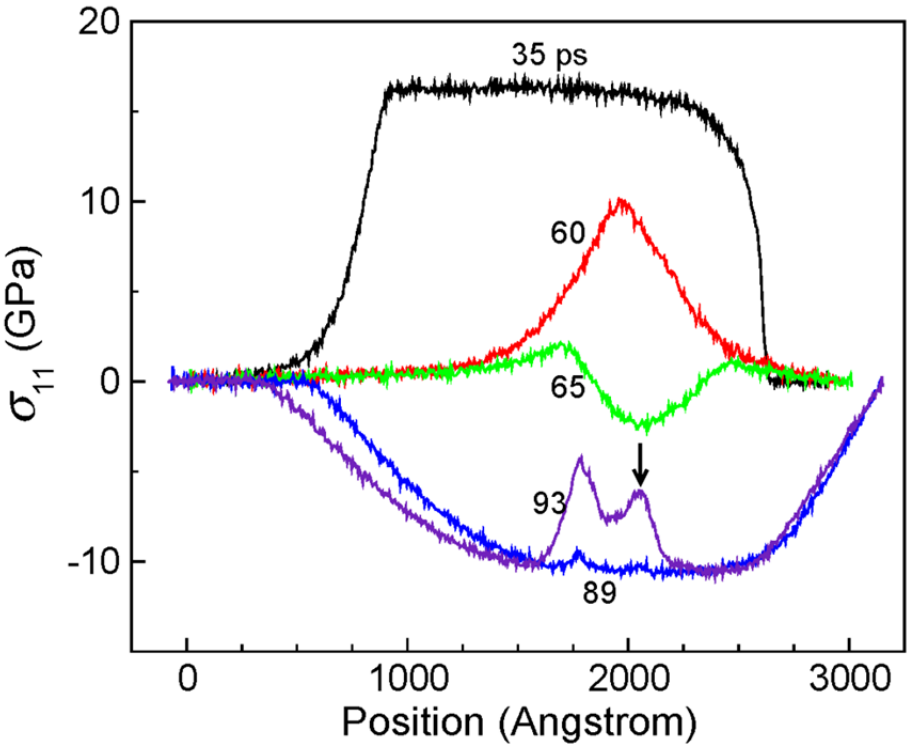

Figure 3.3 The stress profiles for up=0.5 kms−1 at selected instants showing sequentially shock, release, tension and spallation. The arrow denotes an example of spallation.

be identified in $u_{\mathrm{fs}}(t)$ and $\sigma_{11}(x)$ for u_p = 0.5 km s^{-1}; the sluggish plastic wave front following the rapidly rising elastic precursor is characteristic likely due to its particular plastic deformation mechanism different from conventional crystal plasticity[119] [Figures 3.4 and 3.5(a)]. At higher shock strengths (e.g., u_p = 1 km s^{-1}, Figure 3.4), the plastic shock overtakes the elastic precursor (the two-wave structure then becomes one-wave) and the plastic shock rise is much faster because of the facilitated kinetics of the elastic-plastic transition. The rounded transition from the shock rise to the plateau is observed near and above HEL for this metallic glass (e.g., u_p = 0.25 km s^{-1}, Figure 3.4), and below HEL, the rounding is less pronounced but the shock rise is shallower (u_p = 0.125 km

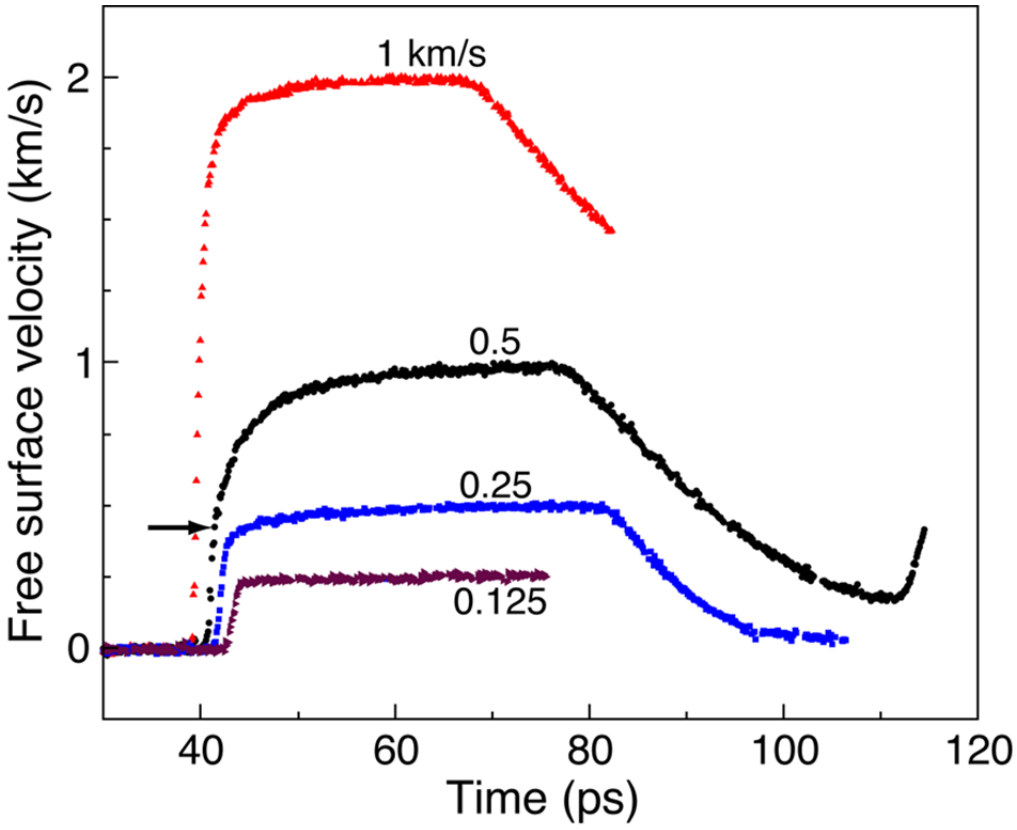

Figure 3.4 Representative free surface velocity histories for different u_p (numbers). The arrow indicates the elastic precursor. Spall pullback in u_{fs} occurs at t ~ 112 ps for u_p = 0.5 km s^{-1}.

s^{-1}). Similarly, such rounding above HEL was reported for some Zr-based metallic glasses.[120,121] Interestingly, Kanel *et al.* observed this rounding even below HEL for some shocked silicate glasses.[122,123] However, there are some exceptions.[124] We speculate that free volume and shear deformation kinetics may play a role in this rounding behavior (below and above HEL), although the exact mechanisms remain to be explored. The plateau feature in our simulations is different from the experiments on Zr-based metallic glasses,[120,121,124] possibly because of the differences in time scale.

The wave speed of the leading wave front at a given u_p, u_{s1}, can be obtained from two wave profiles at different t and is plotted in Figure 3.6 (triangles); it thus represents the elastic and plastic shock speeds before and after the overtake of the elastic precursor by the plastic shock, respectively. Three regimes can be identified (divided by HEL and the overtake): below HEL (regime I), u_{s1} increases with increasing u_p from the ambient longitudinal wave speed; between HEL and the overtake (regime II), u_{s1} remains a constant (4.87 ∓ 0.03 km s^{-1}) since the elastic-plastic transition occurs at the same stress level; above the overtake (regime III), u_{s1} increases again with u_p. The HEL is located

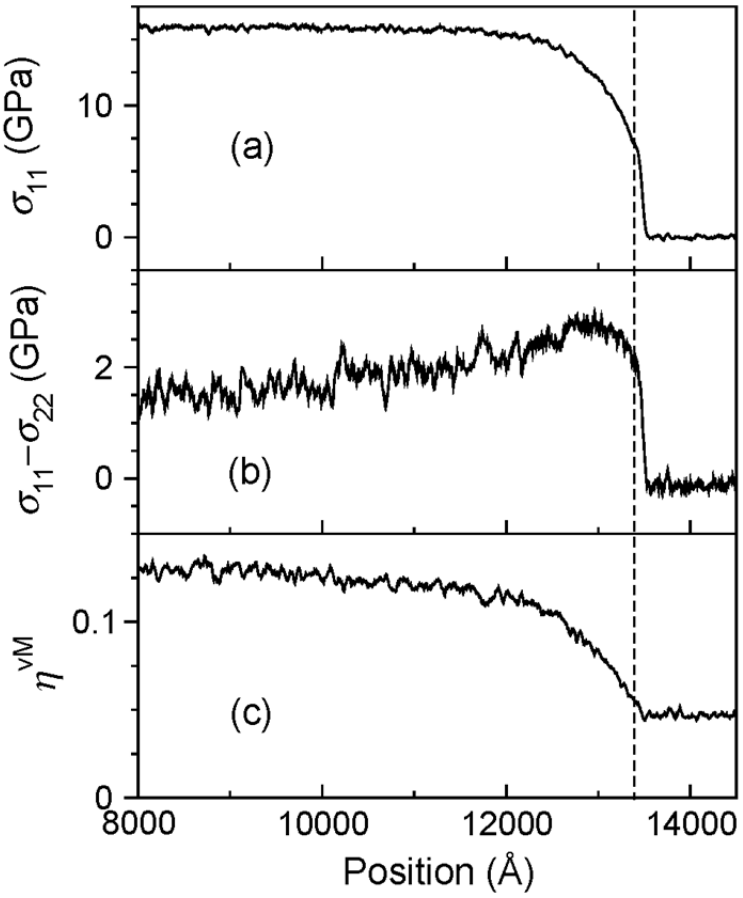

Figure 3.5 $\sigma_{11}, (\sigma_{11} - \sigma_{22}), \eta^{\mathrm{vM}}$ profiles across the shock front in the target for u_p = 0.5 km s^{-1} at t = 169 ps. The dashed line indicates the onset of the elastic-plastic transition at HEL. There exists a stress overshoot in (b) after HEL. The target dimensions are 4.2 nm × 4.2 nm × 1.2 μm.

between 0.125 and 0.25 km s^{-1}, and the overtake occurs at $u_p \approx$ 0.8 km s^{-1}. The HEL can be measured more accurately as the amplitude of the particle velocity or σ_{11} of the elastic precursor [e.g., from $\sigma_{11}(x)$ and and $u_{\mathrm{fs}}(t)$]: (HEL is about 7.2 $\mp$ 0.4 GPa [Figure 3.5(a)] and $u_{p,\mathrm{HEL}}$ is about 0.21 $\mp$ 0.01 km s^{-1} (Figure 3.4; the particle velocity doubles on the free surface); they are consistent with each other using the momentum conservation jump condition.[35]

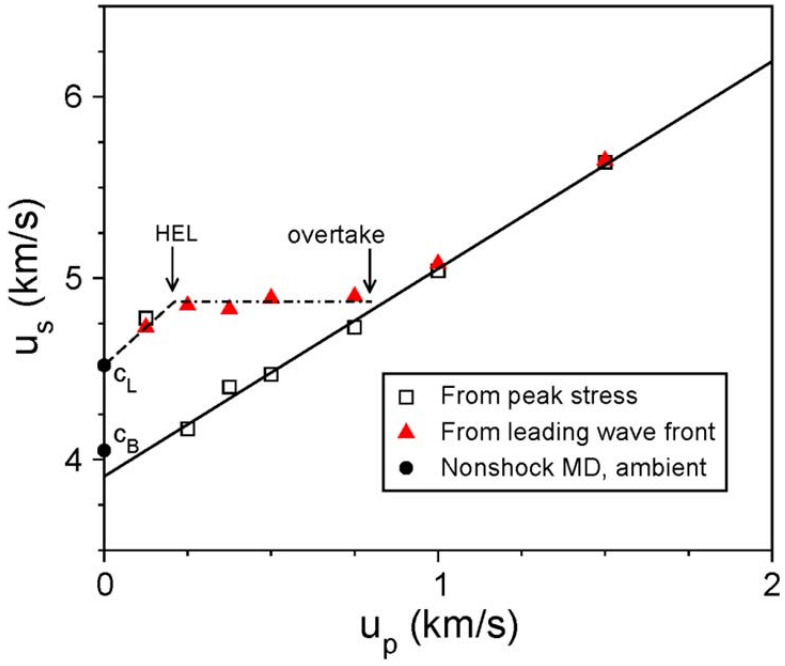

Figure 3.6 The shock velocity (u_s, squares) along with the leading wave front velocity (triangles) plotted as a function of u_p. c_L and c_B are deduced from Ref.[102]

$$\sigma_{HEL} = \rho_0 u_s u_p\big|_{HEL}, \tag{3-14}$$

and u_s = 4.87 km s^{-1}. The HELs of some Zr-based metallic glasses determined from shock experiments are between 5–7 GPa (mostly around 7 GPa),[120,121,125,126] consistent with our simulations here. Linear extrapolation of the values of u_{s1} at and below HEL to u_p= 0 yields 4.5 km s^{-1}; this value is essentially the longitudinal sound speed (c_L) at ambient condition, and agrees with the previous result.[102]

The shock plateau is largely developed as seen from the free surface velocity histories or the wave profiles within the bulk, from which the supported shock or Hugoniot states (H) at a given u_p can be deduced, including σ_{ij}, ρ, and T as well as shock velocity u_s (Table 3.2 and Figure 3.6). In regimes I and III (with a single elastic and

plastic shock wave, respectively), the Hugoniot jump condition is applied between the ambient and final shock states

$$\sigma_{11,H} = \rho_0 u_s u_p. \quad (3\text{-}15)$$

In regime II with split elastic and plastic waves, we consider two successive applications of the jump condition: from the ambient condition to the HEL [Equation (3-14)], and from the HEL to the final plastic shock state,

$$\sigma_{11,H} - \sigma_{11,HEL} = \rho_{HEL}(u_s - u_{p,HEL})(u_p - u_{p,HEL}). \quad (3\text{-}16)$$

In contrast to u_{s1}, direct measurement of u_s is difficult due to the sluggish elastic-plastic transition (as well as computational limitations on the simulation size). u_s is calculated with equations (3-15) and (3-16) instead. u_s becomes u_{s1} in the elastic and overtake regimes as expected (Figure 3.6). Note that equation (3-16) is intended for steady flows and only approximate in our cases. The peak shock state u_s – u_p relation for the plastic wave can be described with a linear fitting

$$u_s = c_0 + s u_p, \quad (3\text{-}17)$$

where c_0=3.91 ∓ 0.04 km s^{-1} and s = 1.14 ∓ 0.03 (the solid line, Figure 3.6). Fitting to all the data points in the plastic region or those at *up*_0.75 km s−1 yields the same results. c_0 is the extrapolated u_s at u_p= 0, and is in reasonable agreement with a previous result of the bulk sound speed c_B (4.0 km s^{-1}) at the ambient condition[102] within simulation uncertainties. The volumetric strain

$$\varepsilon \equiv 1 - \frac{\rho_0}{\rho_H}, \quad (3\text{-}18)$$

where ρ_H is obtained with the mass conservation jump condition[35] from u_s and u_p. Direct measurement of ρ_H from $\rho(x)$ yields consistent results.

A shocked solid begins to yield when σ_{11} reaches the critical value σ_{HEL}, above which it may retain a constant shear strength (the elastic-perfectly plastic transition), or σ_y may decrease (strain softening), or increase (strain hardening) with increasing shock strength. We examine the differential stress, or $2\tau = (\sigma_{11} - \sigma_{22})$ across the shock front and σ_Y at the supported shock states. τ is the maximum shear stress, and $\sigma_Y = 2\tau$ for plastic deformation.

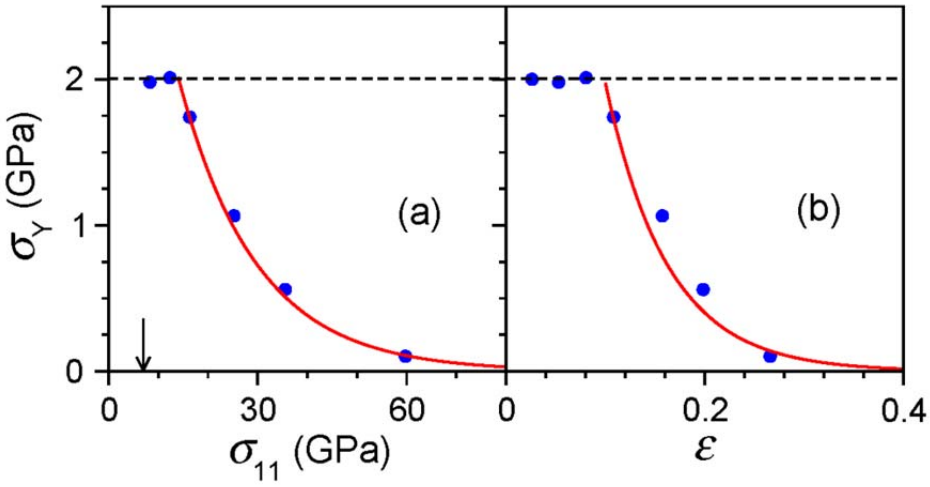

Figure 3.7 The shock-state yield strength σ_Y as a function of peak stress (a) and volumetric strain (b). Solid curves: power-law fits showing strain softening. Dashed line: the elastic-perfectly plastic transition. Arrow: HEL.

Across the shock front, the solid is elastically shocked to σ_{HEL}; the elastic shock is succeeded by a sluggish transition to plastic shock state [e.g., u_p=0.5 km s^{-1}, Figure 3.5(a)]; correspondingly, $2\tau = (\sigma_{11} - \sigma_{22})$ rises sharply in the elastic regime to about 2 GPa, overshoots to about 2.7 GPa (strain hardening) and then relaxes slowly to a steady value of about 1.7 GPa at the steady shock state. Note that this strain hardening is highly

transient compared to the ensuing relaxation, i.e., the latter is a dominant feature of the plasticity kinetics.

Assuming the von Mises yield criterion, σ_Y is also estimated at the supported shocked states above HEL (Table 3.2 and Figure 3.7) as a function of $\sigma_{11,H}$ or ε_H, and shows a power law softening in both cases. The softening is emerging only at u_p = 0.5 km s^{-1}, i.e., with a delay relative to HEL, and becomes drastic around 0.75 km s^{-1}. Since shock loading is adiabatic with an accompanying temperature rise, thermal softening is coupled with strain softening at higher shock strengths (e.g., at u_p above 1 km s^{-1}). This strain softening in metallic glasses has also been observed in quasistatic loading conditions such as nanoindentation,[127,128] and is likely due to the formation of shear transformation zones (see below) and the lack of efficient strain hardening mechanisms.[4] σ_Y approaches zero at high shock strengths (e.g., u_p =1.5 km s^{-1}), and the plastic wave overtakes the elastic wave at u_p > 0.75 km s^{-1}. Such features are unlikely caused by melting since T_H is too low at these elevated stresses (Table 3.2), but more likely due to the high Poisson's ratio and the applied stresses. At the HEL, it follows from the von Mises yield criterion that

$$\sigma_Y = \frac{1-2\upsilon}{1-\upsilon}\sigma_{HEL}. \tag{3-19}$$

For $\upsilon \approx 0.42$ (see below) and $\sigma_{HEL} \approx 7.2$ GPa, $\sigma_Y \approx 2$ GPa, consistent with its values near the onset of plasticity; see the steady state values at u_p = 0.25 and 0.375 km s^{-1} (Figure 3.7), as well as the onset strength for u_p = 0.5 km s^{-1} in Figure 3.5(b). Although σ_Y at HEL can be estimated with reasonable accuracy from σ_{HEL} and υ, it may not be used for high pressures due to possible work hardening or softening.

Given $\sigma_{ij,H}$, the Poisson's ratio and hydrostaticity are calculated for different steady shock states (Table 3.2). It is expected that increasing strain softening with increasing shock strength corresponds to increasing υ (to 0.5) and h (to 1), and this indeed agrees with our observations. The shocked metallic glass is not completely

hydrostatic at u_p < 1 km s^{-1}, and retains finite shear strength up to 1 km s^{-1}, likely due to unsaturated (but successively growing) plasticity. However, since the values of v and h are high even at the onset of plasticity, the $u_s - u_p$ relation in the plastic regime can essentially be described by a single linear relation with $c_0 \approx c_B$ (Figure 3.6). The opposing rarefaction fans encounter within the target, releasing the shock compressed region into a tensile state; when this tensile stress exceeds a critical strength, spall is initiated after some short delay. This maximum tensile stress ($-\sigma_{11,\max}$), is the dynamic spall strength σ_{sp}. σ_{11} and T in the spall region then increase due to recompression, but the average density decreases due to void nucleation and growth, which is characteristic of the spall process (Figure 3.8). Multilayer spallation is observed: $-\sigma_{11}$ can reach the spall strength at several locations throughout a broad spall zone (e.g., the profile at 89 ps in Figure 3.3), and nucleate multiple spall layers (Figure 3.2 and the 93-ps profile in Figure 3.3). Compression waves are originated at the spall zone and propagate toward the free surfaces of the flyer plate and target, inducing a pullback in $u_{\mathrm{fs}}(t)$ (e.g., u_p = 0.5 km s^{-1} in Figure 3.4). The subsequent release and compression waves are then trapped between the spall zone and the target (or flyer plate) free surface, yielding reverberations in $u_{\mathrm{fs}}(t)$ (not shown).[36]

The instantaneous tensile strain rate can be obtained from the spatial derivatives of $u_1(x)$ and $\rho(x)$ with the Eulerian mass conservation equation

$$\dot{\varepsilon} = \left(\frac{\partial u_1}{\partial x} + \frac{u_1}{\rho}\frac{\partial \rho}{\partial x}\right)\Big|_t . \tag{3-20}$$

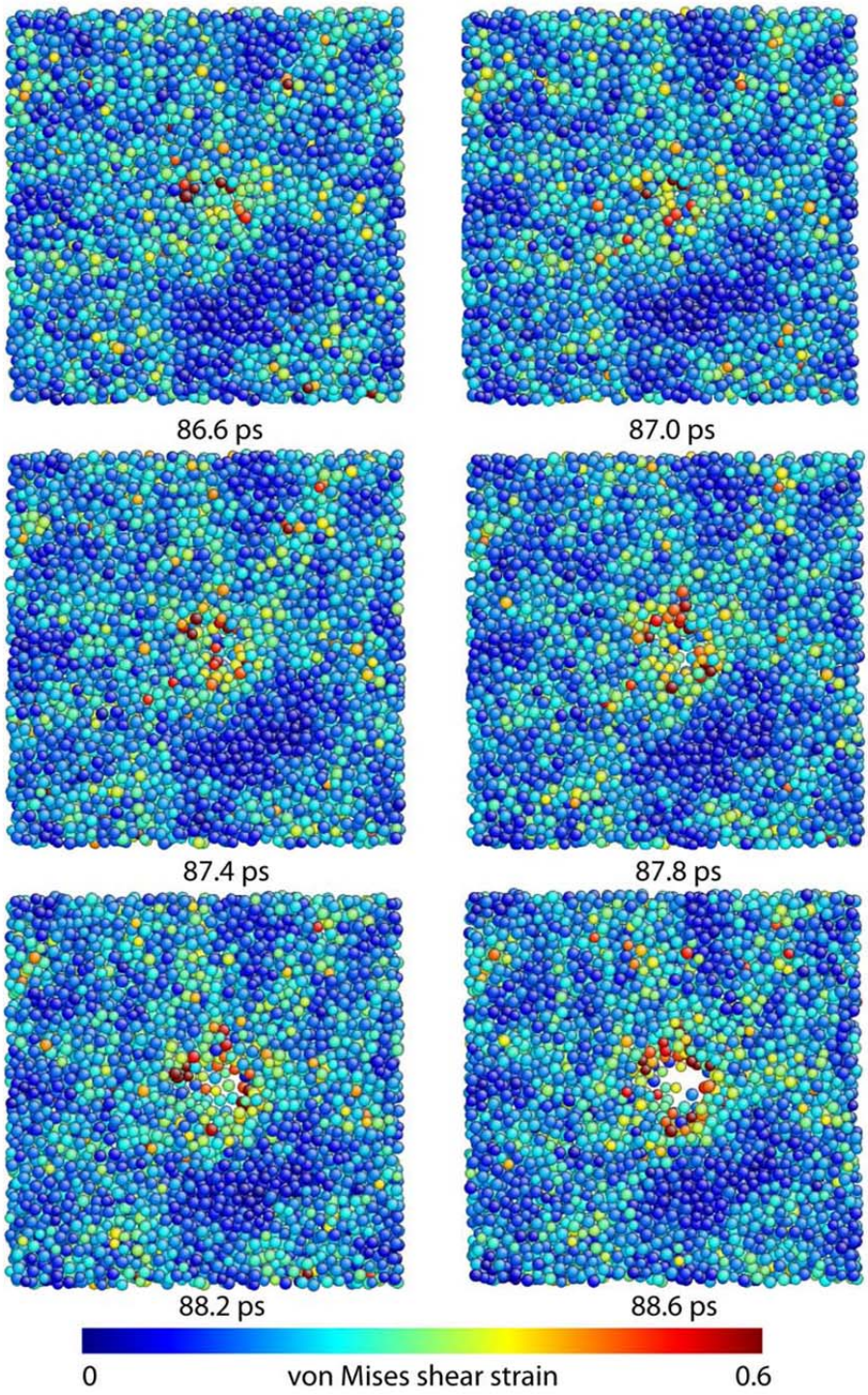

Figure 3.8 Snapshots of the atomic configurations (8.4 nm×8.4 nm cross-section) showing early stages of void nucleation and growth for $u_p = 0.5$ km s^{-1}, viewed along the shock direction. Visualization adopts AtomEye.[129]

The second term on the right hand side of equation (3-20) can be omitted near the maximum tensile stress zone (where $\partial\rho/\partial x$ is small). $\dot{\varepsilon}$ may vary with x and t, and its value in the spall zone right before the spall initiation is adopted. While higher strain rate normally increases spall strength, the temperature in the spall zone right before spallation (or simply, spall temperature $T_{\rm sp}$) has an opposite effect. Thus, the spall parameters include $\sigma_{\rm sp}$, $\dot{\varepsilon}$ and $T_{\rm sp}$. Spallation occurs at $u_p \geq 0.5$ km s^{-1} in our simulations, and the related spall parameters are summarized in Table 3.2. With increasing u_p, both $T_{\rm sp}$ and $\dot{\varepsilon}$ increase, while $\sigma_{\rm sp}$ increases then decreases due to the competing effects of $T_{\rm sp}$ and $\dot{\varepsilon}$.[95]

3.4 Plasticity and Spallation Mechanisms

Amorphous metallic glasses lack well-defined crystal lattices and, consequently, prohibit plastic deformation via long-range concerted movement of atoms. Therefore, the observed plasticity cannot be explained with the conventional crystal plasticity theory (e.g., dislocations)[119] and we resort to the local shear strain analysis in terms of $\eta^{\rm vM}$.[113]

For a configuration under consideration, $\eta^{\rm vM}$ is calculated relative to a fixed reference frame, the initial configuration prior to shock loading. Across the shock front, $\eta^{\rm vM}$ increases from its ambient value of about 0.04 in the unshocked region (due to thermal fluctuations) gradually to a steady shock state value (Figs. 3.5(c) and 3.9). For u_p=0.5 km s^{-1}, the two-wave structure in $\sigma_{11}(x)$ and the profile of $2\tau = (\sigma_{11} - \sigma_{22})$ [Figures 3.5(a) and 3.5(b)] clearly show the elastic-plastic transition which is accompanied by the accordant increase in $\eta^{\rm vM}$. While the elastic-plastic transition thickness as seen from $\sigma_{11}(x)$ is about 2000 Å, it is nearly 50% wider in $2\tau(x)$ and $\eta^{\rm vM}(x)$, indicating the shear properties appear to have slower relaxation kinetics. The shock-state $\eta^{\rm vM}$ increases with increasing u_p (Figure 3.9 and circles in Figure 3.10): it is

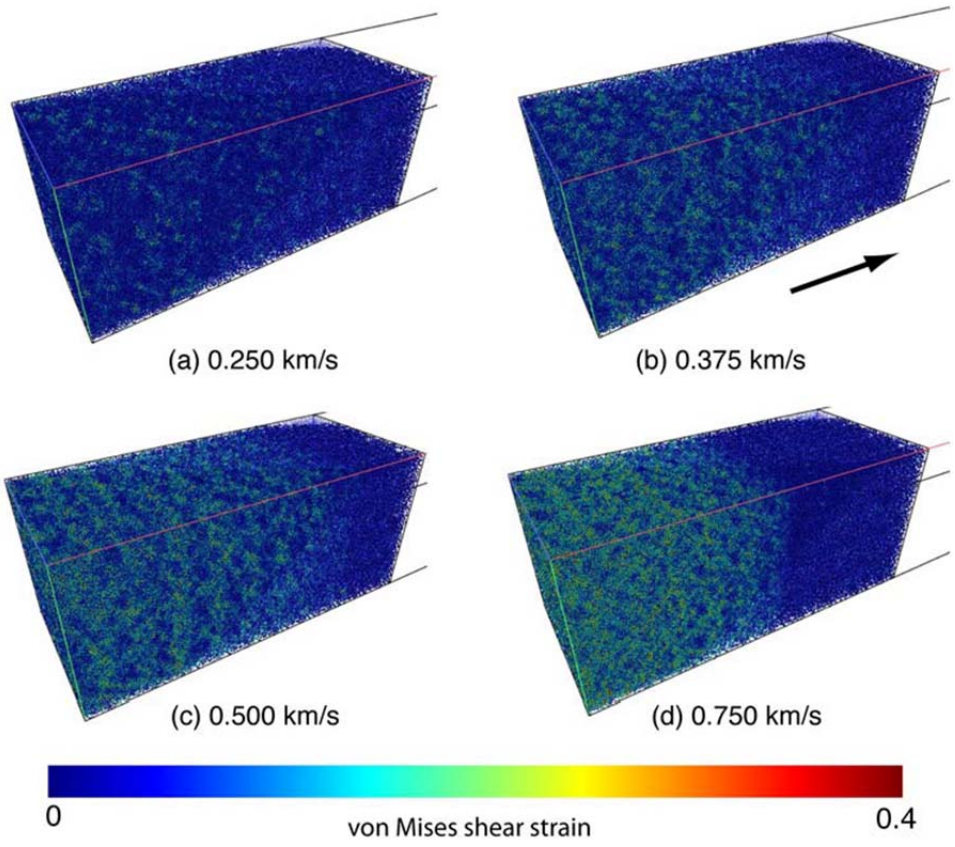

Figure 3.9 Visualization of the $Cu_{46}Zr_{54}$ glass shock-loaded at different u_p in terms of η^{vM}. The cross-section (on the *yz* plane) is 16.8 nm × 16.8 nm. The arrow denotes the shock direction *x*.

close to the ambient value below the HEL (e.g., at u_p = 0.125 km s^{-1}), becomes noticeable above the HEL, and then saturates at high u_p. The elastic precursor is not pronounced in $\eta^{\mathrm{vM}}(x)$, likely due to the low threshold of $\eta^{\mathrm{vM}} \sim 0.06$ for the elastic-plastic transition as identified from Figures 3.5(c) and 3.10; another reason is that $\eta^{\mathrm{vM}}(x)$ is averaged over a finite bin width around a given *x*, and a few nuclei will be overwhelmed by the ambient surroundings as a result. The shear strain is inhomogeneous at nm scales: the localized high shear strain zones or simply shear transformation zones (STZs) are limited in size (sub-nm in width initially) and dispersed among low shear zones. No preferred growth of certain STZs are observed in our simulations, likely due to the simulation geometry (the *y* and *z* directions are constrained rather than free). The STZs

are randomly centered, but are regularly shaped with two intersecting branches; each branch is at about $\mp$ 45° from the shock direction in the *xy* and *xz* planes, i.e., along the maximum shear stress directions as expected. Such a STZ pattern was also observed in a

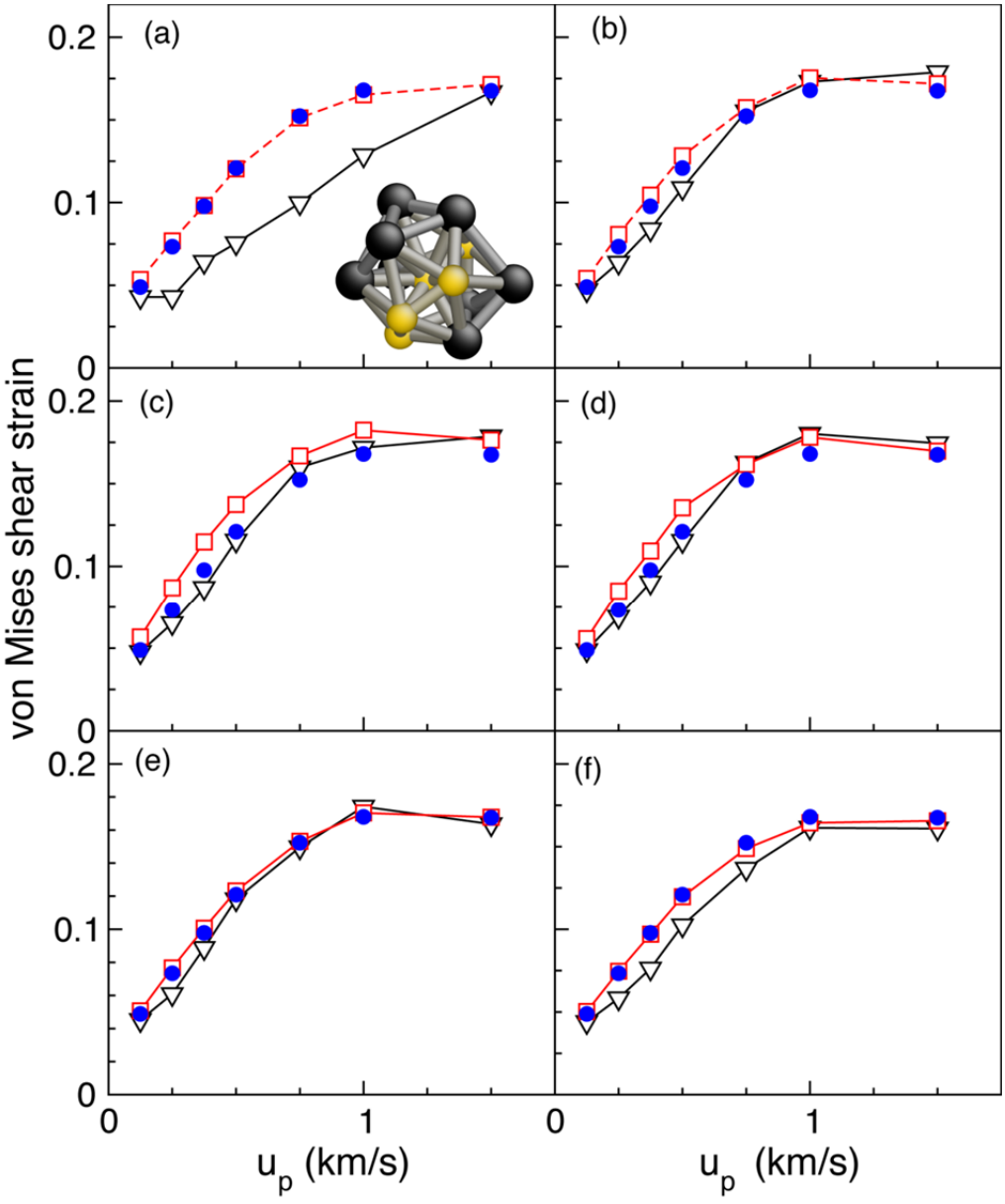

Figure 3.10 The averaged shock-state η^{vM} for the atoms conserving the original Voronoi type (or conserved; triangles), the transformed atoms (squares) and the bulk (circles). (a–f) refer to Voronoi Types 1–6, respectively. The inset to (a) is a Type 1 Voronoi polyhedron centered at a Cu atom with its 12 Cu and Zr nearest neighbors forming an icosahedron, indexed as <0,0,12,0>.

$Cu_{64}Zr_{36}$ glass sheet under uniaxial tension, simulated with an embedded atom- method potential.[130] Similarly, STZs occurred in MD simulations of ternary and quinternary glasses under pure shear and uniaxial stress loading.[103,113] STZs were examined in both nanoparticle and bulk NiZr glasses;[131,132] the STZ pattern similar to ours was found in this bulk glass with the atomic bond angle distribution peaked at 45°, while the bond angle distribution is broad for nanoparticles.[132] As noted by Schuh *et al.*,[5] STZs comprising a few to hundreds of atoms are commonly observed in computer simulations spanning a wide range of glass compositions, interatomic potentials and (nonshock) loading conditions. Thus, these previous MD simulations, together with our current work, strongly suggest that STZs are a common mechanism of plastic deformation in metallic glasses under both shock and nonshock loading conditions. The elastic-plastic transition is sluggish for u_p =0.25–0.5 km s^{-1}, and the thickness of the plastic shock wave front decreases (i.e., steepens) at higher u_p. The transition is dominated by the relaxation process of $2\tau = (\sigma_{11} - \sigma_{22})$ from its overshoot peak over HEL likely due to transient strain hardening [e.g., at about 13000 Å, Figure 3.5(b)]; this transient overshoot determines the relaxation kinetics and the plastic shock thickness. For example, the amount of overshoot increases from about 0.8 GPa for u_p =0.5 km s^{-1} to 3–4 GPa for 1 km s^{-1}, and reduces the plastic shock thickness from about 2000 Å to 200 Å accordingly. The strain hardening is also observed in some experiments,[133] and can be explained with the exhaustion of STZ nucleation sites;[134] this is indeed the case as we will show below in Section 3.5. For comparison, the observed shock-state strain softening (Figure 3.7) is also related to local structure features (Section 3.5) besides the shock heating effect, as suggested by Schuh *et al.*[5] Higher shock strength increases STZs and induces higher temperature, which in turn facilitates the plastic transformation, but this factor is possibly secondary at the onset of plastic deformation. In contrast to the rapid plasticity kinetics and high plasticity at high u_p, the slow kinetics at low u_p induce low plasticity in the shocked region, which is nonetheless in a supported shock state in our MD time scales; this underdeveloped (unsaturated) plasticity gives rise to the relatively high shear strength and low hydrostaticity at low u_p (Table 3.2 and Figure 3.7).

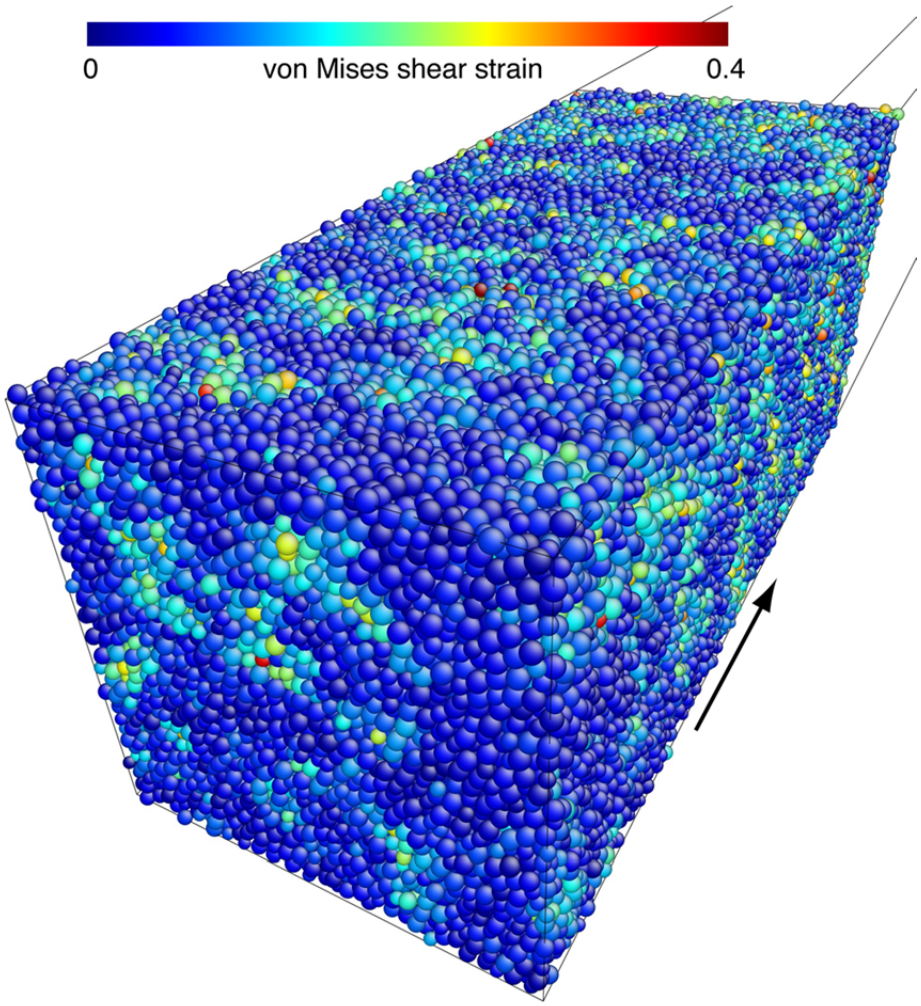

Figure 3.11 Visualization of a slice of the $Cu_{46}Zr_{54}$ glass at a fully released state (zero stress) after unloading from the shock state (u_p = 0.5 km s^{-1}). The cross-section (on the *yz* plane) is 8.4 nm × 8.4 nm. The arrow denotes the shock direction *x*. Color coding is based on η^{vM}.

We also calculate the local atomic temperatures during shock loading and compare them with the corresponding η^{vM} and no good correlation between T and η^{vM} is found, i.e., the temperatures in the STZs are comparable to those in the low shear zones. Local temperature variations are not the cause for STZ (the local structures are instead, see Section 3.5), and not the effect of STZ, either. The latter is probably attributed to the slower kinetics in thermalization than strain relaxation upon shock loading with finite

shock thicknesses. Thus, initiation of STZ is of structural rather than thermal origin. Similarly, MD simulations on different metallic glasses suggest that the thermal effect becomes important only after the STZ reaches a critical size.[113]

During release (unloading), the STZs can still persist, although the exact deformation may vary with time and impact velocity; Figure 3.11 shows STZs at a completely released state. Shear bands were well observed in a Zr-based metallic glass recovered after shock loading.[124] Following unloading, the glass is subjected to tensile loading, and the configuration near the onset of spallation (prespall, cf. Figure 3.3) undergoes additional shear strain compared to their earlier shock state counterparts. For example, the average η^{vM} is about 0.12 at the shock state for u_p =0.5 km s^{-1}, and it increases to about 0.18 right before spall after release fan induced tensile loading beyond compression.

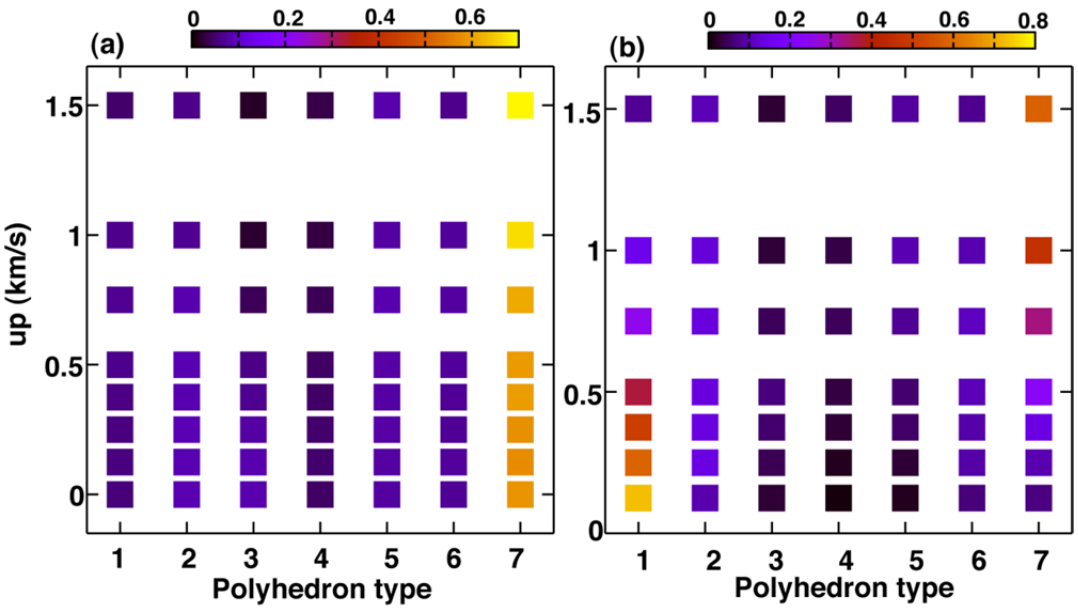

Figure 3.12 (a) The atomic fraction vs Voronoi polyhedron type at different shock states and ambient conditions. Each atom belongs to a certain Voronoi Types (1–7) based on the Voronoi analysis. (b) The fractions of the original Type 1 atoms transforming into other types at different shock states (transformed). The fraction of Type 1 atoms in the unshocked state is 1. The conserved fraction is also included (atoms remaining as Type 1 after shock loading).

The prespall η^{vM} is about 0.2 if referenced to the shock state. STZs also grow in size (Figure 3.8 vs Figure 3.9) over the course of shock compression, release and tension, and can be better correlated with local temperature before spall (compared to the correlation at the shock state), likely because of the longer time scales allowing heating from shear strain (plastic heating). We have shown that void nucleation in shock-loaded single crystal Cu is preceded by crystal plasticity and other defect formation, and occurs preferentially at the regions with high disordering and plasticity. (Similar behavior is observed for Ni under shock and Lennard-Jones face-centered cubic crystals and single crystal Cu under nonshock conditions).[92,94,135] Preferential nucleation of voids in disordered regions was observed in a shock-loaded crystalline glass-forming crystalline (B11) CuTi alloy.[136] Void nucleation is found to favor shear bands in shock-recovered crystalline alloys[33] and bulk metallic glass.[124] As expected, the snapshots in Figure 3.8 show that void nucleation occurs at highly shear-deformed regions (high plasticity) in the amorphous metallic glass. Thus, the predamage in terms of plasticity as well as certain defect formation is prerequisite and likely common for void nucleation in both crystalline and amorphous metals.

3.5 Structural Features Related to Plasticity and Spall

The microscopic structures of the unshocked and shocked $Cu_{46}Zr_{54}$ glasses are characterized with the Voronoi analysis method, in which each atom is indexed with four Voronoi indices and assigned a Voronoi polyhedron type. As described in Section 3.2, Types 1–6 are individual Voronoi types, and Type 7 is a collective Voronoi type consisting of numerous other minor individual types such as <0,2,8,3>, <0,4,4,3>, <1,0,9,3>, and <0,12,2,0>. Shown as an example in Figure 3.10(a) inset is a Type 1 Cu atom (indexed as <0,0,12,0>) with its 12 Cu and Zr nearest neighbors forming an icosahedron around it. The fractions or percentages of Voronoi Types 1–7 are calculated referencing to the total number of atoms in a region under consideration, and shown in Figure 3.12(a) for the ambient and shock states at different u_p.

In the unshocked glass (u_p = 0), the atoms indexed as Types 1–6 are predominant in quantity over all other individual types included in Type 7. The fraction of Type 1 atoms (icosahedron) is about 0.05; among all the Type 1 polyhedra, the majority is Cu centered and the Zr-centered polyhedra account for ~ 9%, consistent with previous studies.[112,127,137] The fraction of Type 3 atoms is about 0.09, and most Type 3 polyhedra are also Cu-centered. <0,12,2,0> is an example of Type 7; all polyhedra indexed as <0,12,2,0> are Zr-centered and likely related to the Frank-Kasper polytetrahedra.[138] As a collective type, however, the fraction of Type 7 atoms (>0.5) prevails over Types 1–6 in unshocked and shocked states. Types 1–6 represent relatively "close-packed" atoms, and are expected to diminish with increasing shock strengths overall. With increasing u_p, the fractions of Types 2–4 decrease, that of Type 1 increases slightly and then decreases rapidly, and those of Types 5 and 6 remain nearly constant, while that of Type 7 increases from about 0.6 at u_p = 0 to 0.7 at 1.5 km s^{-1}. The decrease in Type 3 contributes to about 70% of the increase in Type 7 over the whole u_p range explored. Above HEL, the atoms of Type 3 decrease rapidly within u_p = 0.25 – 1.0 km s^{-1} and, Types 2 and 4, within 0.5 – 1.0 km s^{-1}, consistent with the pronounced softening above 0.375 km s^{-1} (Figure 3.7).

Upon shock loading, the Voronoi type of an atom can change, e.g., the original Type 1 may transform *into* another type (Types 2–7) after shock, and a Type 1 atom at the shock state may have transformed *from* another type. For illustrative purpose, we characterize such transformations between Type 1 and other types at different steady shock states. Figure 3.12 (b) shows the case of transformation from Type 1 into Types 1–7. With increasing u_p, the conserved fraction (Types 1→1, or simply 1→1) decreases rapidly from about 0.73 at u_p = 0.125 km s^{-1} to 0.08 at 1.5 km s^{-1}; the conserved Type 1 atoms are highly shear resistant (see below) and their decrease is consistent with the strain softening (Figure 3.7). The fractions of the original Type 1 atoms transforming into Types 3 and 4 are largely negligible. The 1→7 transformation is the most pronounced overall in particular at the high u_p end, followed by the 1→2, 1→6 and 1→5 transformations in descending order. The 1→2 transformation is favored at the low u_p

end, and 1→5, the high u_p end. For the transformations into Type 1 at the shock states (not shown), the general feature is mainly similar to their inverse transformations [Figure 3.12(a)] except for a more pronounced 3→1 transformation (compared to its inverse) above HEL. The frequent occurrence of the 1↔2 transformations (only less frequent than 1↔7) may be explained by their structural similarity. As a result of the forward and backward transformations, the fraction of Type 1 atoms undergoes a minor increase and then faster decrease with increasing u_p. As noted previously,[112] such transformations as 1→5 induce excess volumes, which may lend some support to the free volume model of plasticity in metallic glasses.[4,5,134]

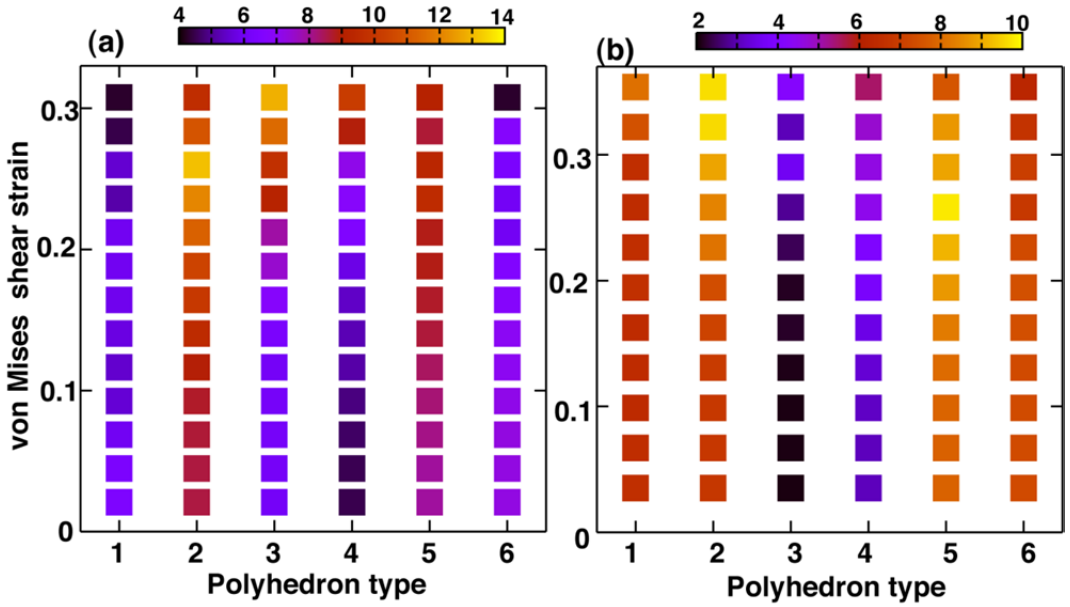

Figure 3.13 The percentage of a specific Voronoi type vs. shear strain at the shock states with (a) u_p = 0.5 km s^{-1} and (b)1 km s^{-1}. Color coding is based on the cumulative percentage above a certain η^{vM}.

Given the Voronoi analysis at different shock states, we characterize the shear mobility (m) of a Voronoi atom type in terms of η^{vM} at different shock strengths (Figure 3.10). For each original (before shock) Voronoi type (Types 1–6), we divide the

corresponding atoms within a selected steady shock region into two groups, the conserved and transformed atoms; the average shear strain is calculated for each group, and compared to the bulk average of all the atoms under consideration, which serves as the baseline for comparison. Overall, the conserved atoms undergo smaller shear strain than the transformed atoms, and the difference is diminished at the high u_p end. For the transformed atoms, $m_1 \approx m_6 \approx m_5 < m_2 < m_4 < m_3$ (subscripts denote the Voronoi types); for the conserved atoms, $m_1 < m_6 < m_2 < m_5 \approx m_4 \approx m_3$. The difference in the shear mobility between conserved and transformed atoms is the largest for Type 1 and smallest for Type 5; and the average mobility for a given type (including both conserved and transformed) is the highest for Type 3 and smallest for Type 1. Thus, Type 3 atoms are most mobile (Type 4 is similar but less important due to its low concentration); Type 1 atoms are most shear-resistant, similar to previous observations.[112,127] Type 5 atoms are most likely to follow the bulk behaviors. Type 6 is similar to Type 1 in the general trend. The high shear mobility of Type 3 atoms also dictates their low structural stability under shear stress; as shown in Figure 3.12(a), the fraction of Type 3 decreases continuously to nearly zero with increasing u_p. The major increase in the shear strain occurs at u_p = 0.5–1.0 km s^{-1} for Types 1–6 (Figure 3.10), which partly reduces the fractions of such types as Type 3 [Figure 3.12(a)]. Note that the shear strain of the conserved Type 1 atoms is constant below and near HEL and then increases rapidly above HEL; thus, one manifestation of the plasticity is the sharp increase in the shear mobility of conserved Type 1 atoms.

We also examine the distributions of Types 1–7 in the whole range of η^{vM} within a steady shock region. This η^{vM} range is divided into 20 bins, each centered at certain η^{vM}; and the number of atoms of each type within each bin is counted. The cumulative number of atoms above a certain η^{vM} is obtained as well. The corresponding percentages are calculated, and Figure 3.13 shows the examples of such distributions at two representative shock states, u_p = 0.5 and 1.0 km s^{-1} (only the cumulative distributions are shown).

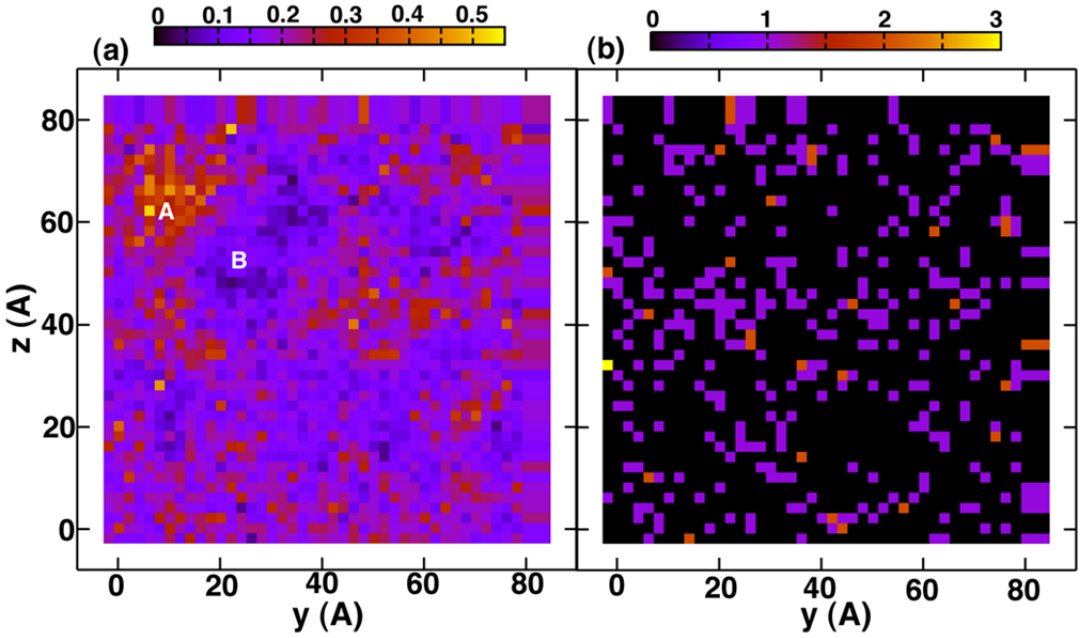

Figure 3.14. The prespall η^{vM} distribution (a) and the corresponding distribution of Type 1 and 6 atoms in a thin section for $u_p = 0.5$ km s^{-1} at 87.2 ps, viewed along the shock direction. In (a), *A* denotes a high η^{vM} region (void nucleation site), and *B*, a low η^{vM} region. In (b), color coding refers to the number of Type 1 or 6 atoms in a fine grid on the *yz* plane.

At u_p = 0.5 km s^{-1} [Figure 3.13(a)], the percentages of Types 1 and 6 decrease with increasing η^{vM} (favoring low η^{vM} as observed previously),[130] in sharp contrast to Types 2–5 (favoring high η^{vM}); these observations are consistent with their shear mobilities (or resistances). In particular, Type 1 is most abundant at the lowest shear strains, and Type 3, the highest strains (excluding Type 7). Thus, the high shear mobility of Type 3 (as well as Types 2, 4, and 5 to a lesser extent) atoms play the dominant role in the formation of STZs, and Type 1 (as well as Type 6) atoms, in forming lower strain regions distinct from STZs. The distribution of Type 7 is approximately uniform (minor decrease in the fraction with increasing η^{vM}). All these types act collectively to induce the inhomogeneous shear deformation at the atomic level that leads to plastic flow. At u_p =1.0 km s^{-1} [Figure 3.13(b)], the general trend remains similar with some exceptions. Types 1 and 6 are enriched relative to Types 2–5, and Types 2 and 5 become most

abundant at highest η^{vM}. The drastic changes lie in Type 3, which is almost absent at the low η^{vM} end and reduced greatly at the high end, simply because of its low stability at high shock strengths due to its high shear mobility. The total fraction of Type 3 is reduced [Figure 3.12(a)] again due to its low structural stability.

Similar to the plasticity nucleation and shock state strain softening as discussed above, the transient hardening [Figure 3.5(b)] can also be attributed to the atomic-level structural evolution. At the onset of plasticity (just above HEL), we find that the fraction of Type 3 atoms decreases while 2τ increases transiently, and thus the nucleation sites are reduced since Type 3 atoms play a predominant role in STZ nucleation. As argued by Chen,[134] the critical shear stress driving the formation of STZ will increase in order to sustain a plastic deformation rate as the nucleation sites exhaust, thus giving rise to the transient strain hardening. Indeed, we observe that such hardening increases with increasing loading rate (or u_p).

During release and tension induced by the reflected shock waves, the solid undergoes further shear deformation and structure changes, and nanovoids nucleate in the regions with high shear deformations [Figures 3.8 and 3.14(a)]. As an illustrative case relating void nucleation to local structures for low and medium u_p (the shock regime of main interest), we cut a thin slice out of the prespall atomic configuration perpendicular to the shock direction through the void nucleation region for u_p = 0.5 km s^{-1}; the Voronoi type and η^{vM} for each atom within this slice are calculated prior to slicing. The highest η^{vM} (>0.3) region is dominated by the atoms of Type 2–5 (in particular Type 3; excluding Type 7), where Type 1 and 6 atoms are minimum [similar to Figure 3.13(a)]. In the spatial distributions of η^{vM} and the Voronoi types, region *A* is occupied by atoms with the highest shear deformation [Figure 3.14(a)] while few Type 1 or 6 atoms are present [Figure 3.14(b)]. On the other hand, Types 1 and 6 are much more abundant in the least shear-deformed regions (e.g., $\eta^{\mathrm{vM}} < 0.05$, region *B*). Thus, the regions with prone-to-shear-flow Type 3 atoms are also favored for void nucleation, in sharp contrast to Type 1 atoms with highest shear resistance. However, we do not expect an exact one-to-one spatial correspondence between a local structure and the shear

deformation in the whole region. Note that these structural features related to void nucleation are only approximate since the glass is more homogenized after release and tension compared to the shock state. At high shock strengths, fewer Type 3 atoms are found for the same reason of high shear mobility as in the shock state; void nucleation still occurs at the highly shear-deformed regions during tension, but the exact structural features vary because of different shock state structures and subsequent relaxation during release and tension.

The complex structural changes among different Voronoi polyhedron types are observed in our simulations, and the formation and evolution of STZs are accompanied by these changes in a dynamic way. Possible mechanisms underlying such changes include the free volume theory and the bond-exchange model;[139,140] the latter was proposed by Egami and co-workers to describe the shear deformation in glasses. On one hand, the free volume theory is appealing since free volume is necessary for local shear transformation,[140] and such transformations as Types 1→5 induce excess volumes.[112] On the other hand, the atomic bond rearrangement is more realistic as suggested by Egami.[140] Egami argued that deformation should involve changes in bond arrangement if the structure is defined by the topology of atomic connectivity, and proceeds via bond exchange when the total number of bonds is conserved during rearrangement. A recent MD simulations on a binary metallic glass show that transitions between distinct polyhedron types may occur at ps time scale and give rise to the boson peak.[141] The structure changes in our simulations could be candidates for such topological structure changes, and thus the bond rearrangement appears to be a highly plausible mechanism. Guerdane and Teichler[141] also pointed out that in icosahedral-like medium range orders, the coupling between neighboring structural units leads to dependencies between their local environment transitions and induces an atom exchange between them, in a way similar to the bond-exchange model; this argument lends further support to the bond-rearrangement mechanism.

CHAPTER IV

DISLOCATION INDUCED SHEAR BANDING IN METALLIC GLASS WITHIN $Cu/Cu_{46}Zr_{54}$ GLASS NANOLAMINATES

4.1 Introduction

Shear band related deformation is a dominant factor for cracking and failure in metallic glasses.[5,9] Shear transformation zones (STZs) are the plasticity carriers in metallic glasses in the absence of dislocations, and have been observed for different loading conditions including shock wave loading.[5,124,142] STZs may form shear bands but the exact processes are not completely understood. Several molecular dynamics (MD) studies observed SB formation by introducing notches to initiate shear bands, indentation, pure shearing or simulated casting, as well as uniaxial compression.[103,130,143-148] Especially, the role of short-range order (SRO) in SB formation and softening of metallic glasses was emphasized.[130]

Recent experiments demonstrated exceptional ductility of nanocrystalline-amorphous nanolaminates, and MD simulations and electron microscopy pointed to the role of amorphous−crystalline interfaces (ACIs) both as sources and sinks of dislocations.[3,81,149] ACIs show a potential for engineering novel materials and revealing new phenomena and underlying physics. However, some key questions do remain, including whether shear bands form in a metallic glass layer of crystalline−glass nanolaminates under the similar loading conditions where shear bands form in the corresponding bulk glass, and what are the mechanisms of shear banding if it occurs. Further understanding of shear band formation can help engineer metallic glasses with desired functionalities.[5] Experimental or MD studies are still rare in this emerging field.[3,81,150] Here we report MD simulations of $Cu(111)/Cu_{46}Zr_{54}$ glass nanolaminates, and show that shear bands in the glass can be directly induced by dislocations in the Cu layers through ACIs.

4.2 Model Preparation and Visualization of Dislocations

Our MD simulations are performed with the LAMMPS package[100] and an embedded-atom-method potential for the Cu-Zr system.[111] The initial $Cu_{46}Zr_{54}$ configuration, composed of 16000 atoms ($4.8 \times 17 \times 3.6$ nm^3 in edge lengths) with randomized Cu or Zr positions, is subjected to incremental heating to 2000 K (melted) with the constant-pressure-temperature ensemble and three-dimensional (3D) periodic boundary conditions. The time step for integrating the equation of motion is 2 fs. The liquid alloy is then cooled down to 50 K at a cooling rate of 0.01 K/ps. It is important to use a proper cooling rate since it has a direct effect on the SRO characteristics and consequently on shear band formation. We thus adopt the same cooling rate as reported in previous simulations.[111,151] (We also test much higher cooling rates and observe homogeneous deformation instead of highly localized shear bands in pure glass, consistent with a previous study.[128] The total time for heating, melting and cooling is approximately 195 ns. This unit glass configuration is then replicated by $2 \times 2 \times 20$ (1280000 atoms), annealed at 800 K for 2 ns, and then cooled down to 50 K at 1 K/ps ($9.7 \times 34 \times 71$ nm^3). The resultant glass is used for simulations of pure glass and nanolaminates. To construct a $Cu/Cu_{46}Zr_{54}$ glass bilayer, a Cu (111) slab of similar dimensions ($9.5 \times 34 \times 71$ nm^3) is equilibrated at 50 K and zero pressure and combined with the glass; the bilayer (3054080 atoms) is further equilibrated under 3D periodic conditions for about 0.5 ns. We also construct another bilayer structure with the same cross-section but half the thickness (~ 5 nm for each layer) for simulations at the same conditions. Discussions refer to the thicker bilayer structure (~ 10 nm per layer) unless otherwise stated.

There are various methods used for visualizing the dislocations such as common neighbor analysis,[152,153] cohesive energy,[154] centrosymmetry,[155] coordination number (CN),[156] slip vector analysis[157] and some other techniques. Figure 4.1 shows six different methods of visualization of a dislocation in a nanocrystal.[158] In the present work, the centrosymmetry and the slip vector analysis (maximum relative displacement) are used.

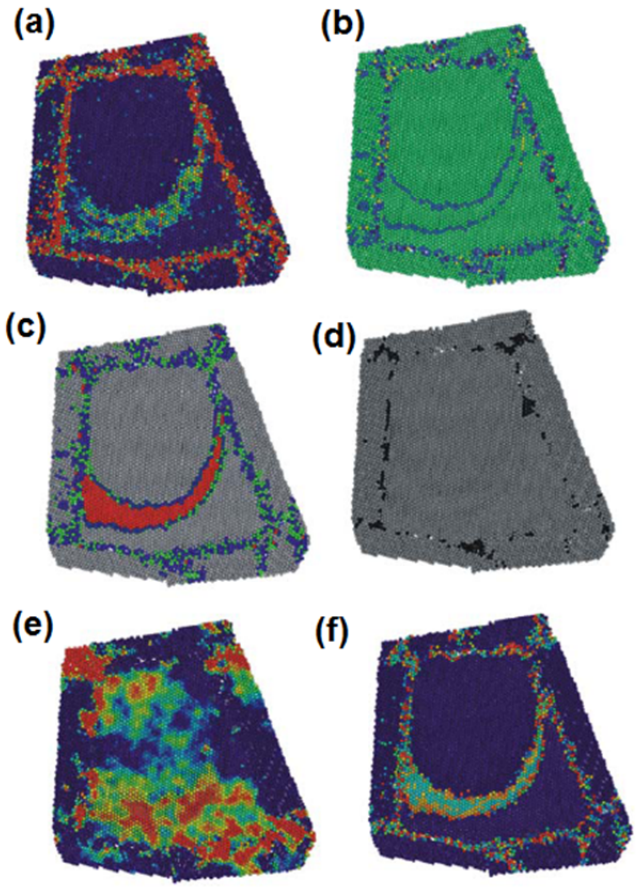

Figure 4.1 Visualization of a dislocation segment by six different methods in a nanocrystal. Coloring is based on (a) potential energy, (b) coordination, (c) medium range order, (d) position disorder, (e) hydrostatic pressure and (f) centro-symmetric parameter. Image taken from Ref.[158]

Centrosymmetry is a very useful method to reveal whether an atom is part of a perfect lattice or a defect such as stacking fault, dislocation, grain boundary and free surface. The centrosymmetry parameter (CP) is calculated for each atom by;[155]

$$CP = \sum_{i=1}^{N/2} \left| \vec{R}_i + \vec{R}_{i+N/2} \right|^2 \qquad (4\text{-}1)$$

where $\vec{R}_i + \vec{R}_{i+N/2}$ are the bond length vectors and N is the number of nearest neighbors of the central atom. For example, for an fcc crystal, N = 12, thus there are 6 bond pairs

which are added together and their squares are summed to calculate the CP value for a central atom. If this atom is on a perfect lattice site, its CP value should be 0 (or close to 0 due to thermal perturbations). In the case of a defect, the symmetry is broken and the value of the parameter becomes larger than 0. Table 4.1 shows the centrosymmetry value range for a typical FCC atom (gold).

Table 4.1 Centrosymmetry (real and normalized) values for gold (FCC).[100]

Defect	$\boldsymbol{CP}$	$\boldsymbol{CP/a_0^2}$
Bulk Lattice	0	0
Dislocation core	0.5 - 1.25	0.03 - 0.075
Stacking faults	4.0 - 6.0	0.24 - 0.36
Free surface	23.0	1.38

4.3 Results and Discussion

In uniaxial stress (σ) loading of the bilayer structure and pure glass, we apply periodic boundary conditions only along the *x*- and *z*-axes, resulting in two free surfaces along the *y*-axis. The nanostructure thus contains repeating bilayers along the *x*-axis (nanolaminates). Uniaxial compression is applied along the *z*-axis via scaling the corresponding cell length. The boundaries along the *x*-axis are coupled to a barostat to maintain σ_{xx} = 0. The strain (ε) rate in our simulations is 4×10^7 s^{-1}. The loading procedure is the same as or similar to previous simulations.[151,159]

Uniaxial compression loading is applied to the nanolaminates and pure glass up to $\varepsilon \sim 10\%$, followed by unloading to zero stress at the same strain rate; their $\sigma_{zz} - \varepsilon$ curves are markedly different [Figure 4.2(b)]. The small initial stress ($\sigma_{zz} \sim 0.3$ GPa) in the nanolaminates is due to different relaxation in the Cu and glass layers when the free surfaces normal to the y-axis are imposed. The nanolaminates deform elastically or with little plasticity (OA) until σ_{zz} peaks at 4.3 GPa ($\varepsilon = 4.7\%$). The ensuing plastic deforma-

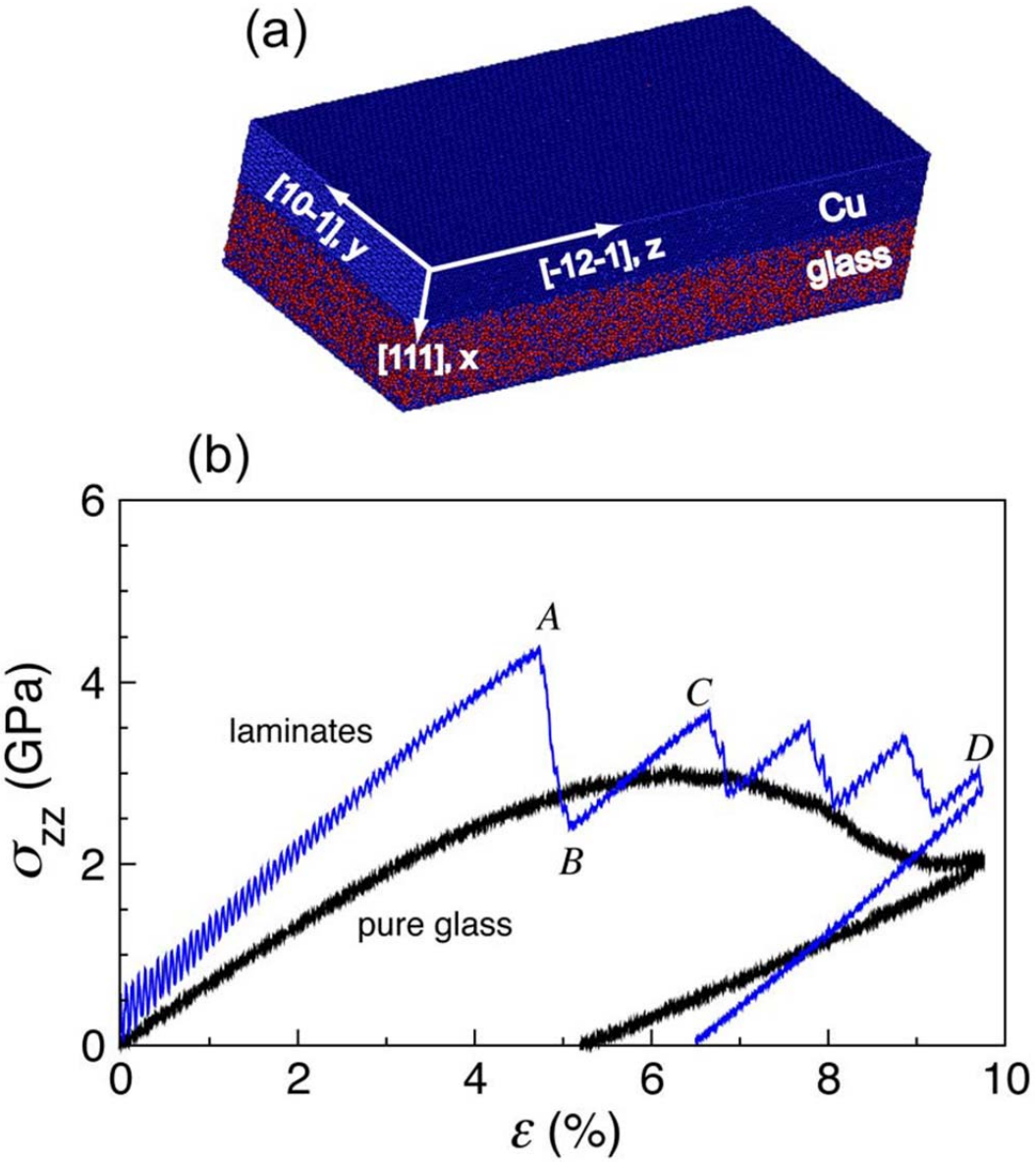

Figure 4.2 (a) Configuration of the Cu-$Cu_{46}Zr_{54}$ glass nanolaminates. The laminate width is defined along the y-axis. (b) $\sigma_{zz} - \varepsilon$ curves for nanolaminates and pure glass.

tion shows a zig-zag pattern, indicating cyclic strain softening (AB) and hardening (BC). σ_{zz} fluctuates around 3 GPa, and the fluctuations decay with increasing loading. In contrast, the pure glass is softer in the "elastic" regime, and the loading curve peaks at lower stress (3 GPa) but higher train (6.5%). The stress relaxation is smooth without

apparent strain hardening, and becomes stabilized around 2 GPa. The unloading curves are smooth for both cases. The unloading slope is steeper for the nanolaminates, and the residual strain after unloading (6.4%) is higher than pure glass (5%). We characterize the atomic-level structure and deformation with the commonly used parameters, the atomic von Mises shear strain[113,129] (η^{vM}) and centrosymmetry parameter.[155] The atomic-level deformation can also be characterized with the slip vector[157]

$$\boldsymbol{s}_i = -\frac{1}{n_s}\sum_{i\neq j}^{n}\left(\mathbf{x}_{ij} - \mathbf{X}_{ij}\right). \tag{4-2}$$

Here n is the number of the nearest neighbors to atom i, n_s is the number of the slipped neighbors j, and $\boldsymbol{x}_{ij}$ and $\boldsymbol{X}_{ij}$ denote the vector (between atom i and j) difference in current and reference configurations, respectively. The reference configurations are the pre-load structures. Similarly, the maximum relative displacement is defined as[160]

$$s_i = \mathbf{x}_{ij} - \mathbf{X}_{ij}: \quad \left|\mathbf{x}_{ij} - \mathbf{X}_{ij}\right|_{max}. \tag{4-3}$$

The latter definition is used in our analysis, and the scalar slip is $s_i = |\mathbf{s}_i|$. Although the centrosymmetry method allows differentiating between the different defects (stacking fault, full dislocation, twin dislocation, etc.), it lacks the information regarding to the Burgers vector of dislocations. Slip vector approach, on the other hand, supplies the information about the Burgers vector. Another advantage of slip vector method is that it can be applied to any microstructure, whereas the centrosymmetry approach can only be utilized for the centrosymmetric microstructures. The results are shown in Figure 4.3 for the nanostructure and pure glass at different stages of loading and unloading.

In the face-centered cubic structure, an edge dislocation is dissociated into a leading and a trailing Shockley partial linked by a stacking fault. The amplitude of the Burger's vector is $|\mathbf{b}|$ =1.48 Å for a {111} <112> Shockley partial dislocation, and 2.56 Å for a perfect {111} <110> dislocation in Cu. In our simulations, the dissociated dislo-

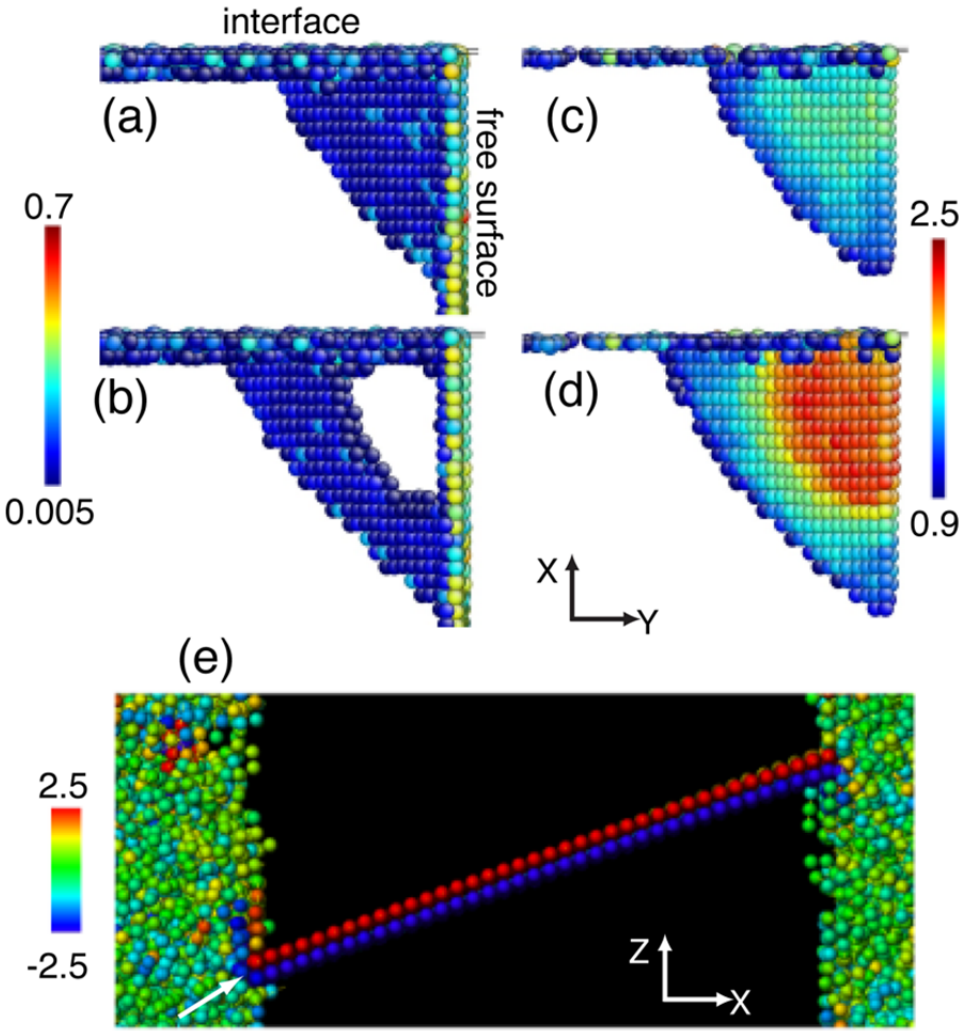

Figure 4.3 Snapshots of partial, full and screw dislocations in the Cu layer of the bilayer structure. (a) and (b) are visualized with the centrosymmetry parameter, and their counterparts color-coded with MRD amplitude in Å are shown in (c) and (d), respectively. (e) is visualized with MRD amplitude and shifted along the x-axis; it shows a section farther away from the free surfaces. ε = 4.4 % for (a) and (c); ε = 4.404 % for (b) and (d); ε = 4.7 % for (e).

cation propagates through the Cu layer predominantly with an edge dislocation character accompanied by screw dislocation n content into the ACI. Deposition of the screw dislocation causes local shear deformation in the vicinity of the ACI similar to the full Burger's vector of the dislocation. This process can be envisioned as dislocation cross-slip into the ACI plane. Figure 4.3 shows sequentially the dislocation activities in the Cu layer. At the onset of plasticity [AB in Figure 4.2(b)], a leading partial dislocation is

nucleated at the corner of an ACI and a free surface [Figures 4.3(a) and 4.3 (c)]; subsequently the trailing partial dislocation is nucleated at the same location [Figures 4.3(b) and 4,3(d)]. (Similarly, dislocation nucleation near the free surface was observed for nanowires or thin films.[161-163] While the centrosymmetry parameter visualization [Figures 4.3(a) and 4.3(b)] is consistent with its MRD counterpart [Figures 4.3(c) and 4.3(d)], the latter appears better in revealing dislocation features. The dissociated full dislocation loop propagates on the same habit slip plane towards the opposite ACI. The dislocation also propagates towards the opposite free surface. While encountering the opposite interface, the full dislocation switches its slip plane from one {111} to another {111} parallel to the ACI as indicated by the arrow in Figure 4.3(e), forming a screw dislocation. [Figure 4.3(e) shows the projection of MRD onto the slip direction. Two neighboring parallel {111} planes move in opposite directions]. Upon impinging on the opposite free surface, the dislocation induces stress or strain concentration near the free surface, which then leads to the activation of parallel or intersecting slip planes (not necessarily simultaneously) that propagate back toward another free surface. This process is repeated during the loading process and yields the slip pattern or "slip bands" as illustrated in Figure 4.4(b). Shear deformation is more pronounced (in terms of η^{vM} amplitude and "band" width) where adjacent parallel slip planes are activated. Steps or ledges are also formed on the free surfaces as a result of the interaction between dislocations and free surfaces.

Plasticity in the glass layer of the bilayer structure is revealed with η^{vM}, and manifested as STZs or larger-scale shear bands; nucleation and growth of plasticity in the glass layer predominantly follow the dislocation−ACI interactions [Figures 4.4(b), 4.4(c) and 4.4]. When the first dislocation is nucleated in the Cu layer, only randomly dispersed STZs appear within the glass layer [Figure 4.5(a)]. As the propagating dislocation impinges on or moves along ACIs, STZs in the glass layer are nucleated at the interfaces by virtue of the dislocation strain field; the moving dislocation creates two narrow shear bands (connected STZs) along the opposing ACIs, which then grow toward

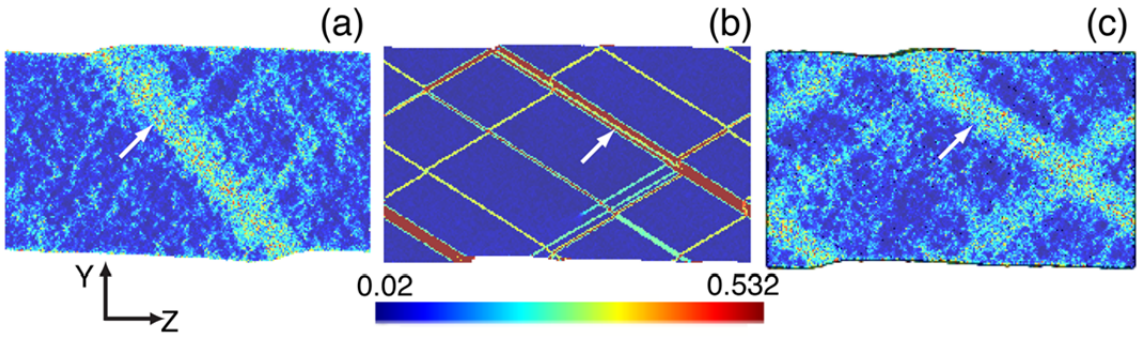

Figure 4.4 Shear deformation η^{vM} map of pure glass (a), and the Cu layer (b) and glass layer (c) in the nanostructure (viewed along the interface normal).

the interior of the glass layer [Figures 4.5(b) and 4.5(c)]. During its growth, a shear band may absorb "background" STZs in the glass layer [Figure 4.5(c)]. (Shear bands are not symmetric with respect to the dislocation since it impinges on the ACI at about 70°.) This process of shear band nucleation and growth is repeated, and continues along with the dislocation-mediated plasticity in the Cu layer as discussed above. Figure 4.4(c) suggests that shear banding is the main mechanism of plasticity in the glass layer, complemented by scattered STZs. The shear band pattern in the glass layer matches the dislocation pattern in the Cu layer, and so do the free surface ledge locations. The width of shear bands and η^{vM} amplitude within the glass layer are proportional to those of the "slip bands" in the Cu layer [Figures 4.4(b) and (c)]. Thus, shear banding in the glass layer is a direct result of dislocation activity in the Cu layer. Previous MD simulations used a different loading scheme and showed the formation of STZs (not shear bands) induced by dislocations.[3]

For pure glass under increasing ε, small shear bands (preceded by STZs) form at random locations near free surfaces; one of them becomes dominant and grows toward the opposite free surface, and plasticity concentrates on this main shear band along with "secondary shear bands" and STZs [Figure 4.4(a)]. Shear banding also induces ledges on the free surfaces. (Details of shear band formation were reported in a similar simulation.[151] The primary shear band is at $\sim 45^{\circ}$ with the loading axis (z), following the

maximum shear stress direction. In sharp contrast, multiple intersecting shear bands form in the glass layer of the bilayer structure, and are at ~ 30^{o} with the loading axis (e.g., the arrows in Figure 4.4). The differences in plastic deformation between pure glass and the glass layer in the nanolaminates further support that dislocations in the Cu layer induce shear banding in the glass layer in the nanolaminates.

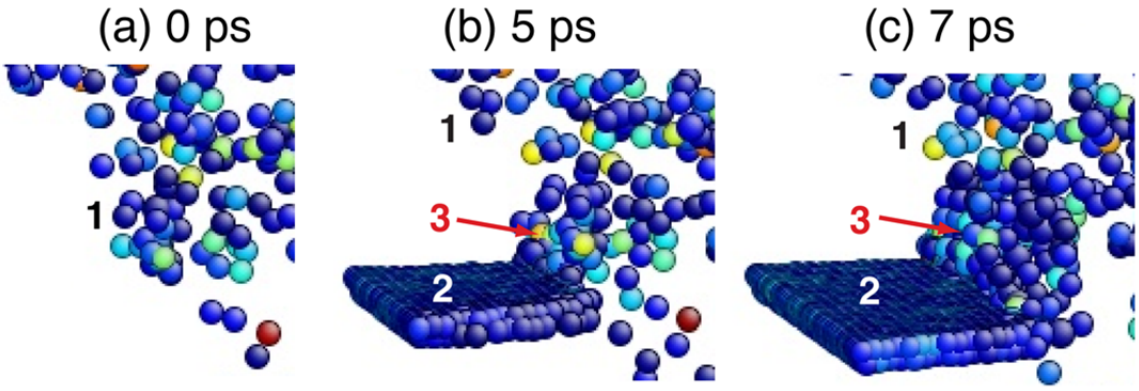

Figure 4.5 Snapshots of shear band nucleation-growth in the glass layer (relative time) visualized with η^{vM}. 1: STZs; 2: advancing dislocation; 3: growing shear band.

In the nanolaminates, dislocation nucleation and propagation are frustrated by the free surfaces until sufficient shear stress is rebuilt for the next round of dislocation activity. Such "periodic" dislocation activity in the Cu layer causes the cyclic strain softening and hardening [Figure 4.2(b)], while shear banding in the glass layer contribute to softening to a lesser extent. Upon unloading, dislocations in the Cu layer and shear bands in the glass layer are largely preserved, indicating their stability in the MD time scales. Simulations on the thinner bilayer structure (~ 5 nm) yield similar features. Shear banding is expected to form for thicker glass layers; as an extreme case, shear bands are observed in bulk metallic glasses in current and previous studies.[151]

A previous simulation without free surfaces showed that ACIs act as both dislocation sources and sinks under tensile loading and induce STZs.[3] Our simulations

(uniaxial compression with free surfaces) demonstrate definitively that stable shear bands in a thin glass layer (5−10 nm thick) can be induced by dislocations, indicating that shear banding is sensitive to loading (e.g., compression vs tension, and the existence of free surfaces). In our simulations, the first dislocation is nucleated at the intersection of an ACI and a free surface, and free surfaces rather than ACIs are primarily the source for subsequent dislocations. ACIs are sinks of dislocations as well as barriers, and do interact with dislocations (including interface-induced screw dislocations), so the strain energy is transferred to the glass layer through ACIs and shear bands may be induced as a result. The growth of shear bands also incorporates absorbing the independent, "ambient" STZs in the glass layer.

CHAPTER V

DYNAMIC RESPONSE OF PHENOLIC RESIN AND ITS CARBON-NANOTUBE COMPOSITES TO SHOCK WAVE LOADING

5.1 Introduction

Polymers and polymer-based composites have long been explored/exploited for a wide range of engineering applications including high strain rate loading (e.g., shock waves).[164-177,191-192] Especially, for aerospace applications, composite properties require high strength, superb thermal properties and comparatively light weight.[173] Furthermore, since the space ships expose to shock loadings during the re-entry to the atmosphere, having high shock resistance coatings becomes highly important. A number of experimental and numerical studies investigate the potential use of carbon nanotube or fiber reinforced composite coatings for aerospace operations.[178-181]

Despite extensive shock experiments on these materials,[164-165,169-171,176-177,182-183,191] the underlying deformation and "phase change" mechanisms have been elusive due to the daunting complexities inherent in polymeric materials. While the challenge remains and numerical simulations of such materials are computationally intractable and expensive, reactive and nonreactive molecular dynamics (MD), coarse-grain dynamics and first-principles-based modelling/simulations are advantageous in revealing the microscopic details.[166-169,172-175]

Direct MD shock simulations of polymers and polymer composites are rare; some previous MD simulations explored the shock response of molecular crystals and chemistry.[184] As a first attempt on direct MD simulations of shock response of polymer and polymer composites, we choose phenolic resin and its carbon-nanotube (CNT) com-

---

[*]Part of this chapter is reprinted with permission from "Dynamic response of phenolic resin and its carbon-nanotube composites to shock wave loading" by B. Arman, Q. An, S. N. Luo, T.G. Desai, D. L. Tonks, T. Cagin and W. A. Goddard III, 2011, *Journal of Applied Physics*, **109**, 013503. Copyright 2011 by AIP Publishing.

posite in current study [Figures 5.1(a) and 5.2]. CNTs are highly desirable as a structural component in the composites for their superior mechanical and physical properties.[166-168,185] For instance, a recent MD work explored the shock response of the CNT-SiC composites modeled with the Tersoff potential.[173] Our shock simulations yield the Hugoniots of phenolic resin and its CNT composites, and reveal the mechanisms for plasticity and the anisotropy in the shock response of the composites with regularly ordered CNTs.

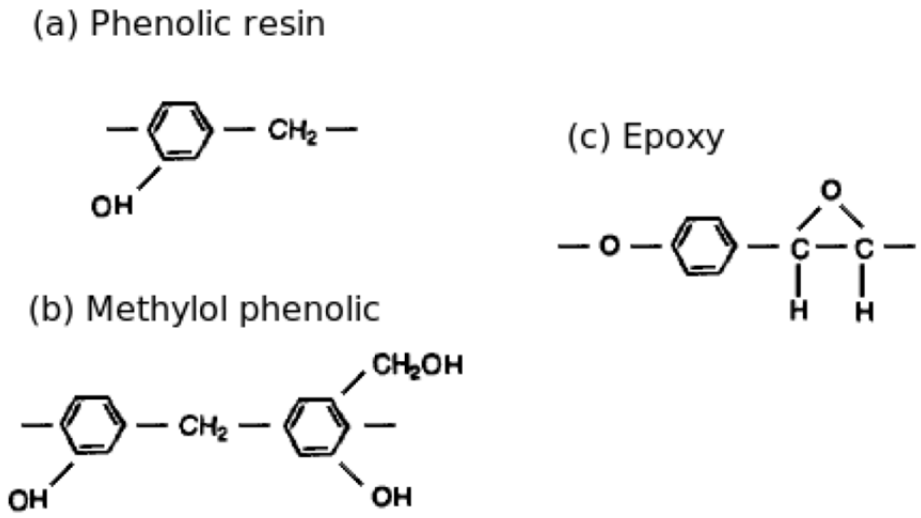

Figure 5.1 Monomers of phenolic resin, methylol phenolic and epoxy.

5.2 Sample Preparation

The forcefield or interatomic potential describing the interactions in phenolic resin, CNT and their composites, is *ab initio*-based polymer consistent force field (PCFF).[186] PCFF includes valence terms [bond (1), angle (2), torsion angle (3), out-of-plane angle (4) and cross-coupling (5) terms in equation (5.1)] and nonbond interaction terms.

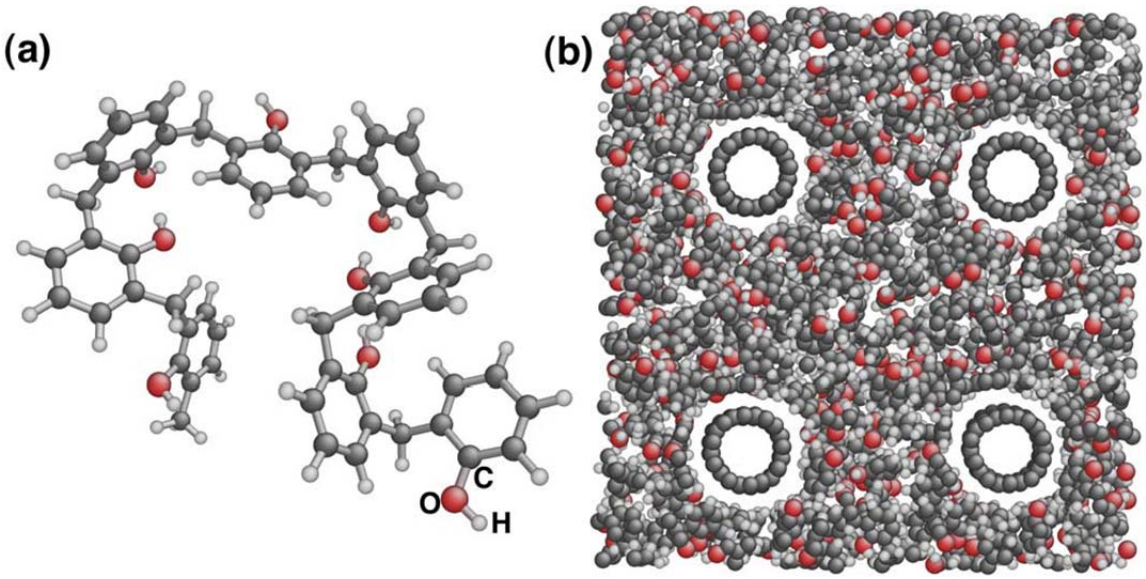

Figure 5.2 (a) A single polymeric chain of phenolic resin. (b) A cross-section of a CNT-resin composite (~5.8 nm×5.9 nm).

$$E_{\text{total}} = \sum_{b}[k_2(b-b_0)^2 + k_3(b-b_0)^3 + k_4(b-b_0)^4] +$$

(1)

$$\sum_{\theta}[k_2(\theta-\theta_0)^2 + k_3(\theta-\theta_0)^3 + k_4(\theta-\theta_0)^4] +$$

(2)

$$\sum_{\emptyset}[k_1(1-\cos\emptyset) + k_2(1-\cos 2\emptyset) + k_3(1-\cos 3\emptyset)] +$$

(3)

$$\sum_{\chi} k_2\chi^2 + \sum_{b,b'} k(b-b_0)(b'-b_0') +$$

(4)

$$\sum_{b,\theta} k(b-b_0)(\theta-\theta_0) + \sum_{b,\phi}(b-b_0)[k_1\cos\emptyset + k_2\cos 2\emptyset + k_3\cos 3\emptyset] +$$

(5)

$$\sum_{\theta,\phi}(\theta-\theta_0)[k_1\cos\emptyset+k_2\cos 2\emptyset+k_3\cos 3\emptyset]+\sum_{b,\theta}k(\theta'-\theta_0')(\theta-\theta_0)+$$

$$\sum_{\theta,\theta,\phi}k(\theta-\theta_0)(\theta'-\theta_0')cos\,\emptyset+\sum_{i,j}\frac{q_iq_j}{r_{ij}}+\sum_{i,j}\epsilon_{ij}\left[2\left(\frac{r_{ij}^0}{r_{ij}}\right)^9-3\left(\frac{r_{ij}^0}{r_{ij}}\right)^6\right] \qquad (5\text{-}1)$$

(6) (7)

The nonbond interaction terms account for electrostatic and van der Waals interactions [terms (6) and (7) in equation (5-1)]. Van der Waals interaction include a LJ-9-6 function, whose parameters for unlike atoms are given as[186]

$$r_{i,j}^0=\left(\frac{(r_i^0)^6+(r_j^0)^6}{2}\right)^{1/6} \qquad (5\text{-}2)$$

$$\epsilon_{i.j}=2\sqrt{\epsilon_i\cdot\epsilon_j}\left(\frac{(r_i^0)^3\cdot(r_j^0)^3}{(r_i^0)^6\cdot(r_j^0)^6}\right). \qquad (5\text{-}3)$$

Atomic partial charges are used to calculate the electrostatic interactions. The partial charge for each atom is computed by summing the bond increments, which are the transferable charge parameters (equation below)

$$q_i=\sum_j\delta_{ij} \qquad (5\text{-}4)$$

where *j* here denotes for all the atoms which are valence-bonded to atom *i*.

For the convenience of discussion, we denote C atoms in benzene rings as atom type C1, C in CH_2 as C2, C in CNT as C1*, H in C–H as H1, and H in O–H as H2. This nonreactive forcefield is not appropriate for chemical reactions (involving bond breaking/formation), if any, induced by shock loading. Our MD simulations are performed with the large-scale atomic/molecular massively parallel simulator (LAMMPS) package.[100] Periodic boundary conditions are applied along all three directions in nonshock simulations but only along the two directions orthogonal to the shock direction in shock simulations.

We construct a unit configuration of amorphous phenolic resin with XENOVIEW[187] via randomly placing 64 polymeric chains into a $2.7 \times 2.9 \times 10$ nm^3 supercell. Each such polymeric chain contains eight monomers [Figures 5.1(a) and 5.2(a)]. A similar structure was studied with the reactive forcefield, ReaxFF.[172] This unit configuration (7296 atoms) is equilibrated with the constant-pressure-temperature (*NPT*) ensemble and a time step of 0.25 fs, and then replicated by $2 \times 2 \times 8$. The resulting configuration (233472 atoms, or $5.4 \times 5.7 \times 80.6$ nm^3 in edge lengths) is further equilibrated at ambient conditions with a time (t) step of 0.25 fs and reaches a density of $\rho_0 = 1.12$ g cm^{-3}, and is adopted as the projectile for shock simulations. A larger configuration ($2 \times 2 \times 12$; $5.4 \times 5.7 \times 120.6$ nm^3) is also constructed and equilibrated for shock simulations.

A CNT composite unit configuration consists of a capped single-wall CNT with (10,0) chirality embedded in phenolic resin containing 64 polymeric chains, and is $2.9 \times 2.9 \times 10$ nm^3 in edge lengths. The CNT is ~ 0.78 nm in diameter and 7.8 nm long. The phenolic resin chains are introduced randomly around the CNT. The van der Waals distance between the resin and CNT is 0.34 nm, similar to an earlier work for CNT-polyethylene composite modeled with a Tersoff–Brenner potential and united atom model potential.[188] This van der Waals distance thus induces the excluded volume between the CNT and the resin matrix, as seen in Figure 5.2(b). The composite unit is first equilibrated at 0.1 K with the constant-volume-temperature (*NVT*) ensemble for 40 ps, followed by thermal annealing procedure at constant volume, where the system is

heated with a ramp rate of 0.02 K fs^{-1} to 2000 K, equilibrated at 2000 K for 20 ps and then cooled to 300 K with the same ramp rate. The annealing procedure is repeated twice. Replications of the composite unit by $2 \times 2 \times 8$ and $2 \times 20 \times 1$ are adopted to construct configurations for longitudinal and transverse shock loading of the composites, respectively. The corresponding edge lengths are $5.7 \times 5.9 \times 84.1$ nm^3 (256640 atoms) and $5.7 \times 59.2 \times 10.5$ nm^3 (320800 atoms). [An example is shown in Figure 5.2(b)]. The resulting configurations (projectiles) are then equilibrated for 125 ps with the *NPT* ensemble at ambient conditions (ρ_0 = 1.18 g cm^{-3}) for shock simulations. The CNTs are tilted slightly as a result of relaxing these particular configurations.

The shock simulations adopt the projectile-wall geometry and microcanonical ensemble.[38,89,189] A desired particle velocity along the shock or *x*-direction, u_p, is added to the *x*-component of the thermal velocities for each atom within the projectile. (The loading direction is along the direction with the longest dimension for a given supercell. (See Figure 5.3) The other two directions orthogonal to the shock direction are *y*- and *z*-directions. Periodic boundary conditions are applied only along the *y*- and *z*-axes, and thus the nonimpact side of the projectile is a free surface. The bonds among the atoms on the impact and nonimpact surfaces are removed before simulation. The cell dimensions are fixed along the *y*- and *z*-directions, so the simulations mimic one-dimensional (1D) strain loading conditions as encountered in experiments. We choose wall/lj126 in LAMMPS as the wall. Upon impact, a shock wave is induced and propagates away from the wall into the projectile. For the CNT-composites, shock loading is applied either parallel or perpendicular to the CNTs, referred to as longitudinal and transverse loading, respectively. The time step for integrating the equation of motion is 0.5 fs, and run durations are up to 40 ps.

The atomic-level deformation can be characterized with the slip vector[157]

$$\boldsymbol{s}_i = -\frac{1}{n_s}\sum_{i \neq j}^{n}\left(\mathbf{x}_{ij} - \mathbf{X}_{ij}\right). \tag{5-5}$$

Here n is the number of the nearest neighbors to atom i, n_s is the number of the slipped neighbors j, and $\mathbf{x}_{ij}$ and $\mathbf{X}_{ij}$ denote the vector (between atom i and j) difference in current and reference configurations, respectively. The reference configurations are the preshock structures. Similarly, the maximum relative displacement is defined as[160]

$$s_i = \mathbf{x}_{ij} - \mathbf{X}_{ij} : \quad |\mathbf{x}_{ij} - \mathbf{X}_{ij}|_{max}. \tag{5-6}$$

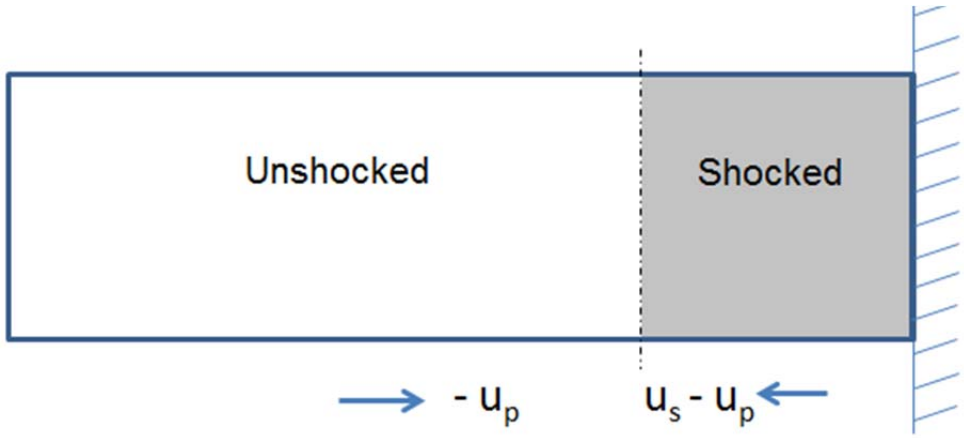

Figure 5.3 Schematic representation of shock wave generation by assigning a u_p to the material and hitting it to a wall.

The latter definition is used in our analysis, and the scalar slip is $s_i = |\boldsymbol{s}_i|$. Another technique for characterizing shear deformation is the local von Mises shear strain[113,129] but it is less revealing than $\mathbf{s}_i$ and thus not presented here.

We obtain the shock profiles of stress ($\sigma_{ij}; i,j = 1$, 2 and 3, or x, y, and z), temperature (T), density, and slip via 1D binning analysis.[95] Pressure P follows as $(1/3)(\sigma_{11} + \sigma_{22} + \sigma_{33})$, and the von Mises stress, $2\tau = \sigma_{11} - (1/2)(\sigma_{22} + \sigma_{33})$, where τ is the maximum shear stress.

Shock simulations are performed on pure phenolic resin and the CNT-resin composites along the longitudinal and transverse directions, and yield such profiles as stress, temperature, and slip as well as structure information. The stress (σ_{11}) evolutions, plotted in the traditional $x - t$ diagrams, illustrate wave propagation and interaction,

which result in the shocked and unshocked regions as well as the release fan originated on the free surface (Figure 5.4). We examine below the shock (Hugoniot) states, deformation, and related structural changes in pure resin and then the composites.

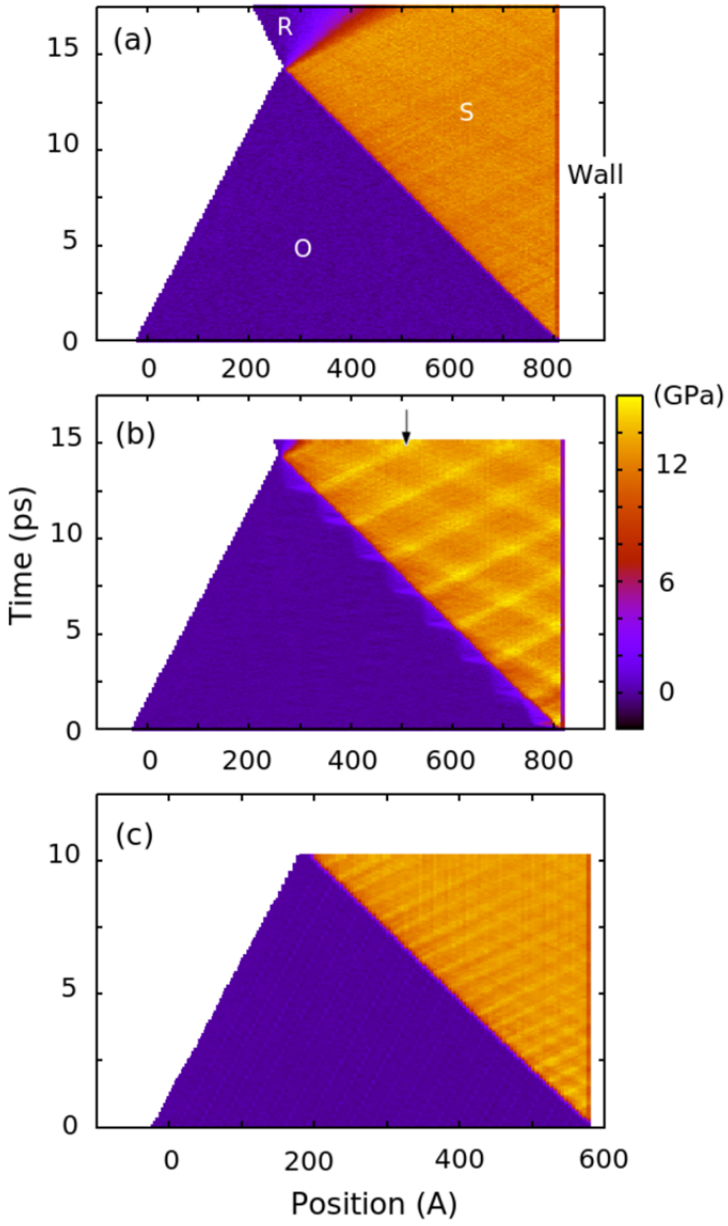

Figure 5.4 *x–t* diagrams for phenolic resin (a), and longitudinal loading (b) and transverse loading (c) of the CNT-resin composites ($u_p = 2$ km s^{-1}). Color coding is based on σ_{11}. *O*: unshocked; *S*: shocked; *R*: release fan.

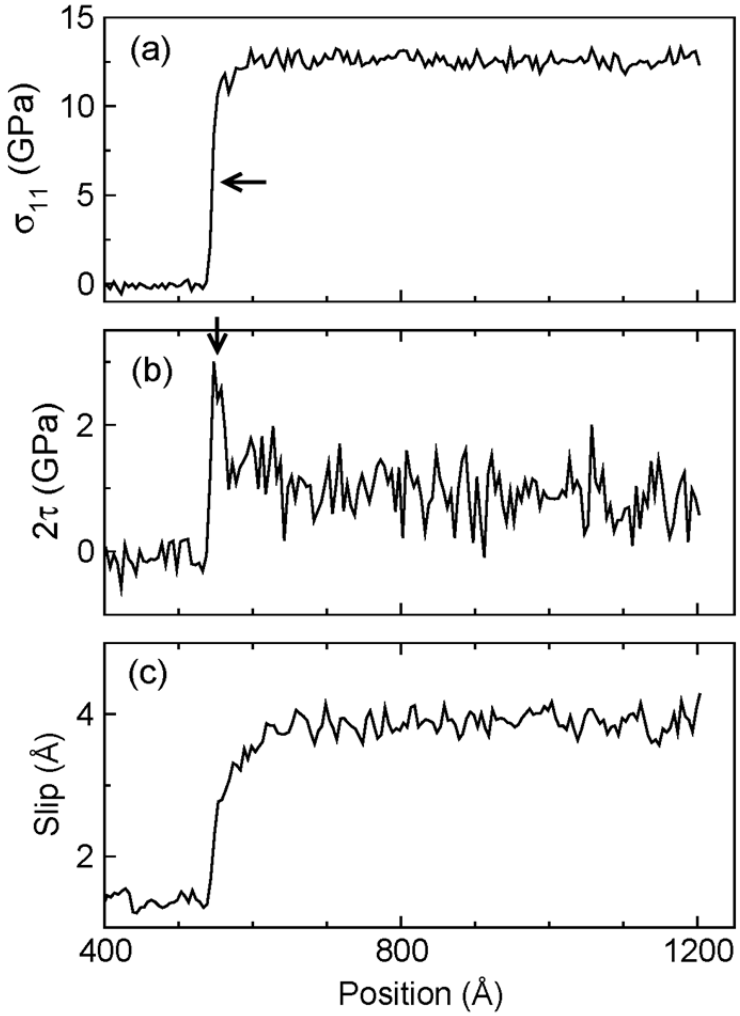

Figure 5.5 Shock profiles of phenolic resin, $\sigma_{11}(x)$, 2τ (x), and $s(x)$, at u_p = 2 km s^{-1}. Arrow: shock front.

5.3 Shock Response of Phenolic Resin

For phenolic resin, well supported shocks are observed in the $x - t$ diagrams and such profiles as $\sigma_{11}(x)$ and *T(x)* [e.g., Figures 5.4(a) and 5.5(a)]. For a given u_p, we obtain the Hugoniot state (denoted with a subscript H) values of $\sigma_{ii,H}$, P_H, and T_H; the

shock velocity u_s can thus be obtained from the jump condition as $u_s = \sigma_{11,H}/\rho_0 u_p$. ($us$ can be measured directly from the shock fronts as in experiments[176] but it may not represent the shock state given the complicated shock fronts.) The Hugoniot states are summarized in Figures 5.6 and 5.7.

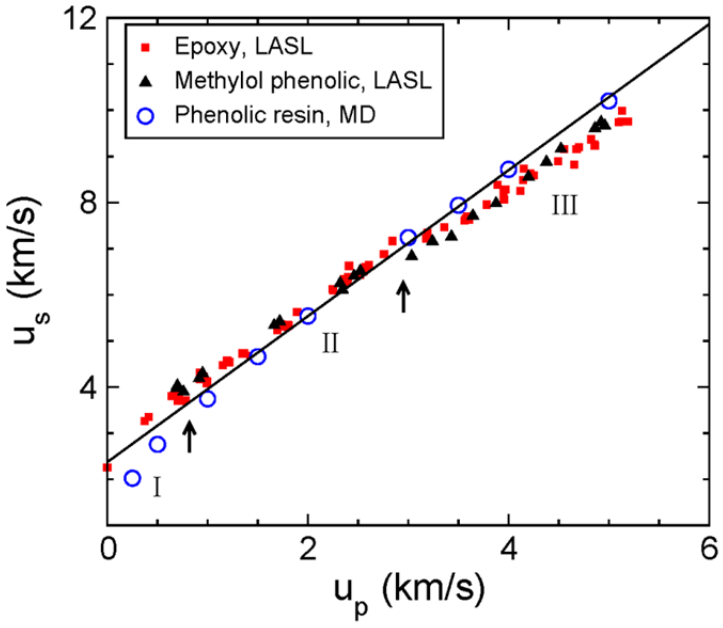

Figure 5.6 u_s–u_p relations for phenolic resin from direct MD shock simulations, and for two similar polymers from shock experiments (LASL) (Refs[1,2]). The solid line denotes a linear fit to the MD results at $u_p > 1$ km s^{-1} (The results for the CNT composites are similar to phenolic resin but omitted for clarity).

We observe in Figure 5.6 a well-defined linear $u_s - u_p$ relation for phenolic resin at $u_p > 1$ km s^{-1}: $u_s = 2.37 + 1.58u_p$ (km s^{-1}). However, the data points at $u_p \leq 1$ km s^{-1} concave upward, lying below the extrapolation of the linear relation. Epoxy and methylol phenolic are two polymers similar to phenolic resin in their monomers and densities (Figure 5.1); $\rho_0 = 1.192$ g cm^{-3}, 1.385 g cm^{-3}, and 1.12 g cm^{-3}, respectively.[191] We thus compare the experiments on epoxy and methylol resin with our simulations of

phenolic resin. Agreement is found approximately in the range of $1 < u_p < 3$ km s^{-1}; and the deviation from the linear extrapolation at the low u_p end appears to be common for all the three polymers. On the other hand, a phase change with a noticeable density increase is indicated at $u_p > 3$ km s^{-1} by the experiments but this feature is missing in the simulations.

As discussed by Carter and Marsh,[191] the experimental $u_s - u_p$ relations for a large number of polymers show three distinct regimes (I–III, with increasing u_p), schematically divided by the two arrows in Figure 5.6. Regime I shows a strong curvature, followed by regime II with a normal, linear $u_s - u_p$ relation. As a result, extrapolation of regime II to zero up yields a u_s value above the ambient bulk sound speed. The detailed experimental study on polymethyl methacrylate (PMMA) is a solid

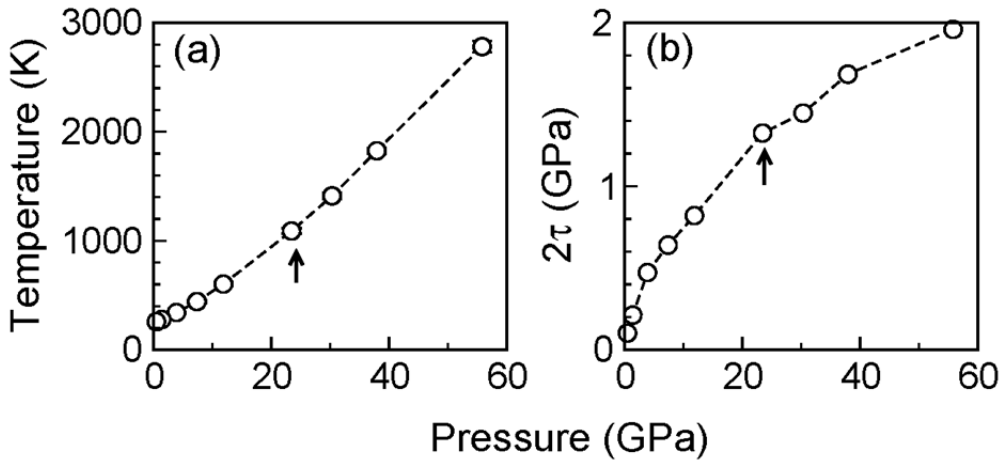

Figure 5.7 Shock state temperature (a) and 2τ (b) vs shock pressure for phenolic resin. The arrows indicate an expected phase change missing in our simulations.

example of this "general" observation.[176] The curvature in Regime I can be explained with the interatomic potentials.[1] Regime III is also linear, and considerable volume reduction occurs upon the II–III transition. They argued that this "phase transition" is neither polymorphic transformation in the usual crystallographic sense nor

melting/vaporization, and that the breaking of covalent bonds within chains and subsequent reformation of tetravalent bonds between chains lead to large volume changes.[191] The failure of our simulations to predict the II–III transition is consistent with its chemical nature inferred, since the bond breaking and formation are not allowed by the current forcefield. Therefore, reactive forcefields such as ReaxFF[172] are necessary. The simulation results appear to be accurate up to u_p = 3 km s^{-1}. The shock temperature near the transition is about 1100 K (u_p = 3 km s^{-1} and P_H = 23.4 GPa), lower than the value (~ 2000 K) estimated by Carter and Marsh.[191]

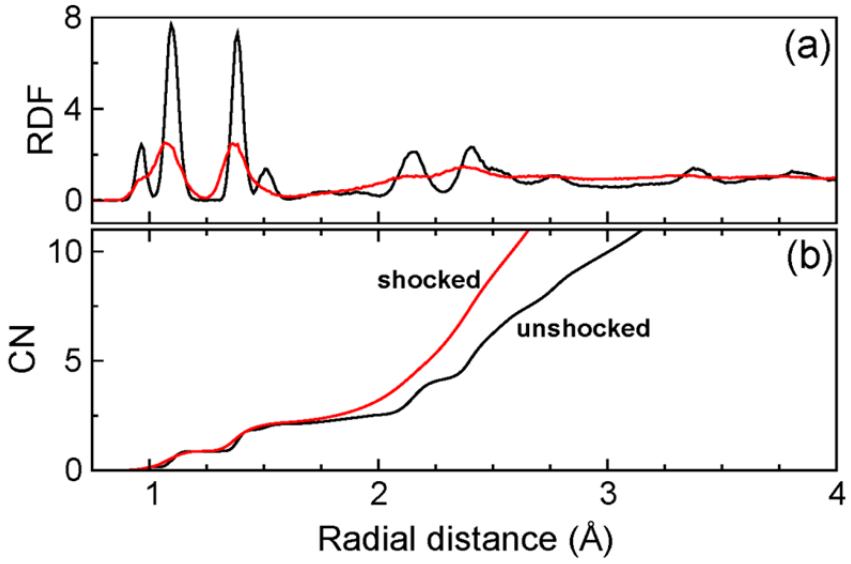

Figure 5.8 Total RDF of phenolic resin (RDF; a) and the corresponding CN (b) vs the radial distance in the shocked and unshocked regions (u_p=3 km s^{-1}).

We calculate the radial distribution functions (RDFs) of phenolic resin in shocked and unshocked regions, and Figure 5.8 shows the total RDFs and the corresponding coordination numbers (CN) for u_p = 3 km s^{-1}. Upon shock, the sharp peaks of the unshocked resin are smeared considerably; the average CN for the first neighbors is small and remains unchanged, while CN increases for the second shell and

beyond. Since calculating $\mathbf{s}_i$ requires a sufficient number of nearest neighbors, we choose a cutoff distance of 2.5 Å. As an example, Figure 5.9 shows a snapshot with color-coding based on s_i, which reveals clearly the shocked and unshocked regimes in phenolic resin (u_p = 2 km s^{-1}).

The dynamics of plastic deformation in shocked resin may be manifested in that of the von Mises stress 2τ. Upon shock arrival, 2τ rises rapidly to a peak value, $2\tau_{\max}$ [as indicated by the arrow in Figure 5.5(b)], and it then reaches a steady shock state value, $2\tau_H$. If $2\tau_{\max} > 2\tau_H$ (shear stress relaxation), the shocked region undergoes plastic deformation. Figure 5.5(b) shows such stress relaxation due to plastic deformation, via the microscopic slip [Figures 5.5(c) and 5.9]; and the relaxation dynamics is nearly identical in $2\tau(x)$ and $s(x)$, as expected [Figures 5.5(b) and 5.5(c)]. In the case of plastic deformation, the shock front widths in $\sigma_{11}(x)$ [Figure 5.5(a)] is much narrower than its counterparts in shear properties [Figures 5.5(b) and 5.5(c)], similar to a shocked metallic glass.[142]

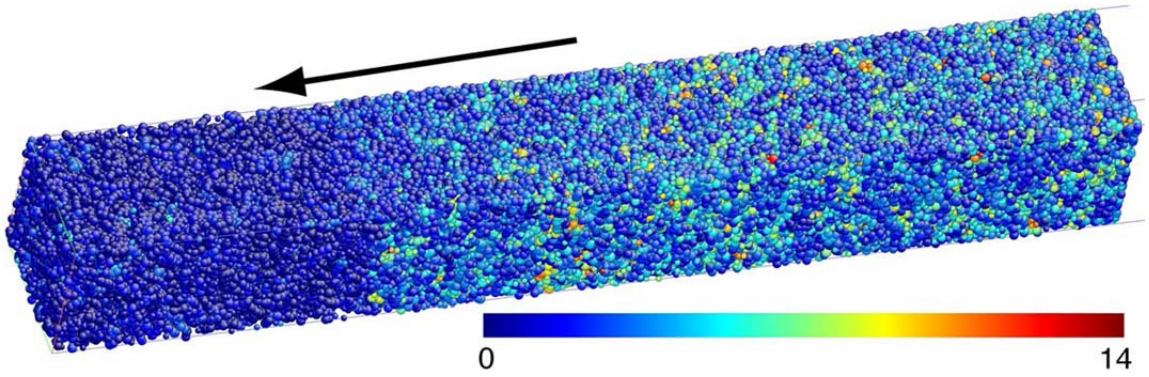

Figure 5.9 Snapshot of phenolic resin shock-loaded at u_p = 2 km s^{-1}. Color coding is based on the total slip s in angstrom. Arrow: shock direction.

The elastic precursor is not definitely identified in our simulations, similar to experiments.[164,176] The shock front [Figure 5.5(a)] shows a rapid rise followed by a

rounding up to the shock plateau, a feature well documented in experiments.[176] In metallic glass simulations, this rounding is related to plastic deformation.[142] However, such rounding in phenolic resin occurs even at u_p = 0.25 km s^{-1} (elastic shock; see below), likely due to viscoelastic behavior.[176] (Both viscoelasticity and rate-dependent plasticity play a role at higher shock strengths.) Since there is no crystalline order in phenolic resin, there are no definitive structure features related to its plasticity as dislocations to crystal plasticity. The shear stress relaxation is a best indication of the elastic–plastic transition, and is absent at u_p < 0.5 km s^{-1} (thus presumably elastic). The well-defined values of $2\tau_H$ increase with increasing shock strength, indicating strain hardening of the shocked resin [Figure 5.7(b)]. ($2\tau_{\max}$ also increases with increasing shock strength.) Such strain or work hardening has been observed in both experiments and simulations of polymers.[174,177]

Atomic-level slip leads to the plastic deformation in phenolic resin; however, different types of atoms may differ in slip. Before shock, all atoms undergo slip solely due to thermal fluctuations, and *s* increases in the order of C1 (C2), O, H1, and H2, varying in the range of 1–2 Å (Figure 5.10). Upon shock, *s* escalates to about 2.8 Å, 4 Å, and 5 Å for C, O, and H, respectively; and *s* is the same for H1 and H2 atoms, and C1 and C2 atoms (Figure 5.10). The average preshock value of *s* is about 1.4 Å (Figure 5.5). The atomic slip resistance increases in the order of H, O, and C, and such differences may give rise to localized shear deformation, similar to the observation on a metallic glass.[142] The backbone of a polymeric chain is composed of C atoms, and the stiffness of the backbone may enhance the slip resistance of C atoms. At longer range, the orientation of a segment in a chain may also affect its deformation.[174] Therefore, the slip directions do not necessarily follow the presumed maximum shear stress directions (45°), as seen in Figure 5.9. These structural inhomogeneities (intrachain and interchain) prevent the formation of long-range slips (so the slip deformation is localized, Figure 5.9) and frustrate the plastic deformation, which may lead to strain hardening.

Plastic deformation in shock-loaded polymers has long been a subject of controversy,[164,176,191] and the lack of elastic precursors certainly contributes to this

debate. For example, Schmidt and Evans[164] proposed that PMMA yields in a wide range of stresses (no definite shear strength), while Barker and Hollenbach[176] argued that there is a definite yield point in PMMA, and the missing elastic precursor could be due to similar elastic and plastic waves velocities. In our simulations, the absence or presence of shear stress relaxations in phenolic resin appears to be able to define the elastic–plastic transition (at $u_p \sim 0.5$ km s^{-1} or $\sigma_{11,H} \sim 1.5$ GPa), thus favoring Barker and Hollenbach's argument. Rate-dependent viscoelasticity and plasticity, and work-hardening may have collectively contributed to the peculiar shock front features in polymers.

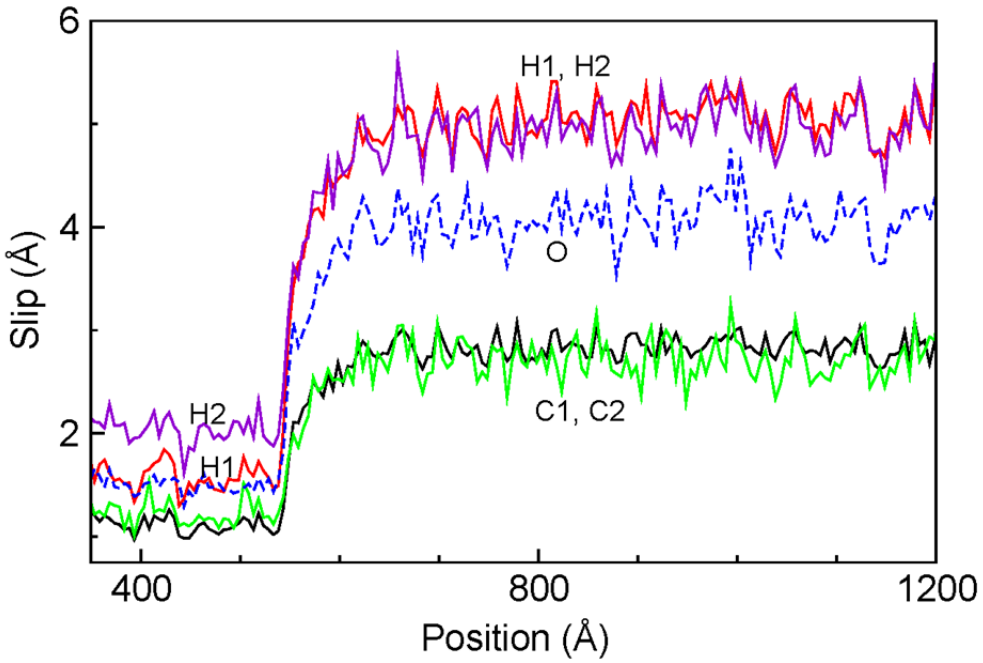

Figure 5.10 $s(x)$ profiles of individual atom types for phenolic resin shocked at $u_p = 2$ km s^{-1}.

5.4 Shock Response of the CNT-resin Composites

Shock loading is applied to the CNT-resin composites at the same u_p as to the pure resin. For the particular nanocomposites explored, incorporating CNTs in phenolic resin does induce certain observable features in the mechanical behavior, and the composites show anisotropic response to shock loading in compression and shear.

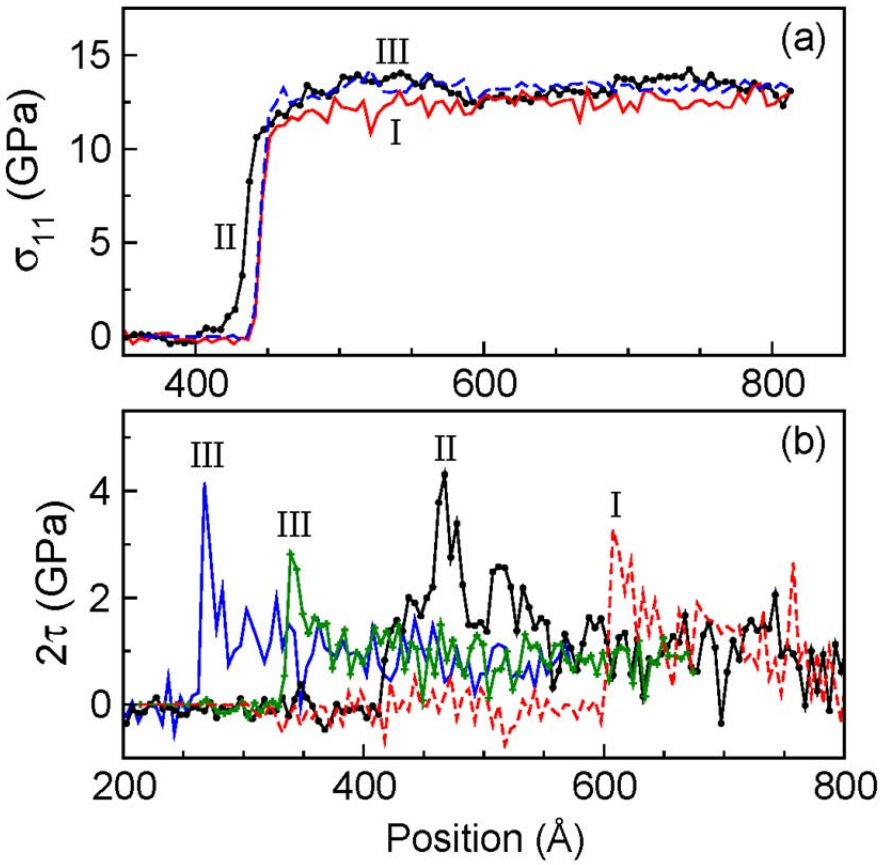

Figure 5.11 Profiles of $\sigma_{11}(x)$ (a) and $2\tau(x)$ (b) for the CNT-resin composites and pure resin at selected instants ($u_p = 2$ km s^{-1}). Some curves are shifted along the x-axis for comparison. I: pure resin; II: longitudinal loading of the composite, and III: transverse loading.

Due to the higher shock impedance of CNTs (mostly higher elastic constants and shock velocity) as compared to the resin matrix, stress concentrations are induced upon compression. Such stress concentrations are manifested as "stripes" in the $x - t$ diagrams

[Figures 5.4(b) and 5.4(c); a stripe is indicated by an arrow]. The right-tilting stripes are due to shock enhancement by the CNTs at the internal interfaces (between the resin matrix and CNTs), and the left-tilting stripes, by the high-impedance reflecting wall. (This phenomenon is essentially reshock or double-shock.) The numbers of such stress concentrations match those of CNTs in the unshocked composites for both longitudinal

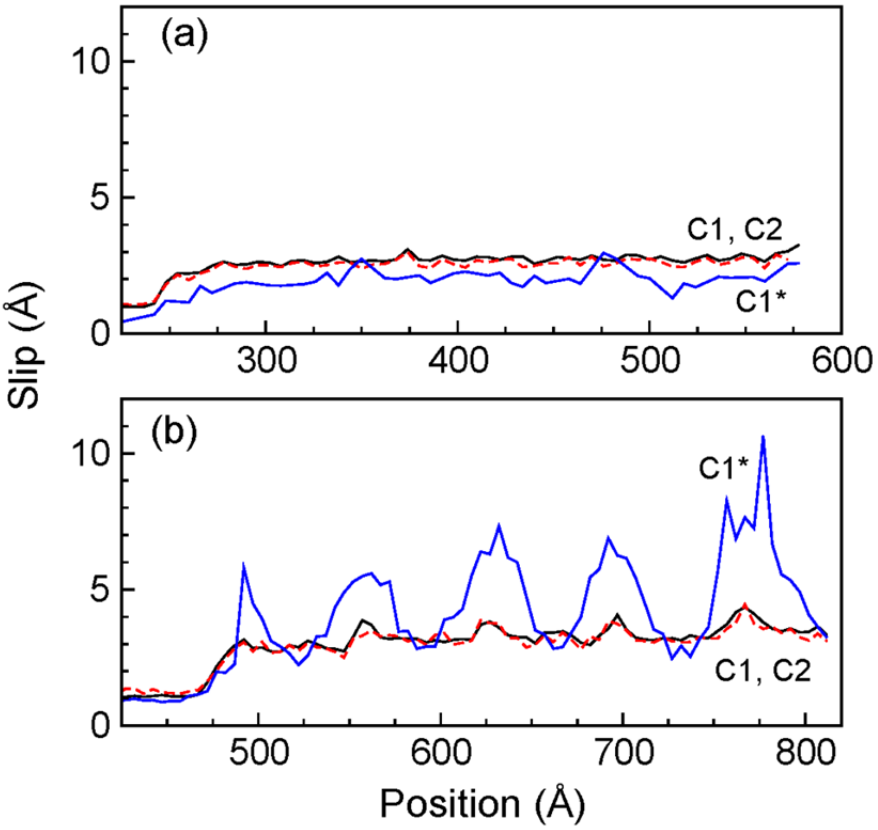

Figure 5.12 Slip profiles, $s(x)$, for different C atom types in the CNT-resin composites subject to transverse (a) and longitudinal loading $u_p = 2$ km s^{-1}.

and transverse loading. This reshock yields spatial fluctuations in stress at a given time, e.g., Figure 5.11(a), as well as temporal fluctuations for a given position. These fluctuations are inherent in dynamic response of structured materials, and depend on the geometry of CNTs within the matrix.

Figure 5.11(a) compares three wave profiles where the shocks are initiated at the same position (the wall) and recorded at the same time (10 ps). The shock front for the longitudinal loading leads slightly that for the transverse loading of the composite as well as that for the pure resin. The shock velocities for the latter two are similar. A precursor is also observed at the foot of the shock front for the longitudinal loading. The higher wave speed in CNTs and the CNT geometry directly lead to the differences in the shock fronts. The length ratios (the total length of CNTs to the cell length) along the

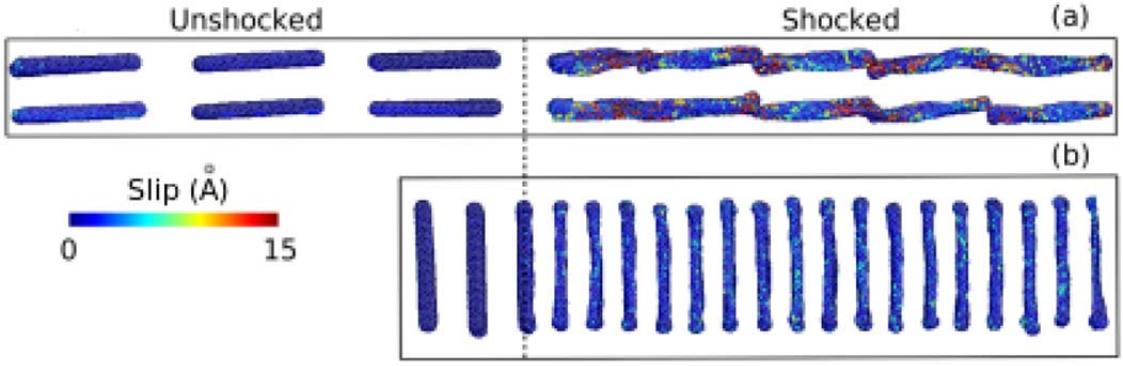

Figure 5.13 Snapshots of CNT deformation within the CNT-resin composite under longitudinal (a) and transverse loading _b_ at u_p = 2 km s^{-1}. The dashed line indicates shock front.

shock direction for the longitudinal and transverse loading are about 0.74 and 0.26, respectively, so the CNT effect on shock velocity is more pronounced for the longitudinal loading. We obtain $\sigma_{11,H}$ via averaging the shocked regime, and $\sigma_{11,H}$ achieved in the composites is sightly higher than the pure resin. Thus, CNTs increase the compressional "stiffness" of the resin, although this increase is not pronounced given the small CNT fraction (and length ratios). The volume ratio of CNTs in the nanocomposites is about 9%. Nonshock simulations on CNT-polyethylene composites yielded similar results.[168] (A recent shock simulation of CNT-SiC composites showed more pronounced

effect of CNTs.[173]) Increasing the length and volume ratios should have a positive effect both on the shock front characteristics and shock states.

Besides the compressional stiffness, CNTs also increase the shear resistance of resin as a structure component in the composites. Figure 5.11(b) shows the profiles of $2\tau(x)$ at selected time instants for pure resin and the composites, which reveal relaxation in 2τ behind the shock front to a steady state. Depending on where the shock front traverses (resin or CNTs), $2\tau_{\max}$ can vary substantially for the composites. For u_p = 2 km s^{-1}, $2\tau_{\max}$ increases from about 3 GPa in the pure resin to 4 GPa in CNT-regions; the shock front in the longitudinal loading is broader than the transverse loading due to different CNT alignment geometry [Figure 5.11(b)]. (It is easier to increase the length ratio and thus the yield strength in the longitudinal loading.) However, CNT appears to have diminished effect on the steady state shear strength, $2\tau_H$. ($2\tau_H$ is comparable for pure resin and the composites simulated here, regardless the loading direction.) We expect that increasing the volume ratio of CNTs may further improve the shear strengths at a shock front (onset of plasticity) and steady shock state.

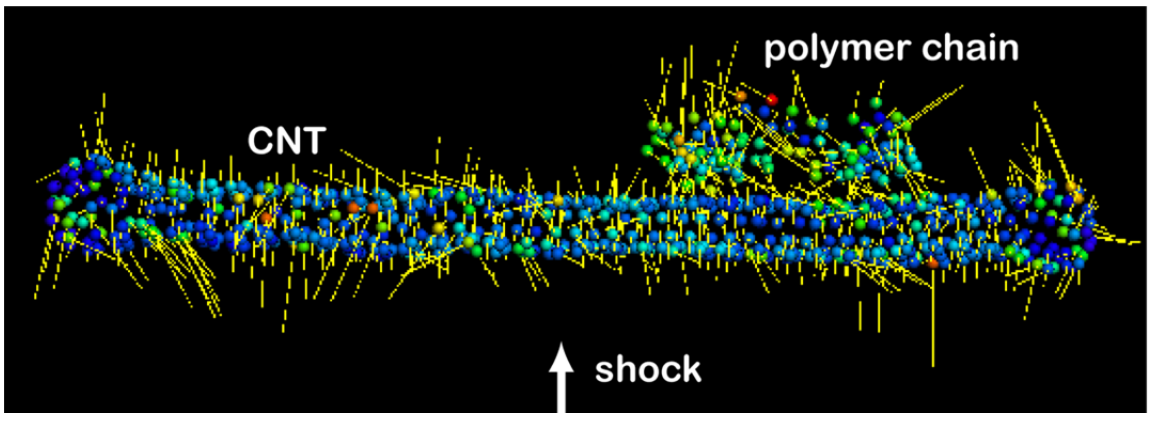

Figure 5.14 Deformation snapshot of a CNT and a neighboring polymer chain within the CNT-resin composite under transverse loading. Each atom is annotated with the slip vector and color coded according to *s* (u_p=2 km s^{-1}). Visualization adopts Ovito (Ref.[190]).

In the CNT-resin composites, the plastic deformation is also manifested as shear stress relaxation and accompanied by slip. For transverse loading, the slip profiles are relatively smooth and the steady state slip, s_H, is about 3.6 Å at u_p = 2 km s^{-1}, slightly lower than the pure resin (3.9 Å), while there are large fluctuations in $s(x)$ for the longitudinal loading, and s_H is about 5 Å. Such observations can be explained with the $s(x)$ profiles of individual atom types in the composites (Figure 5.12; more mobile O, H1, and H2 atoms are omitted for clarity). The C1* atoms (CNT) slip less than C1 and C2 atoms in transverse loading but much more in the longitudinal loading. The $s(x)$ profile of C1* atoms in the transverse case lacks the pronounced fluctuations seen in the longitudinal case. In the latter case, the slip peaks in C1* occur concurrently with those in C, H, and O atoms in the resin matrix. Thus, the CNT geometry directly affects the slip behavior of the composites.

The anisotropic deformation/damage of CNTs under shock loading is examined in more detail in Figures 5.13 and 5.14 (using u_p = 2 km s^{-1} as an example). For the longitudinal loading, the CNTs are distorted with slip and twisting as well as compression-related diameter changes; the regions near the tube ends undergo the most amounts of slip, leading to the slip peaks in $s(x)$ [Figure 5.12(b)]. For transverse loading, the most pronounced feature is the crushing of CNTs along the shock direction, and the tube ends are bulged relative to the rest of the tube [Figures 5.13(b) and 5.14]. Thus, compression, shear and torsion are involved to different extents in the CNT deformation for both loading cases. The difference in the deformation for these two loading cases can be correlated with the CNT cross-section normal to the shock direction (impact cross-section): it is about 1 nm^2 and 8.7 nm^2, respectively, for the longitudinal and transverse loading. In the longitudinal loading, the small cross-section of a stiffer CNT embedded in a soft resin matrix leads to more pronounced deformation (particularly slip); the CNT ends have less constraint than its center portion and are more susceptible to slip [Figure 5.13(a)], except some CNT caps. The cap itself appears more rigid overall in the transverse loading likely due to its geometry, while some highly slipped atoms are observed in the cap region (Figure 5.14). A neighboring polymeric chain shows

complicated slip (Figure 5.14). At higher shock strengths, a shocked CNT is severely deformed/damaged beyond recognition.

CHAPTER VI

CONCLUSIONS

6.1 Summary

We have characterized the shock states, plasticity; shear flow strength, spallation, and related structural features of $Cu_{46}Zr_{54}$ metallic glasses under adiabatic 1D strain shock wave loading. The plasticity is manifested as STZs. Our work and previous results by others suggest that STZ appears to be common to the plastic deformation in metallic glasses under both shock and nonshock loading conditions. Transient strain hardening and shock-state softening are observed, and can be related to the evolution dynamics of STZs. The void nucleation for spallation occurs preferentially at highly shear-deformed sites. The Voronoi and local shear strain analyses show that atoms with different local environments, characterized in terms of Voronoi polyhedron types, have different shear resistances. In particular, the atoms indexed with <0,0,12,0> are most shear-resistant, and those with <0,2,8,1> are highly prone to shear flow. This atomic-level structural inhomogoneity leads to inhomogeneous shear deformation and thus STZs, which in turn play a key role in plasticity as well as void nucleation and growth. STZ is of structural rather than thermal origin (at least at current MD time scales). The local atomic structures may change dynamically in response to loading and unloading. Such complex structure changes could be achieved via the bond exchange or rearrangement as suggested for topological structure changes.

Understanding the process of shear band formation in metallic glasses is critical to improve their mechanical properties. It is reported that amorphous-crystalline interfaces (ACIs) in nanolaminates can play an important role as a source and sink of dislocations. However, the effects of ACIs on shear banding are still lacking. Under the similar loading conditions (uniaxial compression) where shear bands are observed in the bulk metallic glass, our simulations show that shear bands can form in thin glass layers (5−10 nm) of the $Cu/Cu_{46}Zr_{54}$ glass nanolaminates. The mechanisms of shear banding

are different in these two cases. In the former case, small shear bands are randomly nucleated near the free surfaces and some of them grow and become dominant, while shear banding in the glass layer is induced by dislocations via ACIs. We reveal that partial and full dislocations occur in the Cu layer, and screw dislocations, near the amorphous−crystalline interfaces (ACIs). Shear bands are directly induced by the dislocations in the crystalline Cu layer through ACIs, and grow from the ACIs into the glass layers and absorb ambient STZs. Plasticity in the glass layers is realized via pronounced, stable shear banding.

We have characterized the shock response of phenolic resin and the CNT-resin composites under longitudinal and transverse loading. The simulated shock states of phenolic resin agree with the experiments but fail to predict the phase change observed in experiments, likely because such phase change involves bond breaking and formation. The plastic deformation in phenolic resin is achieved via atomic level slip accompanied by shear stress relaxation. Phenolic resin also shows strain hardening, which could be caused by the frustrated slip related to intrachain and interchain inhomogeneities. The CNT-resin composites demonstrate anisotropy in wave propagation, yield and CNT deformation/damage. The CNTs induce stress concentrations in the composites and may increase the yield strength. Our simulations suggest that the bulk shock response of the composites depends on the volume fraction, length ratio, impact cross-section, and geometry of the CNT components; the short CNTs in current simulations have insignificant effect on the bulk response of resin polymer.

REFERENCES

1 Inoue, A. Stabilization of metallic supercooled liquid and bulk amorphous alloys. *Acta Mater* **48**, 279-306 (2000).

2 Schuh, C. A., Nieh, T. G. A survey of instrumented indentation studies on metallic glasses. *J. Mater. Res.* **19**, 46-57 (2004).

3 Wang, Y. M., Li, J., Hamza, A. V. & Barbee, T. W. Ductile crystal line-amorphous nanolaminates. *P Natl Acad Sci USA* **104**, 11155-11160 (2007).

4 Wang, W. H., Dong, C. & Shek, C. H. Bulk metallic glasses. *Mater. Sci. Eng. R-Rep.* **44**, 45-89 (2004).

5 Schuh, C. A., Hufnagel, T. C. & Ramamurty, U. Overview No.144 - Mechanical behavior of amorphous alloys. *Acta Mater* **55**, 4067-4109 (2007).

6 Loffler, J. F. Bulk metallic glasses. *Intermetallics* **11**, 529-540 (2003).

7 Johnson, W. L. Bulk amorphous metal - An emerging engineering material. *Jom-J Min Met Mat S* **54**, 40-43 (2002).

8 Inoue, A. & Takeuchi, A. Recent progress in bulk glassy alloys. *Mater. Trans.* **43**, 1892-1906 (2002).

9 Greer, A. L. & Ma, E. Bulk metallic glasses: at the cutting edge of metals research. *Mrs Bull* **32**, 611-615 (2007).

10 Leach, A. R. *Molecular modelling: principles and applications*. 2nd ed., (Prentice Hall, 2001).

11 Alder, B. J. & Wainwright, T. E. Phase transition for a hard sphere system. *Journal of Chemical Physics* **27**, 1208-1209 (1957).

12 Rahman, A. Correlations in motion of atoms in liquid argon. *Phys Rev a-Gen Phys* **136**, A405-& (1964).

13 Allen, M. P. & Tildesley, D. J. *Computer simulation of liquids*. (Oxford University Press, 1987).

14 Frenkel, D. & Smit, B. *Understanding molecular simulation: from algorithms to applications*. 2nd ed., (Academic, 2002).

15 Rapaport, D. C. *The art of molecular dynamics simulation*. 2nd ed., (Cambridge University Press, 2004).

16 Raabe, D. *Computational materials science: the simulation of materials microstructures and properties*. (Wiley-VCH, 1998).

17 Erginsoy, C., Englert, A. & Vineyard, G. H. Dynamics of radiation damage in body-centered cubic lattice. *Phys Rev a-Gen Phys* **133**, A595-& (1964).

18 Gerold, V. *Structure of solids, Chapter 9: Structures of interfaces in crystalline solids, Volume 1* (VCH, 1993).

19 Finnis, M. W. & Sinclair, J. E. A simple empirical N-body potential for transition-metals. *Philos. Mag. A-Phys. Condens. Matter Struct. Defect Mech. Prop.* **50**, 45-55 (1984).

20 Hua, L., RafiiTabar, H. & Cross, M. Molecular dynamics simulation of fractures using an N-body potential. *Phil Mag Lett* **75**, 237-244 (1997).

21 Sutton, A. P. & Chen, J. Long-range Finnis Sinclair potentials. *Phil Mag Lett* **61**, 139-146 (1990).

22 Baskes, M. I. Modified embedded-atom potentials for cubic materials and impurities. *Phys Rev B* **46**, 2727-2742 (1992).

23 Daw, M. S. & Baskes, M. I. Semiempirical, quantum-mechanical calculation of hydrogen embrittlement in Metals. *Phys Rev Lett* **50**, 1285-1288 (1983).

24 Daw, M. S. & Baskes, M. I. Embedded-atom method - derivation and application to impurities, surfaces, and other defects in metals. *Phys Rev B* **29**, 6443-6453 (1984).

25 Brenner, D. W. Empirical potential for hydrocarbons for use in simulating the chemical vapor-deposition of diamond films. *Phys Rev B* **42**, 9458-9471 (1990).

26 Rosato, V., Guillope, M. & Legrand, B. Thermodynamical and structural-properties of Fcc transition-metals using a simple tight-binding model. *Philos. Mag. A-Phys. Condens. Matter Struct. Defect Mech. Prop.* **59**, 321-336 (1989).

27 Hohenberg, P. & Kohn, W. Inhomogeneous electron gas. *Phys Rev B* **136**, B864-& (1964).

28 Griebel, M., Knapek, S. & Zumbusch, G. W. *Numerical simulation in molecular dynamics: numerics, algorithms, parallelization, applications*. (Springer, 2007).

29 Hill, T. L. *An introduction to statistical thermodynamics*. (Addison-Wesley Pub. Co., 1962).

30 Berendsen, H. J. C., Postma, J. P. M., Vangunsteren, W. F., Dinola, A. & Haak, J. R. Molecular-dynamics with coupling to an external bath. *Journal of Chemical Physics* **81**, 3684-3690 (1984).

31 Andersen, H. C. Molecular-dynamics simulations at constant pressure and-or temperature. *Journal of Chemical Physics* **72**, 2384-2393 (1980).

32 Nose, S. A Unified formulation of the constant temperature molecular-dynamics methods. *Journal of Chemical Physics* **81**, 511-519 (1984).

33 Meyers, M. A. *Dynamic behavior of materials*. (Wiley, 1994).

34 Asay, J. R. & Shahinpoor, M. *High-pressure shock compression of solids*. (Springer-Verlag, 1993).

35 Zel'dovich, Y. B., Raizer, I. U. P., Hayes, W. D. & Probstein, R. F. *Physics of shock waves and high-temperature hydrodynamic phenomena*. (Academic Press, 1966).

36 Antoun, T. *Spall fracture*. (Springer-Verlag, 2003).

37 Grady, D. E. The spall strength of condensed matter. *J. Mech. Phys. Solids* **36**, 353-& (1988).

38 Luo, S. N., Han L. B., Xie, Y., An, Q., Zheng, L., Xia, K. The relation between shock-state particle velocity and free surface velocity: A molecular dynamics study on single crystal Cu and silica glass. *J Appl Phys* **103**, 093530 (2008).

39 Walsh, J. M. & Christian, R. H. Equation of state of metals from shock wave measurements. *Phys Rev* **97**, 1544-1556 (1955).

40 Wackerle, J. Shock-wave compression of quartz. *J Appl Phys* **33**, 922-& (1962).

41 Rice, M. H., Mcqueen, R. G. & Walsh, J. M. Compression of solids by strong shock waves. *Solid State Phys* **6**, 1-63 (1958).

42 Altshuler, L. V. Use of shock waves in high-pressure physics. *Sov Phys Uspekhi* **8**, 52-& (1965).

43 Duval, G. E. & Graham, R. A. Phase-transitions under shock-wave loading. *Rev Mod Phys* **49**, 523-579 (1977).

44 Wentorf, R. H. *Modern very high pressure techniques*. (Butterworths, 1962).

45 Chou, P. C. & Hopkins, A. K. *Dynamic response of materials to intense impulsive loading*. (Air Force Materials Laboratory, 1973).

46 Mcqueen, R. G. & Marsh, S. P. Equation of state for 19 metallic elements from shock-wave measurements to 2 Megabars. *J Appl Phys* **31**, 1253-1269 (1960).

47 Kinslow, R. *High-velocity impact phenomena*. (Academic Press, 1970).

48 Asay, J. R. & Chhabildas, L. C. Role of shock compression technique for scientific and engineering studies. *Proceedings of the 2nd International Symposium on Intense Dynamic Loading and Its Effects*, 220-226 (1992).

49 Crozier, W. D. & Hume, W. High-velocity, light-gas gun. *J Appl Phys* **28**, 892-894 (1957).

50 Hawke, R. S., Susoeff, A. R., Asay, J. R., Ang, J.A., Hall, C. A. *et al.* Railgun performance with a 2-stage light-gas gun injector. *Ieee T Magn* **27**, 28-32 (1991).

51 Shahinpoor, M. & Hawke, R. S. Analytic solutions to dynamic equations of plasma armature railguns. *Ieee T Magn* **25**, 508-513 (1989).

52 Hawke, R. S., Susoeff, A. R., Asay, J. R., Balk, J. K., Hall, C. A. *et al.* Starfire - hyper-velocity railgun development for high-pressure research. *Ieee T Magn* **25**, 223-227 (1989).

53 Boustie, M., Resseguier, T. D., Hallouin, M., Migault, A., Romain, J. P. *et al.* Some applications of laser-induced shocks on the dynamic behavior of materials. *Laser Part Beams* **14**, 225-235 (1996).

54 Cauble, R., Phillion, D. W., Hoover, T. J., Holmes, N. C., Kilkenny, J. D. *et al.* Demonstration of 0.75 Gbar planar shocks in x-Ray driven colliding foils. *Phys Rev Lett* **70**, 2102-2105 (1993).

55 Lower, T., Sigel, R., Eidmann, K., Foldes, I. B., Huller, S. *et al.* Uniform multimegabar shock-waves in solids driven by laser-generated thermal-radiation. *Phys Rev Lett* **72**, 3186-3189 (1994).

56 Tollier, L., Fabbro, R. & Bartnicki, E. Study of the laser-driven spallation process by the velocity interferometer system for any reflector interferometry technique. I. Laser-shock characterization. *J Appl Phys* **83**, 1224-1230 (1998).

57 Trainor, R. J., Shaner, J. W., Auerbach, J. M. & Holmes, N. C. Ultrahigh-pressure laser-driven shock-wave experiments in aluminum. *Phys Rev Lett* **42**, 1154-1157 (1979).

58 Bolis, C., Berthe, L., Boustie, M., Arrigoni, M., Barradas, S. *et al.* Physical approach to adhesion testing using laser-driven shock waves. *J Phys D Appl Phys* **40**, 3155-3163 (2007).

59 Anderhol, N. C. Laser-generated stress Waves. *Appl. Phys. Lett.* **16**, 113-& (1970).

60 Fabbro, R., Fournier, J., Ballard, P., Devaux, D. & Virmont, J. Physical study of laser-produced plasma in confined geometry. *J Appl Phys* **68**, 775-784 (1990).

61 Sollier, A., Berthe, L. & Fabbro, R. Numerical modelling of the transmission of breakdown plasma generated in water during laser shock processing. *Eur Phys J-Appl Phys* **16**, 131-139 (2001).

62 Klement, W., Willens, R. H. & Duwez, P. Non-crystalline structure in solidified gold-silicon alloys. *Nature* **187**, 869-870 (1960).

63 Turnbull, D. Under what conditions can a glass be formed. *Contemp Phys* **10**, 473-& (1969).

64 Inoue, A., Kato, A., Zhang, T., Kim, S. G. & Masumoto, T. Mg-Cu-Y amorphous-alloys with high mechanical strengths produced by a metallic mold casting method. *Mater T Jim* **32**, 609-616 (1991).

65 Zhang, T., Inoue, A. & Masumoto, T. Amorphous Zr-Al-Tm (Tm = Co, Ni, Cu) alloys with significant supercooled liquid region of over 100-K. *Mater T Jim* **32**, 1005-1010 (1991).

66 Peker, A. & Johnson, W. L. A highly processable metallic-glass-Zr41.2ti13.8cu12.5ni10.0be22.5. *Appl. Phys. Lett.* **63**, 2342-2344 (1993).

67 Koch, C. C., Cavin, O. B., Mckamey, C. G. & Scarbrough, J. O. Preparation of amorphous Ni60nb40 by mechanical alloying. *Appl. Phys. Lett.* **43**, 1017-1019 (1983).

68 Liu, B. X., Johnson, W. L., Nicolet, M. A. & Lau, S. S. Structural difference rule for amorphous alloy formation by ion mixing. *Appl. Phys. Lett.* **42**, 45-47 (1983).

69 Liu, B. X., Lai, W. S. & Zhang, Q. Irradiation induced amorphization in metallic multilayers and calculation of glass-forming ability from atomistic potential in the binary metal systems. *Mater. Sci. Eng. R-Rep.* **29**, 1-48 (2000).

70 Schwarz, R. B. & Johnson, W. L. Formation of an amorphous alloy by solid-state reaction of the pure polycrystalline metals. *Phys Rev Lett* **51**, 415-418 (1983).

71 Battezzati, L. & Baricco, M. An analysis of volume effects in metallic-glass formation. *J Less-Common Met* **145**, 31-38 (1988).

72 Egami, T. & Waseda, Y. Atomic size effect on the formability of metallic glasses. *J Non-Cryst Solids* **64**, 113-134 (1984).

73 Inoue, A. Bulk amorphous alloys with soft and hard magnetic properties. *Mater. Sci. Eng. A-Struct. Mater. Prop. Microstruct. Process.* **226**, 357-363 (1997).

74 Miracle, D. B. The efficient cluster packing model - An atomic structural model for metallic glasses. *Acta Mater* **54**, 4317-4336 (2006).

75 Ma, D., Stoica, A. D. & Wang, X. L. Power-law scaling and fractal nature of medium-range order in metallic glasses. *Nat Mater* **8**, 30-34, (2009).

76 Lee, M., Lee, C. M., Lee, K. R., Ma, E. & Lee, J. C. Networked interpenetrating connections of icosahedra effects on shear transformations in metallic glass. *Acta Mater* **59**, 159-170 (2011).

77 Wang, G. Y., Liaw, P. K., Yokoyama, Y., Inoue, A. & Liu, C. T. Fatigue behavior of Zr-based bulk-metallic glasses. *Mater. Sci. Eng. A-Struct. Mater. Prop. Microstruct. Process.* **494**, 314-323 (2008).

78 Buchanan, O. Bulk metallic glasses used for manufacturing net-shape metal products. *Mrs Bull* **27**, 850-851 (2002).

79 Liquid Metal Technologies, accessed in 2011, www.liquidmetal.com.

80 Conner, R. D., Rosakis, A. J., Johnson, W. L. & Owen, D. M. Fracture toughness determination for a beryllium-bearing bulk metallic glass. *Scripta Mater* **37**, 1373-1378 (1997).

81 Wang, Y. M., Hamza, A. V. & Barbee, T. W. Incipient plasticity in metallic glass modulated nanolaminates. *Appl. Phys. Lett.* **91**, 061924 (2007).

82 Zhang, Y., Xu, W., Tan, H. & Li, Y. Microstructure control and ductility improvement of La-Al-(Cu,Ni) composites by Bridgman solidification. *Acta Mater* **53**, 2607-2616 (2005).

83 Szuecs, F., Kim, C. P. & Johnson, W. L. Mechanical properties of Zr56.2Ti13.8Nb5.0Cu6.9Ni5.6Be12.5 ductile phase reinforced bulk metallic glass composite. *Acta Mater* **49**, 1507-1513 (2001).

84 Lee, M. L., Li, Y. & Schuh, C. A. Effect of a controlled volume fraction of dendritic phases on tensile and compressive ductility in La-based metallic glass. *Acta Mater* **52**, 4121-4131 (2004).

85 Grigsby, W., Bowes, B. T., Dalton, D. A., Bernstein, A. C., Bless, A. C. *et al.* Picosecond time scale dynamics of short pulse laser-driven shocks in tin. *J Appl Phys* **105**, 093523 (2009).

86 Paisley, D. L., Luo, S. N., Greenfield, S. R. & Koskelo, A. C. Laser-launched flyer plate and confined laser ablation for shock wave loading: validation and applications. *Rev Sci Instrum* **79**, 023902 (2008).

87 Dlott, D. D., Hambir, S. & Franken, J. The new wave in shock waves. *J Phys Chem B* **102**, 2121-2130 (1998).

88 Evans, R., Badger, A. D., Fallies, F., Mahdieh, M., Hall, T. A. *et al.* Time- and space-resolved optical probing of femtosecond-laser-driven shock waves in aluminum. *Phys Rev Lett* **77**, 3359-3362 (1996).

89 Holian, B. L. Atomistic computer-simulations of shock-waves. *Shock Waves* **5**, 149-157 (1995).

90 Kadau, K., Germann, T. C., Lomdahl, P. S., Albers, R. C., Wark, J. S. *et al.* Shock waves in polycrystalline iron. *Phys Rev Lett* **98** (2007).

91 Germann, T. C., Kadau, K. & Swaminarayan, S. 369 Tflop/s molecular dynamics simulations on the petaflop hybrid supercomputer 'Roadrunner'. *Concurreny and Computation-Practice & Experience* **21**, 2143 (2009).

92 Belak, J. in *Shock compression of condensed matter - 1997* Vol. 429 *Aip Conference Proceedings* (eds S. C. Schmidt, D. P. Dandekar, & J. W. Forbes) 211-214 (Amer Inst Physics, 1998).

93 Meyers, M. A., Traiviratana, S., Lubarda, V. A., Benson, D. J. & Bringa, E. M. The role of dislocations in the growth of nanosized voids in ductile failure of metals. *Jom* **61**, 35-41 (2009).

94 Srinivasan, S. G., Baskes, M. I. & Wagner, G. J. Atomistic simulations of shock induced microstructural evolution and spallation in single crystal nickel. *J Appl Phys* **101**, 7 (2007).

95 Luo, S. N., An, Q., Germann, T. C. & Han, L. B. Shock-induced spall in solid and liquid Cu at extreme strain rates. *J Appl Phys* **106**, 8 (2009).

96 Dremov, V., Petrovtsev, A., Sapozhnikov, P., Smirnova, M., Preston, D. L. *et al.* Molecular dynamics simulations of the initial stages of spall in nanocrystalline copper. *Phys Rev B* **74**, 5 (2006).

97 Holian, B. L. & Lomdahl, P. S. Plasticity induced by shock waves in nonequilibrium molecular-dynamics simulations. *Science* **280**, 2085-2088 (1998).

98 Holian, B. L. Modelling shock-wave deformation via molecular-dynamics. *Phys. Rev. A* **37**, 2562-2568 (1988).

99 Mendelev, M. I., Sordelet, D. J. & Kramer, M. J. Using atomistic computer simulations to analyze x-ray diffraction data from metallic glasses. *J Appl Phys* **102**, 7 (2007).

100 Lammps Molecular Dynamics Simulator, accessed in 2010, http://lammps.sandia.gov.

101 Duan, G., Xu, D., Zhang, Q., Zhang, G., Cagin, T. *et al.* Molecular dynamics study of the binary Cu46Zr54 metallic glass motivated by experiments: glass formation and atomic-level structure. *Phys Rev B* **71**, 9 (2005).

102 Mendelev, M. I., Rehbein, D. K., Ott, R. T., Kramer, M. J. & Sordelet, D. J. Computer simulation and experimental study of elastic properties of amorphous Cu-Zr alloys. *J Appl Phys* **102**, 8 (2007).

103 Cheng, Y. Q., Cao, A. J., Sheng, H. W. & Ma, E. Local order influences initiation of plastic flow in metallic glass: effects of alloy composition and sample cooling history. *Acta Mater* **56**, 5263-5275 (2008).

104 Honeycutt, J. D. & Andersen, H. C. Molecular-dynamics study of melting and freezing and of small Lennard-Jones Clusters. *J. Phys. Chem.* **91**, 4950-4963 (1987).

105 Hsu, C. S. & Rahman, A. Interaction potentials and their effect on crystal nucleation and symmetry. *Journal of Chemical Physics* **71**, 4974-4986 (1979).

106 Cape, J. N., Finney, J. L. & Woodcock, L. V. An analysis of crystallization by homogeneous nucleation in a 4000-atom soft-sphere model. *Journal of Chemical Physics* **75**, 2366-2373 (1981).

107 Rapaport, D. C. Density-fluctuations and hydrogen-bonding in supercooled water. *Mol Phys* **48**, 23-31 (1983).

108 Medvedev, N. N., Geiger, A. & Brostow, W. Distinguishing liquids from amorphous solids - percolation analysis on the voronoi network. *Journal of Chemical Physics* **93**, 8337-8342 (1990).

109 Finney, J. L. Random packings and structure of simple liquids. 1. Geometry of random close packing. *Proceedings of the Royal Society of London Series a-Mathematical and Physical Sciences* **319**, 479-& (1970).

110 Finney, J. L. Modelling structures of amorphous metals and alloys. *Nature* **266**, 309-314 (1977).

111 Cheng, Y. Q., Ma, E. & Sheng, H. W. Atomic level structure in multicomponent bulk metallic glass. *Phys Rev Lett* **102**, 4 (2009).

112 Park, K. W., Wakeda, M., Shibutani, Y., Fleury, E. & Lee, J. C. Effect of the atomic packing density on the structural change rate of amorphous alloys under elastostatic stress. *Met. Mater.-Int.* **14**, 159-163 (2008).

113 Shimizu, F., Ogata, S. & Li, J. Theory of shear banding in metallic glasses and molecular dynamics calculations. *Mater. Trans.* **48**, 2923-2927 (2007).

114 Hill, R. *The mathematical theory of plasticity*. (Oxford University Press, 1998).

115 Bruck, H. A., Christman, T., Rosakis, A. J. & Johnson, W. L. Quasi-static constitutive behavior of Zr41.25ti13.75ni10cu12.5be22.5 bulk amorphous-alloys. *Scripta Metall Mater* **30**, 429-434 (1994).

116 Luborsky, F. E. *Amorphous metallic alloys*. (Butterworths, 1983).

117 Kimura, H., Ast, D. G. & Bassett, W. A. Deformation of amorphous Fe40ni40p14b6 under compression to 250-Kbar. *J Appl Phys* **53**, 3523-3528 (1982).

118 Barker, L. M. & Hollenba.Re. Laser Interferometer for measuring high velocities of any reflecting surface. *J Appl Phys* **43**, 4669-& (1972).

119 Lubliner, J. *Plasticity theory*. (Collier Macmillan, 1990).

120 Martin, M., Sekine, T., Kobayashi, T., Kecskes, L. & Thadhani, N. N. High-pressure equation of the state of a zirconium-based bulk metallic glass. *Metallurgical and Materials Transactions a-Physical Metallurgy and Materials Science* **38A**, 2689-2696 (2007).

121 Turneaure, S. J., Winey, J. M. & Gupta, Y. M. Compressive shock wave response of a Zr-based bulk amorphous alloy. *Appl. Phys. Lett.* **84**, 1692-1694 (2004).

122 Kanel, G. I., Razorenov, S. V. & Fortov, V. E. *Shock-wave phenomena and the properties of condensed matter*. (Springer, 2004).

123 Kanel, G. I., Razorenov, S. V., Savinykh, A. S., Rajendran, A. & Chen, Z. A study of the failure wave phenomenon in glasses compressed at different levels. *J Appl Phys* **98**, 7 (2005).

124 Zhuang, S. M., Lu, J. & Ravichandran, G. Shock wave response of a zirconium-based bulk metallic glass and its composite. *Appl. Phys. Lett.* **80**, 4522-4524 (2002).

125 Yuan, F. P., Prakash, V. & Lewandowski, J. J. Spall strength and Hugoniot elastic limit of a zirconium-based bulk metallic glass under planar shock compression. *J. Mater. Res.* **22**, 402-411 (2007).

126 Togo, H., Zhang, Y., Kawamura, Y. & Mashimo, T. Properties of Zr-based bulk metallic glass under shock compression. *Mater. Sci. Eng. A-Struct. Mater. Prop. Microstruct. Process.* **449**, 264-268 (2007).

127 Cheng, Y. Q., Ma, E. & Sheng, H. W. Alloying strongly influences the structure, dynamics, and glass forming ability of metallic supercooled liquids. *Appl. Phys. Lett.* **93**, 3 (2008).

128 Shi, Y. F. & Falk, M. L. Strain localization and percolation of stable structure in amorphous solids. *Phys Rev Lett* **95**, 4 (2005).

129 Li, J. AtomEye: an efficient atomistic configuration viewer. *Modelling and Simulation in Materials Science and Engineering* **11**, 173-177 (2003).

130 Cao, A. J., Cheng, Y. Q. & Ma, E. Structural processes that initiate shear localization in metallic glass. *Acta Mater* **57**, 5146-5155 (2009).

131 Delogu, F. Molecular dynamics study of size effects in the compression of metallic glass nanowires. *Phys Rev B* **79**, 184109 (2009).

132 Delogu, F. Deformation processes in an amorphous nanometer-sized metallic particle. *Phys Rev B* **77**, 174104 (2008).

133 Das, J., Tang, M. B., Kim, B. K., Theissmann, R., Baier, F. *et al.* "Work-hardenable" ductile bulk metallic glass. *Phys Rev Lett* **94**, 4 (2005).

134 Chen, M. W. Mechanical behavior of metallic glasses: microscopic understanding of strength and ductility. *Annu Rev Mater Res* **38**, 445-469 (2008).

135 Luo, S. N., Zheng, L. Q., An, Q. & Zhao, S. J. Tensile failure of single-crystal and nanocrystalline Lennard-Jones solids under uniaxial strain. *Int J Mod Phys C* **17**, 1551-1561 (2006).

136 Ashkenazy, Y. & Averback, R. S. Shock induced amorphization as the onset of spall. *Appl. Phys. Lett.* **86**, 3 (2005).

137 Wang, X. D., Jiang, Q. K., Cao, Q. P., Bednarcik, J., Franz, H. *et al.* Atomic structure and glass forming ability of Cu46Zr46Al8 bulk metallic glass. *J Appl Phys* **104**, 5 (2008).

138 Jakse, N. & Pasturel, A. Local order and dynamic properties of liquid and undercooled CuxZr1-x alloys by ab initio molecular dynamics. *Phys Rev B* **78**, 9 (2008).

139 Suzuki, Y., Haimovich, J. & Egami, T. Bond-orientational anisotropy in metallic glasses observed by X-ray diffraction. *Phys Rev B* **35**, 2162-2168 (1987).

140 Egami, T. Formation and deformation of metallic glasses: atomistic theory. *Intermetallics* **14**, 882-887 (2006).

141 Guerdane, M. & Teichler, H. Short-range-order lifetime and the "boson peak" in a metallic glass model. *Phys Rev Lett* **101**, 4 (2008).

142 Arman, B., Luo, S. N., Germann, T. C. & Cagin, T. Dynamic response of Cu46Zr54 metallic glass to high-strain-rate shock loading: plasticity, spall, and atomic-level structures. *Phys Rev B* **81,** 144201 (2010).

143 Li, Q. K. & Li, M. Effects of surface imperfections on deformation and failure of amorphous metals. *Appl. Phys. Lett.* **87**, 031910 (2005).

144 Bailey, N. P., Schiotz, J. & Jacobsen, K. W. Atomistic simulation study of the shear-band deformation mechanism in Mg-Cu metallic glasses. *Phys Rev B* 73, 064108 (2006).

145 Li, Q. K. & Li, M. Atomic scale characterization of shear bands in an amorphous metal. *Appl. Phys. Lett.* **88**, 241903 (2006).

146 Li, Q. K. & Li, M. Assessing the critical sizes for shear band formation in metallic glasses from molecular dynamics simulation. *Appl. Phys. Lett.* **91**, 231905 (2007).

147 Shi, Y. F. & Falk, M. L. Stress-induced structural transformation and shear banding during simulated nanoindentation of a metallic glass. *Acta Mater* **55**, 4317-4324 (2007).

148 Shi, Y. F. Size-independent shear band formation in amorphous nanowires made from simulated casting. *Appl. Phys. Lett.* **96**, 121909 (2010).

149 Nieh, T. G. & Wadsworth, J. Bypassing shear band nucleation and ductilization of an amorphous-crystalline nanolaminate in tension. *Intermetallics* **16**, 1156-1159 (2008).

150 Lv, F., Wen, S. P., Zong, R. L., Zeng, F., Gao, Y. *et al.* Nanoindentation study of amorphous-Co79Zr13Nb8/Cr multilayers. *Surf Coat Tech* **202**, 3239-3245 (2008).

151 Cheng, Y. Q., Cao, A. J. & Ma, E. Correlation between the elastic modulus and the intrinsic plastic behavior of metallic glasses: the roles of atomic configuration and alloy composition. *Acta Mater* **57**, 3253-3267 (2009).

152 Tsuzuki, H., Branicio, P. S. & Rino, J. P. Structural characterization of deformed crystals by analysis of common atomic neighborhood. *Comput Phys Commun* **177**, 518-523 (2007).

153 Jonsson, H. & Andersen, H. C. Icosahedral ordering in the Lennard-Jones liquid and glass. *Phys Rev Lett* **60**, 2295-2298 (1988).

154 Bulatov, V. V. & Cai, W. Nodal effects in dislocation mobility. *Phys Rev Lett* **89**, 115501 (2002).

155 Kelchner, C. L., Plimpton, S. J. & Hamilton, J. C. Dislocation nucleation and defect structure during surface indentation. *Phys Rev B* **58**, 11085-11088 (1998).

156 Li, J., Ngan, A. H. W. & Gumbsch, P. Atomistic modelling of mechanical behavior. *Acta Mater* **51**, 5711-5742 (2003).

157 Zimmerman, J. A., Kelchner, C. L., Klein, P. A., Hamilton, J. C. & Foiles, S. M. Surface step effects on nanoindentation. *Phys Rev Lett* **87**, 165507 (2001).

158 Hirth, J. P. *Dislocations in solids. Volume 14*. (North Holland, 2008).

159 Shi, Y. & Falk, M. L. Does metallic glass have a backbone? The role of percolating short range order in strength and failure. *Scripta Mater* **54**, 381-386 (2006).

160 Brandl, C. & Ph.D. dissertation, Ecole Polytechnique Federale de Lausanne. (2009).

161 Cao, A., Wei, Y. G. & Ma, E. Grain boundary effects on plastic deformation and fracture mechanisms in Cu nanowires: molecular dynamics simulations. *Phys Rev B* **77**, 195429 (2008).

162 Monk, J. & Farkas, D. Tension-compression asymmetry and size effects in nanocrystalline Ni nanowires. *Philos Mag* **87**, 2233-2244 (2007).

163 Derlet, P. M. & Van Swygenhoven, H. The role played by two parallel free surfaces in the deformation mechanism of nanocrystalline metals: a molecular dynamics simulation. *Philos. Mag. A-Phys. Condens. Matter Struct. Defect Mech. Prop.* **82**, 1-15 (2002).

164 Schmidt, D. N. & Evans, M. W. Shock wave compression of plexiglas in 2.5 to 20 kilobar region. *Nature* **206**, 1348-& (1965).

165 Pastine, D. J. P V T Equation of state for polyethlyene. *Journal of Chemical Physics* **49**, 3012-& (1968).

166 Liao, K. & Li, S. Interfacial characteristics of a carbon nanotube-polystyrene composite system. *Appl. Phys. Lett.* **79**, 4225-4227 (2001).

167 Hu, Y., Jang, I. & Sinnott, S. B. Modification of carbon nanotube-polystyrene matrix composites through polyatomic-ion beam deposition: predictions from molecular dynamics simulations. *Composites Science and Technology* **63**, 1663-1669 (2003).

168 Frankland, S. J. V., Harik, V. M., Odegard, G. M., Brenner, D. W. & Gates, T. S. The stress-strain behavior of polymer-nanotube composites from molecular dynamics simulation. *Composites Science and Technology* **63**, 1655-1661 (2003).

169 Bourne, N. K. & Milne, A. M. Shock to detonation transition in a plastic bonded explosive. *J Appl Phys* **95**, 2379-2385 (2004).

170 Setchell, R. E. & Anderson, M. U. Shock-compression response of an alumina-filled epoxy. *J Appl Phys* **97**, 8 (2005).

171 Millett, J. C. F., Bourne, N. K., Meziere, Y. J. E., Vignjevic, R. & Lukyanov, A. The effect of orientation on the shock response of a carbon fibre-epoxy composite. *Composites Science and Technology* **67**, 3253-3260 (2007).

172 Jiang, D. E., van Duin, A. C. T., Goddard, W. A. & Dai, S. Simulating the initial stage of phenolic resin carbonization via the ReaxFF reactive force field. *Journal of Physical Chemistry A* **113**, 6891-6894 (2009).

173 Makeev, M. A., Sundaresh, S. & Srivastava, D. Shock-wave propagation through pristine a-SiC and carbon-nanotube-reinforced a-SiC matrix composites. *J Appl Phys* **106,** 014311 (2009).

174 Ge, T. & Robbins, M. O. Anisotropic plasticity and chain orientation in polymer glasses. *Journal of Polymer Science Part B-Polymer Physics* **48**, 1473-1482 (2010).

175 Mattsson, T. R., Lane, M. D., Cochrane, K. R., Desjarlais, M. P., Thompson, A. P. *et al.* First-principles and classical molecular dynamics simulation of shocked polymers. *Phys Rev B* **81** (2010).

176 Barker, L. M. & Hollenba, R. E. Shock-wave studies of pmma, fused silica, and sapphire. *J Appl Phys* **41**, 4208-& (1970).

177 Elert, M. & American Physical Society. *Shock Compression of Condensed Matter--2007: proceedings of the Conference of the American Physical Society Topical Group on Shock Compression of Condensed Matter held in Waikoloa, Hawai'i, June 24-June 29, 2007*. (American Institute of Physics, 2007).

178 Hazell, P. J., Cowie, A., Kister, G., Stennett, C. & Cooper, G. A. Penetration of a woven CFRP laminate by a high velocity steel sphere impacting at velocities of up to 1875 m/s. *Int J Impact Eng* **36**, 1136-1142 (2009).

179 Hazell, P. J., Appleby-Thomas, G. J. & Kister, G. Impact, penetration, and perforation of a bonded carbon-fibre-reinforced plastic composite panel by a

high-velocity steel sphere: an experimental study. *J Strain Anal Eng* **45**, 439-450 (2010).

180 Lopez-Puente, J., Varas, D., Loya, J. A. & Zaera, R. Analytical modelling of high velocity impacts of cylindrical projectiles on carbon/epoxy laminates. *Compos Part a-Appl S* **40**, 1223-1230 (2009).

181 Hazell, P. J., Stennett, C. & Cooper, G. The effect of specimen thickness on the shock propagation along the in-fibre direction of an aerospace-grade CFRP laminate. *Compos Part a-Appl S* **40**, 204-209 (2009).

182 Appleby-Thomas, G. J., Hazell, P. J. & Stennett, C. The variation in lateral and longitudinal stress gauge response within an RTM 6 epoxy resin under one-dimensional shock loading. *J Mater Sci* **44**, 6187-6198 (2009).

183 Hazell, P. J., Stennett, C. & Cooper, G. The shock and release behavior of an aerospace-grade cured aromatic amine epoxy resin. *Polym Composite* **29**, 1106-1110 (2008).

184 Elert, M. L., Zybin, S. V. & White, C. T. Molecular dynamics study of shock-induced chemistry in small condensed-phase hydrocarbons. *Journal of Chemical Physics* **118**, 9795-9801 (2003).

185 Baughman, R. H., Zakhidov, A. A. & de Heer, W. A. Carbon nanotubes - the route toward applications. *Science* **297**, 787-792 (2002).

186 Sun, H. COMPASS: an ab initio force-field optimized for condensed-phase applications - overview with details on alkane and benzene compounds. *J Phys Chem B* **102**, 7338-7364 (1998).

187 Shenogin, S. & Ozisik, R. *Xeno View*, accessed on 2010, http://www.rpi.edu/~ozisik/RahmiOzisik/XenoView.html.

188 Wei, C. Y., Srivastava, D. & Cho, K. Structural ordering in nanotube polymer composites. *Nano Letters* **4**, 1949-1952 (2004).

189 Han, L. B., An, Q., Luo, S. N. & Goddard, W. A. Ultra-elastic and inelastic impact of Cu nanoparticles. *Materials Letters* **64**, 2230-2232 (2010).

190 Stukowski, A. Visualization and analysis of atomistic simulation data with OVITO-the open visualization tool. *Modelling and Simulation in Materials Science and Engineering* 18 (2010).

191 W. J. Carter and S. P. Marsh. Hugoniot equation of state of polymers. *Los Alamos National Laboratory Report No. LA-13006-MS* (1995).

192 S. P. Marsh. Shock Hugoniot Data (University of California Press, Berkeley, 1980).

VITA

Name: Bedri Arman

Address: Department of Chemical Engineering

Texas A&M University

3122 TAMU

College Station, TX 77843-3122

c/o Tahir Cagin

Email Address: bedriarman@hotmail.com

Education: B.S., Chemical Engineering, Bogazici University, 2003

M.S., Materials Science and Engineering, New Mexico Institute of Mining and Technology, 2005

Ph.D., Chemical Engineering, Texas A&M University, 2011